Fabrication of Metal Halide Perovskites via Mist Deposition Method for Solar Cells and X-Ray Detection Applications

by

Yuki Haruta

ABSTRACT

Nowadays, the world's energy problem is threatening the development of humankind. To address the world's energy problem, we need to explore ways to save energy. In this regard, the concept of "producing functional materials via a low-energy process" is important. Recently, metal halide perovskites, such as $CsPbBr_3$ and $Cs_2AgBiBr_6$, have attracted much attention as a promising functional material that can be produced via low-energy solution processes. Metal halide perovskites show excellent optoelectronic properties that are confirmed with brilliant device performances of highly efficient solar cells and highly sensitive X-ray detectors. However, most of the previous studies have been limited to laboratory-scale small devices due to the lack of a scalable deposition process. To proceed with the practical applications of metal halide perovskites, the development of a scalable deposition method is highly required.

In this thesis, the author focuses on the mist deposition method, which is one of the scalable deposition processes. Through the meticulous study on the fabrication conditions, the mist deposition method successfully produces $CsPbBr_3$ and $Cs_2AgBiBr_6$ films with excellent carrier transport properties comparable to that of single crystals. The mist deposition method realizes a wide thickness control range of approximately 0.5–100 μm that can be applied from solar cells to X-ray detectors. Additionally, the growth mechanism in the mist deposition method is investigated to generalize this method to other promising perovskite materials. This study provides knowledge on the fabrication of metal halide perovskite materials in the scalable deposition method for proceeding with their practical applications.

Table of contents

Chapter 1
General Introduction

1.1 How to Solve the World's Energy Problem

1.1.1 World Energy Consumption

The world's energy consumption has exploded since the Industrial Revolution in the mid-18th century. In 2019, the annual energy consumption reached 158,839 TWh which is more than 8 times higher compared to that in 100 years ago (Figure 1-1).[1] To meet the enormous energy demand, we have depended on fossil fuels (coal, oil, and gas) for more than 85% of our energy. The increasing consumption of fossil fuels extraordinarily overcomes the production of them, which means the depletion of energy sources will come someday. In addition, the combustion of tons of fossil fuels produces greenhouse gases causing global warming and climate change. Nowadays, the world's energy problem is threatening our future life.

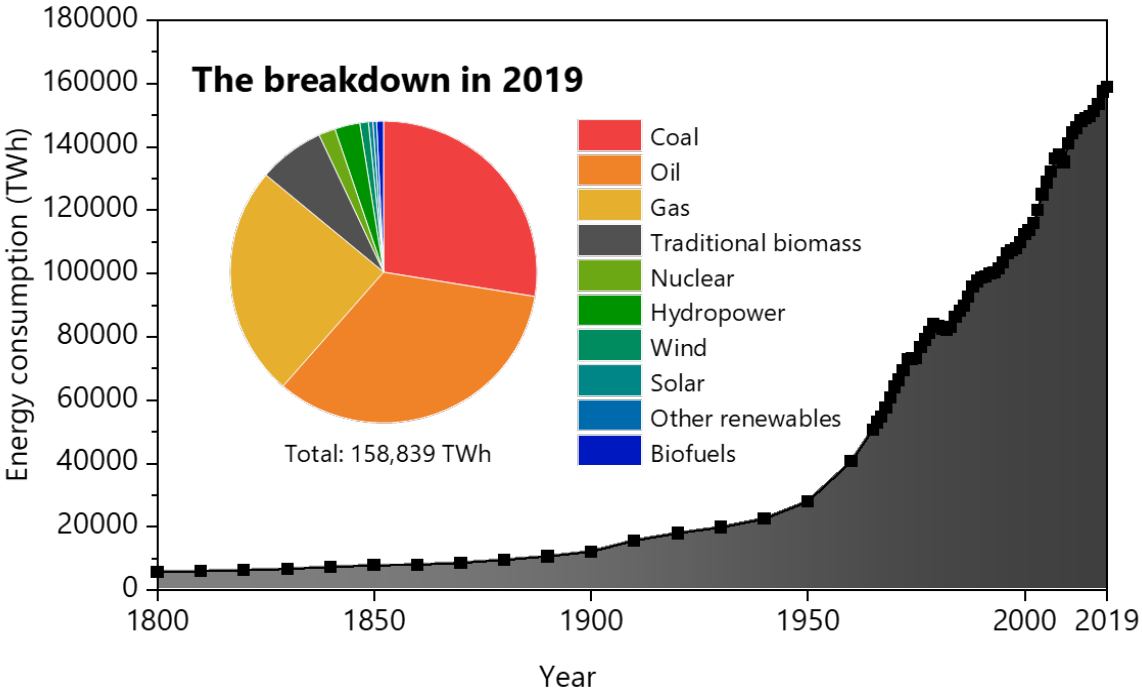

Figure 1-1| World primary energy consumption and the breakdown in 2019. This graph is created based on the data from *Our World in Data*.[1]

1.1.2 Producing Functional Materials via Low Energy Processes

Semiconductor technologies such as solar cells, light-emitting diodes, and photodetectors are supporting our convenient life. While the demand for semiconductors is increasing, the high energy cost for production is a problem. Basically, semiconductors, including Si, GaAs, and CdTe, are very sensitive to defect states, and so high-purity single crystals are required for the application. For instance, single crystal silicon ingots are produced via the Czochralski method with a high temperature (>1000 °C) to achieve high purity of ~11N. Similarly, CdTe and GaAs have been produced via high-energy processes. Although these semiconductor industries have been already established, we cannot depend on these high-energy-cost materials ever under the threat of the world's energy problem.

In this regard, for next-generation functional materials, it is required that they can be produced via a low-energy process. This concept is realized through a two-pronged approach: one of materials chemistry to discover unique materials that can exhibit excellent properties without the need for high-energy processes, and the other of process engineering to fully exploit the properties of these materials. As discussed below, metal halide perovskites have recently emerged as promising and unique materials (section 1.2). In this thesis, to exploit the potential of metal halide perovskites and proceed with the practical applications, the author establishes the fabrication process via the mist deposition method (section 1.4).

1.2 Potential Functional Material: Metal Halide Perovskites

As a promising functional material that can be produced via low-energy processes, metal halide perovskite has attracted much attention since its attractive photovoltaic performance was uncovered in 2009.[2] Metal halide perovskites are semiconducting materials with a perovskite structure with the chemical formula of ABX_3, and its A-, B-, and X-site are accounted for by monovalent cations (A: $CH_3NH_3^+$ (methylammonium; MA^+), $HC(NH_2)_2^+$ (formamidinium; FA^+), Cs^+), divalent metal cations (B: Pb^{2+}, Sn^{2+}) and halogen anion (X: Cl^-, Br^-, I^-), respectively (Figure 1-2). Metal halide perovskites not only have excellent optoelectronic properties (described in section 1.2.1) but also can be produced by using low-cost and low-energy solution processes that required less than 200 °C of fabrication temperature. Thanks to these advantages, metal halide perovskites are expected to apply various optoelectronic devices including solar cells, light-emitting diodes, photodetectors, and X-ray detectors (described in section 1.2.2).

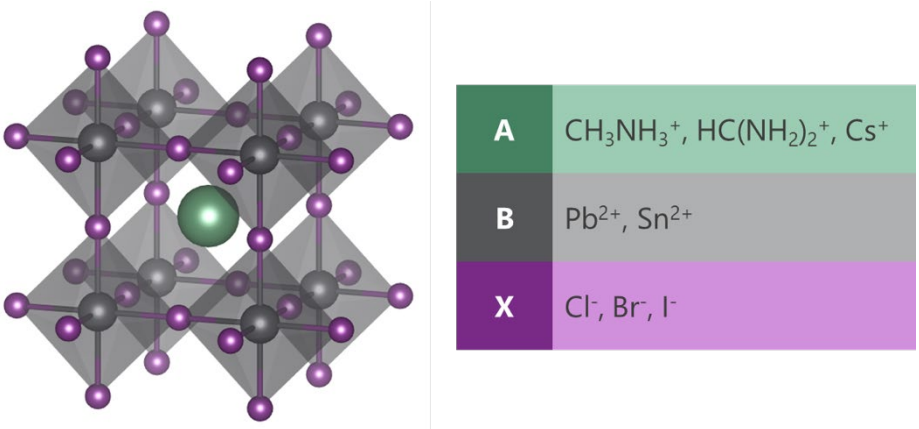

Figure 1-2| Crystal structure of metal halide perovskites with the chemical formula of ABX_3 and representative ions for A-, B-, and X-site.

1.2.1 Optoelectronic Properties of Metal Halide Perovskites

The optoelectronic properties of metal halide perovskites, including photon absorption capability, defect tolerance, and charge transport properties are described in detail to clarify the potential as a next-generation functional material.

Bandgap (E_g) and Photon Absorption Capability

Metal halide perovskites have direct band gaps of 1.2–3.5 eV depending on the composition.[3–5] Since these band gaps correspond to the energy of visible light, metal halide perovskites are suitable for application for solar cells, light-emitting diodes, and photodetectors. In addition, metal halide perovskites have high absorption coefficients thanks to their heavy elements such as Pb. For instance, $CH_3NH_3PbI_3$ ($MAPbI_3$) can absorb sunlight almost completely with only a thickness of less than 500 nm, while silicon requires more than 100 μm.[6]

Metal halide perovskites have also high X-ray attenuation coefficients (Figure 1-3).[7] Especially, the much higher attenuation coefficient against the photon energy in the range of 40–120 keV, which is used for computed tomography (CT) but not covered by conventional amorphous Se (a-Se) detectors, is a major advantage of metal halide perovskites.

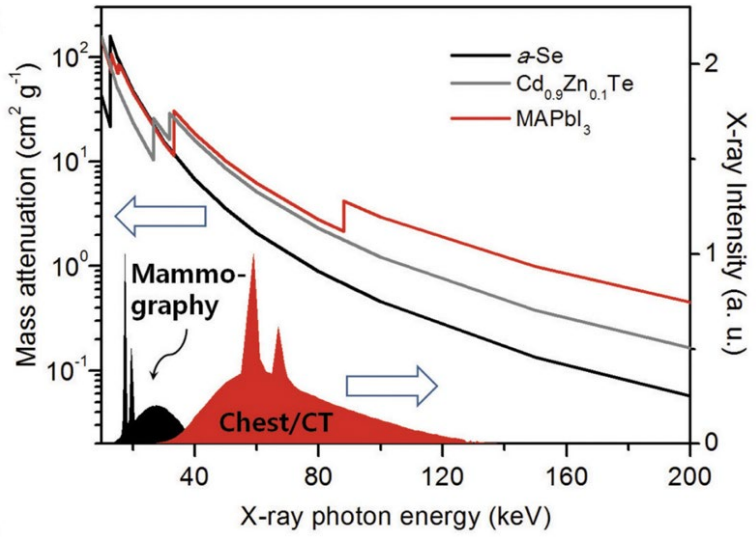

Figure 1-3| X-ray attenuation coefficients of metal halide perovskites, a-Se, $Cd_{0.9}Zn_{0.1}Te$, and $CH_3NH_3PbI_3$ ($MAPbI_3$). Cited from *Nature*.[7]

Defect Tolerance

One of the factors that make metal halide perovskites distinct from conventional semiconductors is the high defect tolerance. In the case of conventional semiconductors such as GaAs and CdTe, extremely low defect density is required to achieve the practical properties because the intrinsic defect states are located at the deep level in the bandgaps and so they work as severe trap states, dramatically deteriorating the electronic properties.[8] On the other hand, in the case of metal halide perovskites, the intrinsic defect states are located at shallow levels (Figure 1-4), and thus they do not work as severe trap states, leading to the high defect tolerance.[9,10] Thanks to their high defect tolerance, metal halide perovskites show long carrier lifetimes even polycrystalline films.[11] It should be noted that this high defect tolerance is significant in lead halide perovskites ($APbX_3$), but not in tin halide perovskites due to the deep defect level of oxidized tin (Sn(IV)).

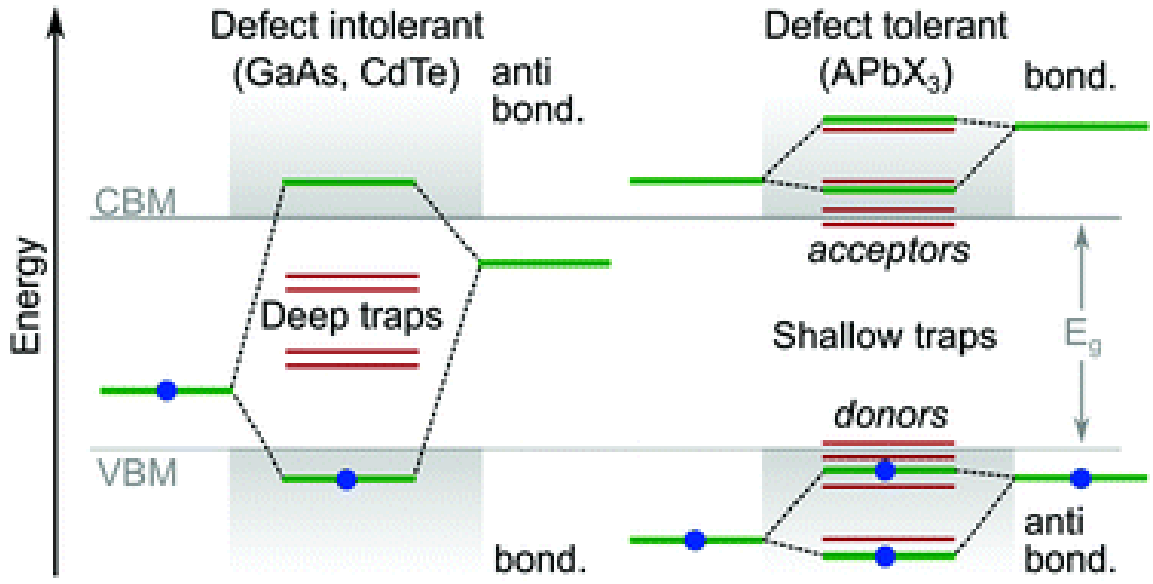

Figure 1-4| Comparison of typical defect states of conventional semiconductors and metal halide perovskites. Cited from *Materials Horizons*.[10]

Carrier Transport Properties

Carrier transport properties, including mobility (μ), lifetime(τ), and diffusion length (L_D), are important factors for optoelectronic device applications. The carrier mobility of perovskite single crystals has been reported in the range of 10–1000 $cm^2\ V^{-1}\ s^{-1}$.[12–21] For instance, Dong. *et al.* reported that $MAPbI_3$ single crystal showed high hole mobility of 164 ± 25 $cm^2\ V^{-1}\ s^{-1}$ and high electron mobility of 24.8 ± 4.1 $cm^2\ V^{-1}\ s^{-1}$. In the same paper, a long carrier lifetime of 95 μs and a long diffusion length of 175 μm under 1 sun illumination were reported.[12] In addition, thanks to their high defect tolerance, even polycrystalline films that include many trap densities at the grain boundaries show a long carrier diffusion length of over 1 μm, exceeding the distance required for charge collection in solar cell applications.[11]

1.2.2 Applications of Metal Halide Perovskites

The excellent properties of metal halide perovskites encourage their applications for various optoelectronic devices such as solar cells and X-ray detectors. In this section, the progress of these device applications is introduced as follows:

Perovskite Solar Cells

Since the first paper revealed the photovoltaic properties of metal halide perovskites, researchers have made a lot of efforts to improve the power conversion efficiency, including device engineering,[22–43] compositional engineering,[3,44–63] and process engineering.[24,64–86] As shown in Figure 1-5,[87] the record efficiency has increased from 3.8% on the first paper to 25.5%, which is comparable to the record of single-crystal Si solar cells. In addition to the high power conversion efficiency, the perovskite solar cells have many advantages such as lightweight, low-cost, and flexibility, compared to the conventional Si and CdTe solar cells. Given these advantages, for instance, ultra-thin flexible solar cells with an overall thickness of 3 μm have been proposed, which cannot be realized by conventional semiconductors.[88] This is a good demonstration that show perovskite solar cell is a next-generation device.

In addition to the single-junction solar cells, multi-junction (tandem) solar cells are also attracting much attention for breaking the Shockley-Queisser efficiency limit. In tandem solar cells, narrow-bandgap (0.8–1.4 eV) and wide-bandgap (1.4–2.0 eV) materials are stacked on top of each other to utilize as many photons included in sunlight as possible. Metal halide perovskites are promising for tandem solar cells thanks to their tunable bandgaps.[89] For example, considering that a material with a bandgap of 1.7 eV is suitable for the top cell of the tandem solar cell which uses Si in the bottom cell, Si/perovskite (1.68 eV) tandem solar cell with the highest efficiency of 29.15% was reported in 2021.[90]

In summary, metal halide perovskites have a great potential for the photoconductive layer of next-generation solar cells, which shows various advantages including high efficiency, lightweight, low-cost processes, and flexibility.

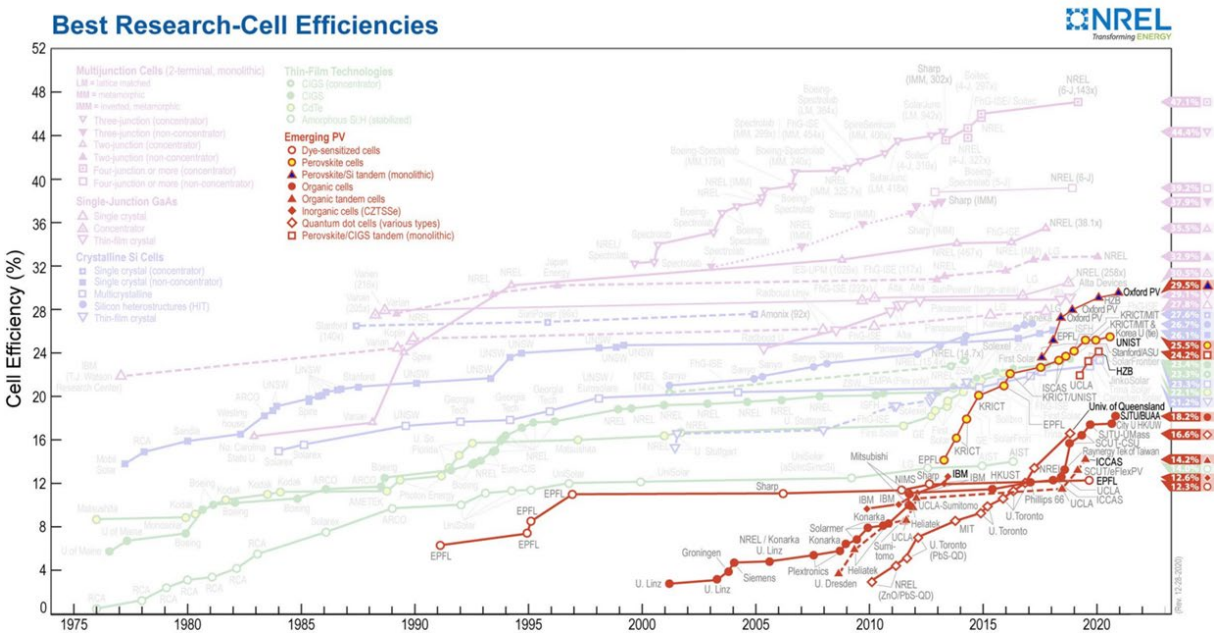

Figure 1-5| History of best power conversion efficiency of various solar cells. Cited from *NREL Efficiency Chart*.[87]

Perovskite X-Ray Detectors

Metal halide perovskites are also expected for X-ray detection applications thanks to their high X-ray absorption coefficient, excellent carrier transport properties, and large bulk resistivity.[91–96] Traditional X-ray detectors that work at room temperature are based on two semiconductor materials: amorphous Se (a-Se) films or $Cd_{1-x}Zn_xTe$ (CZT) single crystals.[97,98] However, the poor sensitivity of a-Se-based detectors and the high energy-cost of CZT-based detectors are problems. On the other hand, recently emerged solution-processed metal halide perovskites have good potential to surpass traditional X-ray detectors. Since the first example of solution-processed perovskite X-ray detector was reported in 2015 using $MAPbI_3$,[99] various perovskite X-ray detectors with high sensitivities have been reported as follows: guanidinium-doped $MAPbI_3$ single crystal (23,000 μC Gy_{air}^{-1} cm^{-2}),[100] $MAPbBr_{2.94}Cl_{0.06}$ single crystal (84,000 μC Gy_{air}^{-1} cm^{-2}),[16] $MAPbBr_3$ single crystal (23,600 μC Gy_{air}^{-1} cm^{-2}),[101] and Rb-doped $CsPbBr_3$ single crystal (8,097 μC Gy_{air}^{-1} cm^{-2}).[102] These sensitivities are much higher than that of traditional a-Se-based X-ray detectors (20 μC Gy_{air}^{-1} cm^{-2}).[97] In addition, perovskite X-ray detectors show low detection limit of tens of $nGy_{air}s^{-1}$, which is significantly lower than the 5,500 $nGy_{air}s^{-1}$ in a-Se based X-ray detectors. These excellent properties are enough to attract much attention for practical application of perovskite X-ray detectors in medical diagnosis, industrial inspection, and security inspection.

1.3 Challenges for the Practical Application of Perovskites

While brilliant devices have been realized by using metal halide perovskites, there are two major challenges for the transition from laboratory to industry: (1) improvement of the device stability and (2) development of scalable deposition processes.

1.3.1 Improvement of the Device Stability

While metal halide perovskites show excellent optoelectronic properties, the instability against heat, moisture, and oxygen is a big issue for the application.[103,104] Organic-inorganic hybrid perovskites whose A-site is occupied by an organic cation will decompose at a high temperature of approximately 150 °C, limiting subsequent device processes. In the case of iodide perovskites (ABI_3), they will deteriorate even at room temperature due to moisture. For instance, $MAPbI_3$ polycrystalline films degrade under ambient air in a few hours.[105] In the case of tin-based perovskites ($ASnX_3$), the oxidization from Sn(II) to Sn(IV) easily happens in ambient air, and the Sn(IV) produces anomalous defect states, deteriorating the device performance.[5,106,107] Therefore, these perovskite materials are fabricated in a glove box with inert gas, which is not preferable for industrialization. Although several passivation strategies[38,108] and encapsulation strategies[109–113] have been proposed to improve the stability under ambient air, unfortunately, the stability is not enough.

Among the metal halide perovskites, cesium lead tri-bromide ($CsPbBr_3$) has shown the highest stability, which includes no organic cations, iodide, and tin.[45,114] Although the stability of $CsPbBr_3$ is enough for practical application, the method for fabricating high-quality $CsPbBr_3$ films is not mature compared to organic-inorganic hybrid perovskites.

1.3.2 Development of Scalable Deposition Processes

In addition to the improvement of stability, the development of a scalable deposition process is also required for practical applications. For solar cell applications, most perovskite thin films have been fabricated by using a spin-coating method. While the fabrication strategy in the spin-coating method has improved to achieve highly efficient perovskite solar cells, the spin-coating method is not suitable for large-area fabrication. The active area of perovskite solar cells that achieved >20% efficiency is usually less than 1 cm^2. Up to now, spray deposition,[60,115–123] blade coating,[124,125] inkjet printing,[69,71] and slot-die coating[126–129] have been introduced for up-scaling. Although certified efficiency of 19.2% has been recorded using 50 cm^2-area $MA_{0.6}FA_{0.4}PbI_3$ films fabricated by blade-coating,[124] the efficiency is still much lower than the record of spin-coating (25.5%). Further improvement of scalable deposition processes is required.

For X-ray detector applications, the reports on scalable deposition processes are much less compared to solar cell applications because of the more difficult requirement for X-ray detectors; much thicker perovskite films (>100 μm) are required to absorb X-ray photons. In fact, most perovskite X-ray detectors are realized by using not thick films but mm-scale single crystals.[13,100–102,130–132] The single crystal has enough thickness to absorb photons but lacks scalability. The lack of scalability is limiting the potential of perovskite X-ray detectors toward X-ray imaging devices that need more than 100 cm^2 area.

1.4 Strategies for Overcoming the Challenges

1.4.1 All-Inorganic Perovskites

To overcome the instability issue, exploring all-inorganic perovskite is one of the good solutions.[133] All-inorganic perovskites, which substitute inorganic cations (Cs^+) with organic cations, show improved stability. Among the all-inorganic perovskites, $CsPbBr_3$ and $Cs_2AgBiBr_6$ are promising stable materials for practical applications.[45,134] Herein, the progress and challenges of $CsPbBr_3$ and $Cs_2AgBiBr_6$ are introduced as follows:

$CsPbBr_3$

Among all-inorganic perovskites, $CsPbBr_3$ shows good stability. Kulbak et al. has reported a comparison between $MAPbBr_3$ and $CsPbBr_3$ to prove the improved stability thanks to cation substitution.[45] While the efficiency of $MAPbBr_3$-based solar cells dropped to 55% of the initial in 5 hours under 100 mW cm^{-2} illumination, the efficiency drops in $CsPbBr_3$-based solar cells was almost nothing, indicating the enhanced stability. Thanks to its high stability, $CsPbBr_3$ has attracted much attention as more practical materials for solar cells,[45,114,135–140] photodetectors,[14,141–145] and X-ray detectors.[17,20,102,146–152]

For solar cell applications, the record efficiency of $CsPbBr_3$-based solar cells has improved from 5.6% to over 10% in the past decade.[45,50,153] However, the efficiency is still much lower than the theoretical limit (~17.5%) due to the lack of development of deposition processes. Further improvement of the deposition process is required.

For X-ray detection applications, many X-ray detectors using $CsPbBr_3$ single crystals have demonstrated high sensitivities.[17,20,102,146–151] On the other hand, for X-ray imaging application, a scalable deposition process for $CsPbBr_3$ thick films is required. The first $CsPbBr_3$ thick film with a thickness of 18 μm was fabricated by the deposition of many cubic-shaped-$CsPbBr_3$ crystals on the substrate from a saturated solution.[154] Although the X-ray detector using the precipitated $CsPbBr_3$ crystals showed high sensitivity of 1,700 μC Gy_{air}^{-1} cm^{-2}, this process is

not suitable for X-ray imaging because the film uniformity is not good due to the rough film morphology consisting of stacked cubic crystals. The hot-press method was also introduced for the fabrication of $CsPbBr_3$ thick films.[155,156] In this method, thick films are fabricated by melting $CsPbBr_3$ powder on the substrate and its solidification by slow cooling. This method is not only scalable but also able to produce high-quality $CsPbBr_3$ monocrystalline grains as proved by their high carrier mobilities and low trap densities, leading to the record high X-ray sensitivity of 55,684 μC Gy_{air}^{-1} cm^{-2}.[155] However, the hot-press method takes high energy-cost and cannot be applied for the deposition on a thermal-sensitive integrated circuit for imaging devices because this method requires a high temperature of approximately 600 °C.

$Cs_2AgBiBr_6$

The toxicity of lead is an issue for the application of metal halide perovskites. Although we can totally replace lead with tin, the relatively low atomic number of Sn is not suitable for especially X-ray detector applications. Recently, the analogy of $CsPbBr_3$ which replaced lead with silver and bismuth, namely $Cs_2AgBiBr_6$, is attracting much attention as a promising lead-free perovskite especially in X-ray detection applications.[15,157–163] Although the sensitivity is low compared to lead halide perovskites, the low noise current thanks to the high bulk resistivity is an advantage of $Cs_2AgBiBr_6$, leading to a low detection limit of 45.7 nGy_{air} s^{-1}.[157]

Polymer-composite film fabrication[161] and hot-pressed wafer fabrication[162] were proposed as the scalable deposition process for $Cs_2AgBiBr_6$ X-ray detectors. However, the former process sacrificed a sensitivity due to the insulating polymer which is required for thick film fabrication, and the latter process has disadvantages that it requires a high temperature and bonding process to the integrated substrate.

1.4.2 Mist Deposition Method

In this thesis, the mist deposition method is explored as a promising scalable deposition process for the practical applications of metal halide perovskites. The mist deposition method is one of the spray deposition methods and it has track records for the scalable deposition of metal oxides[164–170] and organic semiconductors.[169,171,172] But unfortunately, there is no report on the fabrication of all-inorganic perovskites via the mist deposition method. Herein, to clarify the potential as a scalable process for perovskite film formation, the details in the mist deposition method are introduced as follows:

Figure 1-6 shows a schematic illustration of the mist deposition method. The apparatus consists of a mist generation component (Figure 1-6a) and a film deposition component (Figure 1-6b). In the mist generation component, the precursor solution is atomized by ultrasonic vibration. The mist particles are transported by inert gas to the film deposition component, where they are supplied as a curtain-like mist flow from a nozzle onto the preheated substrate. The precursors in the mist particles are immediately deposited accompanied by simultaneous solvent evaporation. To achieve uniform film deposition, the stage on which the substrate is located is moved at a constant speed using a stepping motor during the mist supply. The deposition area is determined by the width of the nozzle and the travel distance of the stage.

While the conventional ultrasonic spray deposition method atomizes at a frequency on the order of kHz, the mist deposition method uses a high frequency on the order of MHz and can produce tiny droplets with a diameter of approximately 3 μm. These droplets are so small that they can float like a "mist" in the air, hence this method is named the mist deposition method.[166] Here is the advantage of this method: the mist containing the precursor can be transported freely like a gas precursor. Therefore, it is possible to design the precursor jetting method according to the application such as large-area production. In this study, a uniform laminar flow of precursor solution droplets is achieved by combining mist generation with the designed ejection nozzle (Figure 1-7).

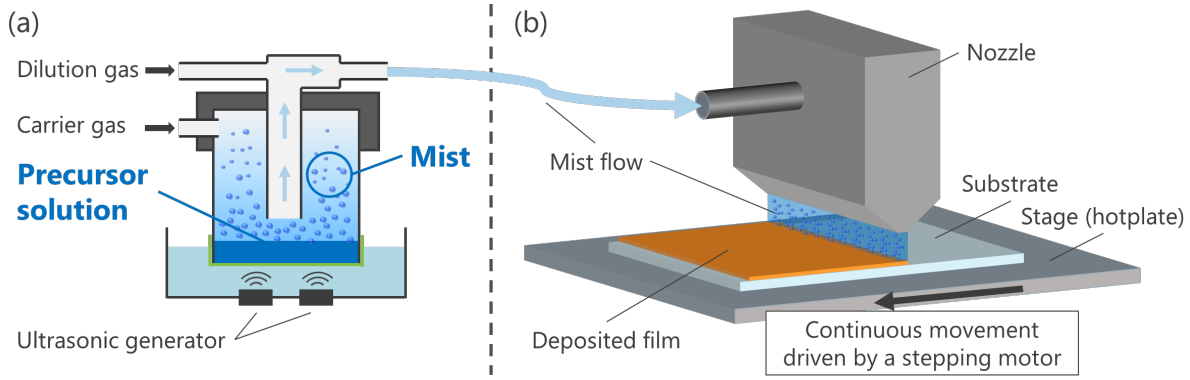

Figure 1-6| Schematic illustration of the mist deposition apparatus, which consists of (a) a mist generation component and (b) a film deposition component.

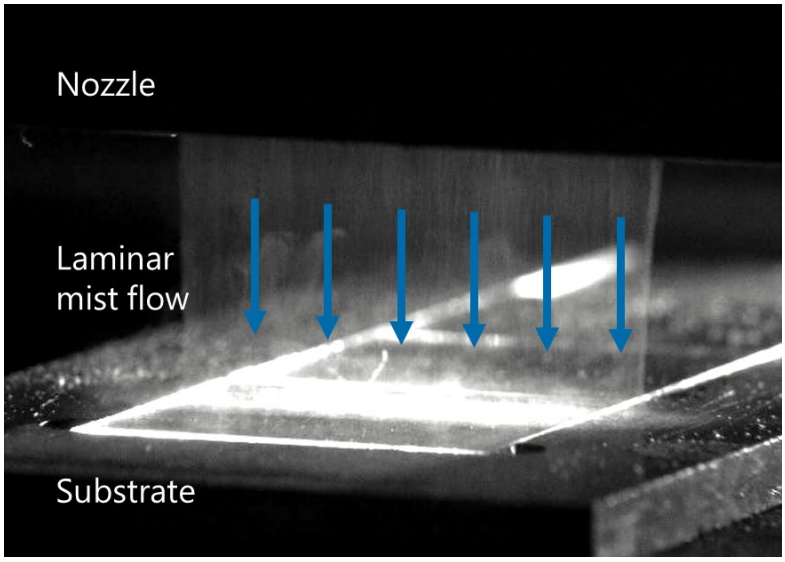

Figure 1-7| A photograph of laminar mist flow ejected from the nozzle. For ease of viewing, the distance between the nozzle and the substrate is much greater than that during the actual process.

1.5 Objective and Outline of This Thesis

Objective

As described above, metal halide perovskite is expected as a functional material that can be fabricated via low-energy processes, but a scalable deposition process for practical application is undeveloped yet. In this thesis, the author aims to develop the basement of fabrication of perovskite films by using the mist deposition method as a new practical deposition method. The author focuses on all-inorganic perovskites ($CsPbBr_3$ and $Cs_2AgBiBr_6$), which show high stability among metal halide perovskites. The author demonstrates their device applications for solar cells and X-ray detectors.

Outline

In Chapter 2, the effects of the basic deposition conditions on the films are investigated. The suitable solvents for the mist deposition of $CsPbBr_3$ are selected based on the investigation of their dissolution capability and viscosity. The mixture solvent of DMSO and DMF is selected. The substrate temperature is changed in the range of 110–190 °C to clarify the effects on the film qualities such as phase purity, crystal orientation, trap density, and carrier mobility.

In Chapter 3, all-inorganic solar cells are fabricated using $CsPbBr_3$ thin films deposited by mist deposition method, and their performance is investigated. Based on the knowledge obtained in Chapter 2, it is clarified that even a $CsPbBr_3$ thin film with a thickness of approximately 340 nm can uniformly cover the entire substrate. All-inorganic perovskite solar cells with an ITO/TiO_2/$CsPbBr_3$/carbon configuration are fabricated using ITO as the transparent electrode, TiO_2 as the electron transport layer, $CsPbBr_3$ as the photoconductive layer, and carbon as the top electrode. The power conversion efficiency, reproducibility, and stability of the solar cells are investigated.

In Chapter 4, fabrication of $CsPbBr_3$ thick film with a thickness of more than 100 μm, which is necessary for X-ray absorption is attempted for the demonstration of X-ray detection. Under the deposition conditions based on the knowledge obtained in Chapter 2, $CsPbBr_3$ thick films with a thickness of 110 μm are obtained. In addition, a polymer layer is introduced in the interface between the $CsPbBr_3$ film and the substrate to suppress an exfoliation. An X-ray detector is fabricated using $CsPbBr_3$ thick films prepared via mist deposition method and the detection properties are investigated.

In Chapter 5, in order to investigate the generality of perovskite deposition via the mist deposition method, I focus on $Cs_2AgBiBr_6$, in which Ag and Bi replaced Pb, a toxic element in $CsPbBr_3$, and attempt its deposition and application to X-ray detectors as well as $CsPbBr_3$. As in the case of $CsPbBr_3$, dense films with columnar grains with thicknesses ranging from approximately 500 nm to 90 μm are obtained. The detection properties of X-ray detectors fabricated using $Cs_2AgBiBr_6$ thick films are investigated. In addition, the growth mechanism of columnar crystals in the mist deposition method is investigated.

References for Chapter 1

1. Energy mix. *Our World in Data* https://ourworldindata.org/energy-mix.

2. Kojima, A., Teshima, K., Shirai, Y. & Miyasaka, T. Organometal Halide Perovskites as Visible-Light Sensitizers for Photovoltaic Cells. *Journal of the American Chemical Society* **131**, 6050–6051 (2009).

3. Hao, F., Stoumpos, C. C., Chang, R. P. H. & Kanatzidis, M. G. Anomalous Band Gap Behavior in Mixed Sn and Pb Perovskites Enables Broadening of Absorption Spectrum in Solar Cells. *Journal of the American Chemical Society* **136**, 8094–8099 (2014).

4. Protesescu, L. *et al.* Nanocrystals of Cesium Lead Halide Perovskites ($CsPbX_3$, X = Cl, Br, and I): Novel Optoelectronic Materials Showing Bright Emission with Wide Color Gamut. *Nano Lett.* **15**, 3692–3696 (2015).

5. Tao, S. *et al.* Absolute energy level positions in tin- and lead-based halide perovskites. *Nature Communications* **10**, 2560 (2019).

6. Chen, Z. *et al.* Thin single crystal perovskite solar cells to harvest below-bandgap light absorption. *Nature Communications* **8**, 1–7 (2017).

7. Kim, Y. C. *et al.* Printable organometallic perovskite enables large-area, low-dose X-ray imaging. *Nature* **550**, 87–91 (2017).

8. Komsa, H.-P. & Pasquarello, A. Identification of defect levels at $In_xGa_{1-x}As$/oxide interfaces through hybrid functionals. *Microelectronic Engineering* **88**, 1436–1439 (2011).

9. Kang, J. & Wang, L.-W. High Defect Tolerance in Lead Halide Perovskite $CsPbBr_3$. *The Journal of Physical Chemistry Letters* **8**, 489–493 (2017).

10. Jin, H. *et al.* It's a trap! On the nature of localised states and charge trapping in lead halide perovskites. *Materials Horizons* **7**, 397–410 (2020).

11. Stranks, S. D. *et al.* Electron-Hole Diffusion Lengths Exceeding 1 Micrometer in an Organometal Trihalide Perovskite Absorber. *Science* **342**, 341–344 (2013).

12. Dong, Q. *et al.* Electron-hole diffusion lengths > 175μm in solution-grown $CH_3NH_3PbI_3$ single crystals. *Science* **347**, 967–970 (2015).

13. Wei, H. *et al.* Sensitive X-ray detectors made of methylammonium lead tribromide perovskite single crystals. *Nature Photonics* **10**, 333–339 (2016).

14. Song, J. *et al.* Ultralarge All-Inorganic Perovskite Bulk Single Crystal for High-Performance Visible-Infrared Dual-Modal Photodetectors. *Advanced Optical Materials* **5**, 1700157 (2017).

15. Pan, W. *et al.* $Cs_2AgBiBr_6$ single-crystal X-ray detectors with a low detection limit. *Nature Photonics* **11**, 726–732 (2017).

16. Wei, H. *et al.* Dopant compensation in alloyed $CH_3NH_3PbBr_{3-x}Cl_x$ perovskite single crystals for gamma-ray spectroscopy. *Nature Materials* **16**, 826–833 (2017).

17. He, Y. *et al.* High spectral resolution of gamma-rays at room temperature by perovskite $CsPbBr_3$ single crystals. *Nature Communications* **9**, 1609 (2018).

18. Zhang, P. *et al.* Anisotropic Optoelectronic Properties of Melt-Grown Bulk $CsPbBr_3$ Single Crystal. *The Journal of Physical Chemistry Letters* **9**, 5040–5046 (2018).

19. Liu, Y. *et al.* Low-temperature-gradient crystallization for multi-inch high-quality perovskite single crystals for record performance photodetectors. *Materials Today* **22**, 67–75 (2019).

20. Peng, J. *et al.* Crystallization of $CsPbBr_3$ single crystals in water for X-ray detection. *Nature Communications* **12**, 1531 (2021).

21. Liu, Y. *et al.* Inch-sized high-quality perovskite single crystals by suppressing phase segregation for light-powered integrated circuits. *Science Advances* **7**, 1–13 (2021).

22. Zhou, C. & Lin, S. Carbon-Electrode Based Perovskite Solar Cells: Effect of Bulk Engineering and Interface Engineering on the Power Conversion Properties. *Solar RRL* **1900190**, 1900190 (2019).

23. Yang, S. *et al.* Stabilizing halide perovskite surfaces for solar cell operation with wide-bandgap lead oxysalts. *Science* **365**, 473–478 (2019).

24. Kim, H.-S. *et al.* Lead Iodide Perovskite Sensitized All-Solid-State Submicron Thin Film Mesoscopic Solar Cell with Efficiency Exceeding 9%. *Scientific Reports* **2**, 1–7 (2012).

25. Lu, J., Chen, S.-C. & Zheng, Q. Defect Passivation of $CsPbIBr_2$ Perovskites for High-Performance Solar Cells with Large Open-Circuit Voltage of 1.28 V. *ACS Applied Energy Materials* **1**, 5872–5878 (2018).

26. Fakharuddin, A., Schmidt-Mende, L., Garcia-Belmonte, G., Jose, R. & Mora-Sero, I. Interfaces in Perovskite Solar Cells. *Advanced Energy Materials* **7**, 1700623 (2017).

27. Jeon, Y.-J. *et al.* Planar heterojunction perovskite solar cells with superior reproducibility. *Scientific Reports* **4**, 6953 (2015).

28. Jiang, Q. *et al.* Surface passivation of perovskite film for efficient solar cells. *Nature Photonics* **13**, 460–466 (2019).

29. Guerrero, A. *et al.* Interfacial Degradation of Planar Lead Halide Perovskite Solar Cells.

ACS Nano **10**, 218–224 (2016).

30. Ding, J., Duan, J., Guo, C. & Tang, Q. Toward charge extraction in all-inorganic perovskite solar cells by interfacial engineering. *Journal of Materials Chemistry A* **6**, 21999–22004 (2018).

31. Yoon, H., Kang, S. M., Lee, J.-K. & Choi, M. Hysteresis-free low-temperature-processed planar perovskite solar cells with 19.1% efficiency. *Energy & Environmental Science* **9**, 2262–2266 (2016).

32. Shen, B. *et al.* Conformal coverage of TiO_2 compact layers for high-efficient planar heterojunction perovskite solar cells. *Organic Electronics* **59**, 177–183 (2018).

33. Tong, G. *et al.* High Efficient Hole Extraction and Stable All-Bromide Inorganic Perovskite Solar Cells via Derivative-Phase Gradient Bandgap Architecture. *Solar RRL* **3**, 1900030 (2019).

34. Domanski, K. *et al.* Not All That Glitters Is Gold: Metal-Migration-Induced Degradation in Perovskite Solar Cells. *ACS Nano* **10**, 6306–6314 (2016).

35. Cojocaru, L. *et al.* Surface Treatment of the Compact TiO_2 Layer for Efficient Planar Heterojunction Perovskite Solar Cells. *Chemistry Letters* **44**, 674–676 (2015).

36. Wang, Q. *et al.* Large Conduction Band Energy Offset Is Critical for High Fill Factors in Inorganic Perovskite Solar Cells. *ACS Energy Letters* **5**, 2343–2348 (2020).

37. Yang, D. *et al.* High efficiency planar-type perovskite solar cells with negligible hysteresis using EDTA-complexed SnO_2. *Nature Communications* **9**, 3239 (2018).

38. Wang, F. *et al.* Highly Efficient and Stable Perovskite Solar Cells by Interfacial Engineering Using Solution-Processed Polymer Layer. *The Journal of Physical Chemistry C* **121**, 1562–1568 (2017).

39. Zhang, X., Zhang, W., Wu, T., Wu, J. & Lan, Z. High efficiency and negligible hysteresis planar perovskite solar cells based on NiO nanocrystals modified TiO_2 electron transport layers. *Solar Energy* **181**, 293–300 (2019).

40. Li, G. *et al.* Overcoming the Limitations of Sputtered Nickel Oxide for High-Efficiency and Large-Area Perovskite Solar Cells. *Advanced Science* **4**, 1700463 (2017).

41. Xia, X. *et al.* Lithium and Silver Co-Doped Nickel Oxide Hole-Transporting Layer Boosting the Efficiency and Stability of Inverted Planar Perovskite Solar Cells. *ACS Applied Materials & Interfaces* **10**, 44501–44510 (2018).

42. Liu, X. *et al.* 17.46% efficient and highly stable carbon-based planar perovskite solar cells employing Ni-doped rutile TiO_2 as electron transport layer. *Nano Energy* **50**, 201–211

(2018).

43. Zhang, H. *et al.* Pinhole-Free and Surface-Nanostructured NiO_x Film by Room-Temperature Solution Process for High-Performance Flexible Perovskite Solar Cells with Good Stability and Reproducibility. *ACS Nano* **10**, 1503–1511 (2016).

44. Savory, C. N., Walsh, A. & Scanlon, D. O. Can Pb-Free Halide Double Perovskites Support High-Efficiency Solar Cells? *ACS Energy Letters* **1**, 949–955 (2016).

45. Kulbak, M. *et al.* Cesium Enhances Long-Term Stability of Lead Bromide Perovskite-Based Solar Cells. *The Journal of Physical Chemistry Letters* **7**, 167–172 (2016).

46. Hu, J. *et al.* Synthetic control over orientational degeneracy of spacer cations enhances solar cell efficiency in two-dimensional perovskites. *Nature Communications* **10**, 1276 (2019).

47. Saliba, M. *et al.* Cesium-containing triple cation perovskite solar cells: improved stability, reproducibility and high efficiency. *Energy Environ. Sci.* **9**, 1989–1997 (2016).

48. Park, B. *et al.* Understanding how excess lead iodide precursor improves halide perovskite solar cell performance. *Nature Communications* **9**, 3301 (2018).

49. Son, D.-Y. *et al.* Universal Approach toward Hysteresis-Free Perovskite Solar Cell via Defect Engineering. *Journal of the American Chemical Society* **140**, 1358–1364 (2018).

50. Yuan, H. *et al.* All-inorganic $CsPbBr_3$ perovskite solar cell with 10.26% efficiency by spectra engineering. *Journal of Materials Chemistry A* **6**, 24324–24329 (2018).

51. Thote, A. *et al.* Stable and Reproducible 2D/3D Formamidinium-Lead-Iodide Perovskite Solar Cells. *ACS Applied Energy Materials* **2**, 2486–2493 (2019).

52. Hu, M. *et al.* Sub-1.4eV bandgap inorganic perovskite solar cells with long-term stability. *Nature Communications* **11**, 151 (2020).

53. McMeekin, D. P. *et al.* A mixed-cation lead mixed-halide perovskite absorber for tandem solar cells. *Science* **351**, 151–155 (2016).

54. Zhang, C. *et al.* Fabrication Strategy for Efficient 2D/3D Perovskite Solar Cells Enabled by Diffusion Passivation and Strain Compensation. *Advanced Energy Materials* **10**, 2002004 (2020).

55. Yi, H. *et al.* Thiocyanate assisted nucleation for high performance mix-cation perovskite solar cells with improved stability. *Journal of Power Sources* **466**, 228320 (2020).

56. Guo, H. *et al.* Doping with $SnBr_2$ in $CsPbBr_3$ to enhance the efficiency of all-inorganic perovskite solar cells. *Journal of Materials Chemistry C* **7**, 11234–11243 (2019).

57. Kim, S.-G. *et al.* Potassium ions as a kinetic controller in ionic double layers for hysteresis-free perovskite solar cells. *Journal of Materials Chemistry A* **7**, 18807–18815 (2019).

58. Zheng, Y. *et al.* High-Performance $CsPbI_xBr_{3-x}$ All-Inorganic Perovskite Solar Cells with Efficiency over 18% via Spontaneous Interfacial Manipulation. *Advanced Functional Materials* **30**, 2000457 (2020).

59. Li, B., Zhang, Y., Zhang, L. & Yin, L. $PbCl_2$-tuned inorganic cubic $CsPbBr_3(Cl)$ perovskite solar cells with enhanced electron lifetime, diffusion length and photovoltaic performance. *Journal of Power Sources* **360**, 11–20 (2017).

60. Heo, J. H., Lee, M. H., Jang, M. H. & Im, S. H. Highly efficient $CH_3NH_3PbI_{3-x}Cl_x$ mixed halide perovskite solar cells prepared by re-dissolution and crystal grain growth via spray coating. *Journal of Materials Chemistry A* **4**, 17636–17642 (2016).

61. Chern, Y.-C. *et al.* Grain structure control and greatly enhanced carrier transport by $CH_3NH_3PbCl_3$ interlayer in two-step solution processed planar perovskite solar cells. *Organic Electronics* **38**, 362–369 (2016).

62. Zhao, Y. & Zhu, K. CH_3NH_3Cl-Assisted One-Step Solution Growth of $CH_3NH_3PbI_3$: Structure, Charge-Carrier Dynamics, and Photovoltaic Properties of Perovskite Solar Cells. *The Journal of Physical Chemistry C* **118**, 9412–9418 (2014).

63. Wang, S.-Q. *et al.* Improving the phase stability of inorganic lead halide perovskites through K/Rb doping. *Applied Physics Express* **12**, 051017 (2019).

64. Burschka, J. *et al.* Sequential deposition as a route to high-performance perovskite-sensitized solar cells. *Nature* **499**, 316 (2013).

65. Wakamiya, A. *et al.* Reproducible Fabrication of Efficient Perovskite-based Solar Cells: X-ray Crystallographic Studies on the Formation of $CH_3NH_3PbI_3$ Layers. *Chemistry Letters* **43**, 711–713 (2014).

66. Lee, D. K., Jeong, D. N., Ahn, T. K. & Park, N. G. Precursor Engineering for a Large-Area Perovskite Solar Cell with >19% Efficiency. *ACS Energy Letters* **4**, 2393–2401 (2019).

67. Feng, M., You, S., Cheng, N. & Du, J. High quality perovskite film solar cell using methanol as additive with 19.5% power conversion efficiency. *Electrochimica Acta* **293**, 356–363 (2019).

68. Matsui, T., Seo, J.-Y., Saliba, M., Zakeeruddin, S. M. & Grätzel, M. Room-Temperature Formation of Highly Crystalline Multication Perovskites for Efficient, Low-Cost Solar Cells. *Advanced Materials* **29**, 1606258 (2017).

69. Eggers, H. *et al.* Inkjet-Printed Micrometer-Thick Perovskite Solar Cells with Large

Columnar Grains. *Advanced Energy Materials* **10**, 1903184 (2020).

70. Wang, Y. *et al.* Patterned Wettability Surface for Competition-Driving Large-Grained Perovskite Solar Cells. *Advanced Energy Materials* **9**, 1900838 (2019).

71. Mathies, F. *et al.* Multipass inkjet printed planar methylammonium lead iodide perovskite solar cells. *Journal of Materials Chemistry A* **4**, 19207–19213 (2016).

72. Wang, R. *et al.* Caffeine Improves the Performance and Thermal Stability of Perovskite Solar Cells. *Joule* **3**, 1–14 (2019).

73. Gong, X. *et al.* Controllable Perovskite Crystallization by Water Additive for High-Performance Solar Cells. *Advanced Functional Materials* **25**, 6671–6678 (2015).

74. Chen, W. *et al.* Conjugated Polymer–Assisted Grain Boundary Passivation for Efficient Inverted Planar Perovskite Solar Cells. *Advanced Functional Materials* **1808855**, 1808855 (2019).

75. Wang, Z. *et al.* Structured crystallization for efficient all-inorganic perovskite solar cells with high phase stability. *Journal of Materials Chemistry A* **7**, 20390–20397 (2019).

76. Nie, W. *et al.* High-efficiency solution-processed perovskite solar cells with millimeter-scale grains. *Science* **347**, 522–525 (2015).

77. Hu, H. *et al.* Nucleation and crystal growth control for scalable solution-processed organic–inorganic hybrid perovskite solar cells. *Journal of Materials Chemistry A* **8**, 1578–1603 (2020).

78. Zhang, K. *et al.* A prenucleation strategy for ambient fabrication of perovskite solar cells with high device performance uniformity. *Nature Communications* **11**, 1006 (2020).

79. Xie, F. *et al.* Vertical recrystallization for highly efficient and stable formamidinium-based inverted-structure perovskite solar cells. *Energy & Environmental Science* **10**, 1942–1949 (2017).

80. Cao, X. *et al.* Fabrication of Perovskite Films with Large Columnar Grains via Solvent-Mediated Ostwald Ripening for Efficient Inverted Perovskite Solar Cells. *ACS Applied Energy Materials* **1**, 868–875 (2018).

81. Wang, P. *et al.* Solvent-controlled growth of inorganic perovskite films in dry environment for efficient and stable solar cells. *Nature Communications* **9**, 2225 (2018).

82. Zhu, L. *et al.* Investigation on the role of Lewis bases in the ripening process of perovskite films for highly efficient perovskite solar cells †. *J. Mater. Chem. A* **5**, 20874–20881 (2017).

83. Huang, Z., Hu, X., Liu, C., Tan, L. & Chen, Y. Nucleation and Crystallization Control via

Polyurethane to Enhance the Bendability of Perovskite Solar Cells with Excellent Device Performance. *Advanced Functional Materials* **27**, 1703061 (2017).

84. Chen, G. *et al.* Crack-free $CH_3NH_3PbI_3$ layer via continuous dripping method for high-performance mesoporous perovskite solar cells. *Applied Surface Science* **392**, 960–965 (2017).

85. Ahn, N. *et al.* Highly Reproducible Perovskite Solar Cells with Average Efficiency of 18.3% and Best Efficiency of 19.7% Fabricated via Lewis Base Adduct of Lead(II) Iodide. *J. Am. Chem. Soc* **137**, 8696–8699 (2015).

86. Bai, Y. *et al.* A pure and stable intermediate phase is key to growing aligned and vertically monolithic perovskite crystals for efficient PIN planar perovskite solar cells with high processibility and stability. *Nano Energy* **34**, 58–68 (2017).

87. Best Research-Cell Photovoltaic Efficiency Chart. *NREL* https://www.nrel.gov/pv/cell-efficiency.html.

88. Kaltenbrunner, M. *et al.* Flexible high power-per-weight perovskite solar cells with chromium oxide-metal contacts for improved stability in air. *Nature Materials* **14**, 1032–1039 (2015).

89. Li, H. & Zhang, W. Perovskite Tandem Solar Cells: From Fundamentals to Commercial Deployment. *Chemical Reviews* **120**, 9835–9950 (2020).

90. Al-Ashouri, A. *et al.* Monolithic perovskite/silicon tandem solar cell with >29% efficiency by enhanced hole extraction. *Science* **370**, 1300–1309 (2020).

91. Wei, H. & Huang, J. Halide lead perovskites for ionizing radiation detection. *Nature Communications* **10**, 1066 (2019).

92. Xu, X. *et al.* Halide perovskites: A dark horse for direct X-ray imaging. *EcoMat* eom2.12064 (2020) doi:10.1002/eom2.12064.

93. Li, Z. *et al.* Halide perovskites for high-performance X-ray detector. *Materials Today* **48**, 155–175 (2021).

94. Wu, H., Ge, Y., Niu, G. & Tang, J. Metal Halide Perovskites for X-Ray Detection and Imaging. *Matter* **4**, 144–163 (2021).

95. Zhou, Y., Chen, J., Bakr, O. M. & Mohammed, O. F. Metal Halide Perovskites for X-ray Imaging Scintillators and Detectors. *ACS Energy Letters* **6**, 739–768 (2021).

96. He, Y., Hadar, I. & Kanatzidis, M. G. Detecting ionizing radiation using halide perovskite semiconductors processed through solution and alternative methods. *Nature Photonics* **16**, 14–26 (2022).

97. Kasap, S. O. X-ray sensitivity of photoconductors: application to stabilized a-Se. *Journal of Physics D: Applied Physics* **33**, 2853–2865 (2000).

98. del Sordo, S. *et al.* Progress in the Development of CdTe and CdZnTe Semiconductor Radiation Detectors for Astrophysical and Medical Applications. *Sensors* **9**, 3491–3526 (2009).

99. Yakunin, S. *et al.* Detection of X-ray photons by solution-processed lead halide perovskites. *Nature Photonics* **9**, 444–449 (2015).

100. Huang, Y. *et al.* A-site Cation Engineering for Highly Efficient $MAPbI_3$ Single-Crystal X-ray Detector. *Angewandte Chemie International Edition* **58**, 17834–17842 (2019).

101. Wang, X. *et al.* PIN Diodes Array Made of Perovskite Single Crystal for X-Ray Imaging. *physica status solidi (RRL) - Rapid Research Letters* **12**, 1800380 (2018).

102. Li, J. *et al.* Rubidium Doping to Enhance Carrier Transport in $CsPbBr_3$ Single Crystals for High-Performance X-Ray Detection. *ACS Applied Materials & Interfaces* **12**, 989–996 (2020).

103. Fu, R. *et al.* Stability Challenges for Perovskite Solar Cells. *ChemNanoMat* **5**, 253–265 (2019).

104. Niu, G., Guo, X. & Wang, L. Review of recent progress in chemical stability of perovskite solar cells. *Journal of Materials Chemistry A* **3**, 8970–8980 (2015).

105. Hu, Y., Qiu, T., Bai, F., Ruan, W. & Zhang, S. Highly Efficient and Stable Solar Cells with 2D $MA_3Bi_2I_9$/3D $MAPbI_3$ Heterostructured Perovskites. *Advanced Energy Materials* **8**, 1703620 (2018).

106. Noel, N. K. *et al.* Lead-free organic–inorganic tin halide perovskites for photovoltaic applications. *Energy & Environmental Science* **7**, 3061 (2014).

107. Nakamura, T. *et al.* Sn(IV)-free tin perovskite films realized by in situ Sn(0) nanoparticle treatment of the precursor solution. *Nature Communications* **11**, 3008 (2020).

108. Kim, J., Ho-Baillie, A. & Huang, S. Review of Novel Passivation Techniques for Efficient and Stable Perovskite Solar Cells. *Solar RRL* **3**, 1–16 (2019).

109. Matteocci, F. *et al.* Encapsulation for long-term stability enhancement of perovskite solar cells. *Nano Energy* **30**, 162–172 (2016).

110. McKenna, B., Troughton, J. R., Watson, T. M. & Evans, R. C. Enhancing the stability of organolead halide perovskite films through polymer encapsulation. *RSC Advances* **7**, 32942–32951 (2017).

111. Ramos, F. J. *et al.* Versatile perovskite solar cell encapsulation by low-temperature ALD-Al_2O_3 with long-term stability improvement. *Sustainable Energy & Fuels* **2**, 2468–2479 (2018).

112. Kim, H. *et al.* Enhanced Stability of $MAPbI_3$ Perovskite Solar Cells using Poly(p-chloro-xylylene) Encapsulation. *Scientific Reports* **9**, 15461 (2019).

113. Mohammadi, M. *et al.* Encapsulation Strategies for Highly Stable Perovskite Solar Cells under Severe Stress Testing: Damp Heat, Freezing, and Outdoor Illumination Conditions. *ACS Applied Materials & Interfaces* **13**, 45455–45464 (2021).

114. Kulbak, M., Cahen, D. & Hodes, G. How Important Is the Organic Part of Lead Halide Perovskite Photovoltaic Cells? Efficient $CsPbBr_3$ Cells. *The Journal of Physical Chemistry Letters* **6**, 2452–2456 (2015).

115. Bishop, J. E., Routledge, T. J. & Lidzey, D. G. Advances in Spray-Cast Perovskite Solar Cells. *The Journal of Physical Chemistry Letters* **9**, 1977–1984 (2018).

116. Fai, C. *et al.* $CsPbIBr_2$ Perovskite Solar Cell by Spray- Assisted Deposition. *ACS Energy Lett.* **1**, 573–577 (2016).

117. Barrows, A. T. *et al.* Efficient planar heterojunction mixed-halide perovskite solar cells deposited via spray-deposition. *Energy Environ. Sci.* **7**, 2944–2950 (2014).

118. Chang, W.-C., Lan, D.-H., Lee, K.-M., Wang, X.-F. & Liu, C.-L. Controlled Deposition and Performance Optimization of Perovskite Solar Cells Using Ultrasonic Spray-Coating of Photoactive Layers. *ChemSusChem* **10**, 1405–1412 (2017).

119. Duan, J. *et al.* Spray-assisted deposition of $CsPbBr_3$ films in ambient air for large-area inorganic perovskite solar cells. *Materials Today Energy* **10**, 146–152 (2018).

120. Das, S. *et al.* High-Performance Flexible Perovskite Solar Cells by Using a Combination of Ultrasonic Spray-Coating and Low Thermal Budget Photonic Curing. *ACS Photonics* **2**, 680–686 (2015).

121. Rocks, C., Svrcek, V., Maguire, P. & Mariotti, D. Understanding surface chemistry during $MAPbI_3$ spray deposition and its effect on photovoltaic performance. *Journal of Materials Chemistry C* **5**, 902–916 (2017).

122. Park, M. *et al.* Highly Reproducible Large-Area Perovskite Solar Cell Fabrication via Continuous Megasonic Spray Coating of $CH_3NH_3PbI_3$. *Small* **15**, 1804005 (2019).

123. Liang, Z. *et al.* A large grain size perovskite thin film with a dense structure for planar heterojunction solar cells via spray deposition under ambient conditions. *RSC Advances* **5**, 60562–60569 (2015).

124. Chen, S. *et al.* Stabilizing perovskite-substrate interfaces for high-performance perovskite modules. *Science* **373**, 902–907 (2021).

125. Mallajosyula, A. T. *et al.* Large-area hysteresis-free perovskite solar cells via temperature controlled doctor blading under ambient environment. *Applied Materials Today* **3**, 96–102 (2016).

126. Burkitt, D., Searle, J. & Watson, T. Perovskite solar cells in N-I-P structure with four slot-die-coated layers. *Royal Society Open Science* **5**, 172158 (2018).

127. Whitaker, J. B. *et al.* Scalable slot-die coating of high performance perovskite solar cells. *Sustainable Energy & Fuels* **2**, 2442–2449 (2018).

128. Yang, Z. *et al.* Slot-die coating large-area formamidinium-cesium perovskite film for efficient and stable parallel solar module. *Science Advances* **7**, 1–14 (2021).

129. Li, J. *et al.* 20.8% Slot-Die Coated $MAPbI_3$ Perovskite Solar Cells by Optimal DMSO-Content and Age of 2-ME Based Precursor Inks. *Advanced Energy Materials* **11**, 2003460 (2021).

130. Wang, X. *et al.* Solution-Processed Halide Perovskite Single Crystals with Intrinsic Compositional Gradients for X-ray Detection. *Chemistry of Materials* **32**, 4973–4983 (2020).

131. Wei, W. *et al.* Monolithic integration of hybrid perovskite single crystals with heterogenous substrate for highly sensitive X-ray imaging. *Nature Photonics* **11**, 315–321 (2017).

132. Wang, X. *et al.* Low-noise X-ray PIN photodiodes made of perovskite single crystals by solution-processed dopant incorporated epitaxial growth. *Nano Energy* **89**, 106311 (2021).

133. Faheem, M. B. *et al.* All-Inorganic Perovskite Solar Cells: Energetics, Key Challenges, and Strategies toward Commercialization. *ACS Energy Letters* **5**, 290–320 (2020).

134. Greul, E., Petrus, M. L., Binek, A., Docampo, P. & Bein, T. Highly stable, phase pure $Cs_2AgBiBr_6$ double perovskite thin films for optoelectronic applications. *Journal of Materials Chemistry A* **5**, 19972–19981 (2017).

135. Tang, M. *et al.* Toward efficient and air-stable carbon-based all-inorganic perovskite solar cells through substituting $CsPbBr_3$ films with transition metal ions. *Chemical Engineering Journal* **375**, 121930 (2019).

136. Duan, J., Wang, Y., Yang, X. & Tang, Q. Alkyl-Chain-Regulated Charge Transfer in Fluorescent Inorganic $CsPbBr_3$ Perovskite Solar Cells. *Angewandte Chemie International Edition* **59**, 4391–4395 (2020).

137. Duan, J., Zhao, Y., He, B. & Tang, Q. High-Purity Inorganic Perovskite Films for Solar Cells with 9.72 % Efficiency. *Angewandte Chemie International Edition* **57**, 3787–3791 (2018).

138. Zhou, Q., Duan, J., Yang, X., Duan, Y. & Tang, Q. Interfacial Strain Release from the $WS_2/CsPbBr_3$ van der Waals Heterostructure for 1.7 V Voltage All-Inorganic Perovskite Solar Cells. *Angewandte Chemie* **132**, 22181–22185 (2020).

139. Duan, J., Zhao, Y., Wang, Y., Yang, X. & Tang, Q. Hole-Boosted $Cu(Cr,M)O_2$ Nanocrystals for All-Inorganic $CsPbBr_3$ Perovskite Solar Cells. *Angewandte Chemie International Edition* **58**, 16147–16151 (2019).

140. Zhao, Y., Duan, J., Wang, Y., Yang, X. & Tang, Q. Precise stress control of inorganic perovskite films for carbon-based solar cells with an ultrahigh voltage of 1.622 V. *Nano Energy* **67**, 104286 (2020).

141. Ou, Z. *et al.* Improvement of $CsPbBr_3$ photodetector performance by tuning the morphology with PMMA additive. *Journal of Alloys and Compounds* **821**, 153344 (2020).

142. Li, C. *et al.* Enhanced photoresponse of self-powered perovskite photodetector based on ZnO nanoparticles decorated $CsPbBr_3$ films. *Solar Energy Materials and Solar Cells* **172**, 341–346 (2017).

143. Saidaminov, M. I. *et al.* Inorganic Lead Halide Perovskite Single Crystals: Phase-Selective Low-Temperature Growth, Carrier Transport Properties, and Self-Powered Photodetection. *Advanced Optical Materials* **5**, 1600704 (2017).

144. Yang, Z. *et al.* Spray-Coated $CsPbBr_3$ Quantum Dot Films for Perovskite Photodiodes. *ACS Applied Materials & Interfaces* **10**, 26387–26395 (2018).

145. Zeng, J. *et al.* Space-Confined Growth of $CsPbBr_3$ Film Achieving Photodetectors with High Performance in All Figures of Merit. *Advanced Functional Materials* **28**, 1804394 (2018).

146. Feng, Y. *et al.* Low defects density $CsPbBr_3$ single crystals grown by an additive assisted method for gamma-ray detection. *Journal of Materials Chemistry C* **8**, 11360–11368 (2020).

147. He, Y. *et al.* $CsPbBr_3$ perovskite detectors with 1.4% energy resolution for high-energy γ-rays. *Nature Photonics* **15**, 36–42 (2021).

148. Xu, Q. *et al.* $CsPbBr_3$ Single Crystal X-ray Detector with Schottky Barrier for X-ray Imaging Application. *ACS Applied Electronic Materials* **2**, 879–884 (2020).

149. Forth, L. J. *et al.* Sensitive X-ray Detectors Synthesised from $CsPbBr_3$. in *2019 IEEE*

Nuclear Science Symposium and Medical Imaging Conference (NSS/MIC) 1–5 (IEEE, 2019). doi:10.1109/NSS/MIC42101.2019.9059728.

150. Fan, Z. *et al.* Solution-Processed $MAPbBr_3$ and $CsPbBr_3$ Single-Crystal Detectors with Improved X-Ray Sensitivity via Interfacial Engineering. *physica status solidi (a)* **217**, 2000104 (2020).

151. Stoumpos, C. C. *et al.* Crystal Growth of the Perovskite Semiconductor $CsPbBr_3$: A New Material for High-Energy Radiation Detection. *Crystal Growth & Design* **13**, 2722–2727 (2013).

152. Clinckemalie, L. *et al.* Challenges and Opportunities for $CsPbBr_3$ Perovskites in Low- and High-Energy Radiation Detection. *ACS Energy Letters* **6**, 1290–1314 (2021).

153. Li, X. *et al.* All-Inorganic $CsPbBr_3$ Perovskite Solar Cells with 10.45% Efficiency by Evaporation-Assisted Deposition and Setting Intermediate Energy Levels. *ACS Applied Materials & Interfaces* **11**, 29746–29752 (2019).

154. Gou, Z. *et al.* Self-Powered X-Ray Detector Based on All-Inorganic Perovskite Thick Film with High Sensitivity Under Low Dose Rate. *physica status solidi (RRL) – Rapid Research Letters* **13**, 1900094 (2019).

155. Pan, W. *et al.* Hot-Pressed $CsPbBr_3$ Quasi-Monocrystalline Film for Sensitive Direct X-ray Detection. *Advanced Materials* **31**, 1904405 (2019).

156. Matt, G. J. *et al.* Sensitive Direct Converting X-Ray Detectors Utilizing Crystalline $CsPbBr_3$ Perovskite Films Fabricated via Scalable Melt Processing. *Advanced Materials Interfaces* **7**, 1901575 (2020).

157. Yin, L. *et al.* Controlled Cooling for Synthesis of $Cs_2AgBiBr_6$ Single Crystals and Its Application for X-Ray Detection. *Advanced Optical Materials* **7**, 1900491 (2019).

158. Steele, J. A. *et al.* Photophysical Pathways in Highly Sensitive $Cs_2AgBiBr_6$ Double-Perovskite Single-Crystal X-Ray Detectors. *Advanced Materials* **30**, 1804450 (2018).

159. Zhang, H. *et al.* X-Ray Detector Based on All-Inorganic Lead-Free $Cs_2AgBiBr_6$ Perovskite Single Crystal. *IEEE Transactions on Electron Devices* **66**, 2224–2229 (2019).

160. Yuan, W. *et al.* In Situ Regulating the Order–Disorder Phase Transition in $Cs_2AgBiBr_6$ Single Crystal toward the Application in an X-Ray Detector. *Advanced Functional Materials* **29**, 1900234 (2019).

161. Li, H. *et al.* Lead-free halide double perovskite-polymer composites for flexible X-ray imaging. *Journal of Materials Chemistry C* **6**, 11961–11967 (2018).

162. Yang, B. *et al.* Heteroepitaxial passivation of $Cs_2AgBiBr_6$ wafers with suppressed ionic

migration for X-ray imaging. *Nature Communications* **10**, 1989 (2019).

163. Zhang, H. *et al.* Encapsulated X-Ray Detector Enabled by All-Inorganic Lead-Free Perovskite Film With High Sensitivity and Low Detection Limit. *IEEE Transactions on Electron Devices* **67**, 3191–3198 (2020).

164. Kawaharamura, T. *et al.* Mist CVD Growth of ZnO-Based Thin Films and Nanostructures. *Journal of the Korean Physical Society* **53**, 2976–2980 (2008).

165. Fujita, S. Mist deposition technology as a green route for thin film growth. *Proceedings of AM-FPD 2014 - The 21st International Workshop on Active-Matrix Flatpanel Displays and Devices: TFT Technologies and FPD Materials* 53–56 (2014) doi:10.1109/AM-FPD.2014.6867120.

166. Kim, B. H., Lee, J. Y., Choa, Y. H., Higuchi, M. & Mizutani, N. Preparation of TiO_2 thin film by liquid sprayed mist CVD method. *Materials Science and Engineering B: Solid-State Materials for Advanced Technology* **107**, 289–294 (2004).

167. Okuno, T., Oshima, T., Lee, S. D. & Fujita, S. Growth of SnO_2 crystalline thin films by mist chemical vapour deposition method. *Physica Status Solidi (C) Current Topics in Solid State Physics* **8**, 540–542 (2011).

168. Ikenoue, T. & Fujita, S. Thin Film Formation of Transparent Conductive Oxides by Solution-Based Mist Deposition Method toward Hybrid Device Applications. *MRS Proceedings* **1400**, mrsf11-1400-s02-05 (2012).

169. Ikenoue, T., Kameyama, N. & Fujita, S. Fabrication of PEDOT:PSS/ZnMgO Schottky-type ultraviolet sensors on glass substrates with solution-based mist deposition technique and hard-mask patterning. *physica status solidi (c)* **8**, 613–615 (2011).

170. Ikenoue, T., Sakamoto, S. & Inui, Y. Fabrication and characterization of Cu_2O, ZnO and ITO thin films toward oxide thin film solar cell by mist chemical vapor deposition method. *physica status solidi (c)* **11**, 1237–1239 (2014).

171. Ikenoue, T., Nishinaka, H. & Fujita, S. Fabrication of conducting poly(3,4-ethylenedioxythiophene): poly(styrenesulfonate) thin films by ultrasonic spray-assisted mist deposition method. *Thin Solid Films* **520**, 1978–1981 (2012).

172. Lee, J.-H., Yoshikawa, S. & Sagawa, T. Fabrication of efficient organic and hybrid solar cells by fine channel mist spray coating. *Solar Energy Materials and Solar Cells* **127**, 111–121 (2014).

Chapter 2
Mist Deposition Method for $CsPbBr_3$ films

2.1 Introduction

The mist deposition method has track records for scalable deposition of metal oxides and organic semiconductors.[1–9] However, there were no reports on the fabrication of all-inorganic perovskites. Although there is one report on the fabrication of organic-inorganic hybrid perovskite ($MAPbBr_{3-x}Cl_x$) films via the mist deposition method,[7] the systematic investigation to fabricate high-quality films are not enough. To proceed with the practical application, not only just to fabricate by scalable processes but also to improve the film quality is required. In this chapter, the author aims to demonstrate the fabrication of all-inorganic perovskite ($CsPbBr_3$) films via the mist deposition method. The effects of fabrication conditions are investigated to establish the way to prepare the all-inorganic films with high carrier transport properties.

2.2 Experimentals

Materials

CsBr (99.999%) and $PbBr_2$ (99.999%) were purchased from Sigma-Aldrich. *N, N*-dimethylformamide (DMF, 99.5%) and dimethyl sulfoxide (DMSO, 99.0%) were purchased from Fujifilm Wako.

Mist deposition of $CsPbBr_3$ films

A precursor solution, which was prepared by dissolving 50 mM CsBr and 50 mM $PbBr_2$ in a solvent mixture of DMSO and DMF, was atomized to the mist by 2.4 MHz ultrasonic vibration. This mist was then transported by nitrogen gas and injected from a nozzle with a rectangular aperture (30 × 1 mm^2) to the pre-heated glass substrate (130–190 °C) as a curtain-

like flow. The carrier gas flow rate and dilution gas flow rate were set at 0.4 and 4.6 L min^{-1}, respectively. $CsPbBr_3$ can be uniformly deposited over a wide area by passing the substrate under the mist flow at a constant speed. In this chapter, $CsPbBr_3$ was deposited onto a reduced area of 25 × 6 mm^2 by moving the substrate by 6 mm at a speed of 0.16 mm s^{-1}. The deposition cycle was repeated to give a thick $CsPbBr_3$ film.

Characterization

X-ray diffraction (XRD) spectra of $CsPbBr_3$ films were recorded using a PW 3040/60 X'Pert PRO with Cu-Kα radiation. Cross-sections of the films were observed with scanning electron microscopy (SEM; JSM-6510LV, JEOL). To investigate the carrier transport properties, a Pt/$CsPbBr_3$/carbon structure was fabricated as follows: a Pt thin film as an ohmic electrode was formed on an ITO/glass substrate (25 × 20 mm^2) by sputtering deposition. The $CsPbBr_3$ film was deposited onto the Pt film at 150 °C in the same way as the fabrication on glass substrates. Finally, a circular carbon ohmic electrode was deposited onto the $CsPbBr_3$ film by painting carbon ink and heating at 100 °C for 10 min. This process was chosen to prevent the $CsPbBr_3$ film from being damaged by heat or incident particles with high energy. The active area was measured to be 0.07 cm^2. The dark current density-voltage curve was measured with a Keithley 2400 Source Meter. In this measurement, carbon and Pt electrodes served as the anode and cathode, respectively.

2.3 Results and Discussion

2.3.1 Selection of Solvents for Precursor Solution

Suitable solvents for the preparation of $CsPbBr_3$ films are investigated. In the mist deposition method, the precursor solution must be atomized by ultrasonic vibration. Thus, the solvent should have a suitable viscosity. Additionally, the solvent should be able to dissolve as much of the precursor as possible. Because the solvent volatilizes during transportation, supersaturation and precipitates may occur before the precursor solution reaches the substrate. To avoid this, a margin of saturation concentration is required. From the above, the solvent used for the precursor solution should have a viscosity suitable for atomization and high solubility of the precursor.

Dimethyl sulfoxide (DMSO) and *N, N*-dimethylformamide (DMF) are representative organic solvents used for the perovskite precursor solution. The viscosity and solubility of $CsPbBr_3$ are listed in Table 2-1. DMSO can dissolve 500 mM of $CsPbBr_3$ and therefore it is commonly used to prepare $CsPbBr_3$ solution. However, its viscosity is as high as 2.00 cP, making it difficult to atomize. On the other hand, the viscosity of DMF is 0.80 cP, which is close to the viscosity of water (0.89 cP), and atomization is easy. However, when 100 mM of CsBr and $PbBr_2$ were added in DMF, orange precipitates immediately appeared and remained even after stirring for more than a day (Figure 2-1a). Herein, a mixture of DMSO and DMF is used to achieve both suitable viscosity and enough solubility. The viscosity of the DMSO-DMF solvent decreased with an increasing DMF ratio (Figure 2-1b). The amounts of generated mist particles increased by using the solvent mixture DMSO-DMF mixture (Figure 2-1c–e). Based on the above discussion, DMSO-DMF (1:1, volume ratio) mixture solvents are selected for the preparation of $CsPbBr_3$ films.

Table 2-1| Viscosity and solubility of $CsPbBr_3$ of DMSO and DMF.

Solvent	Viscosity at 25 °C (cP)	Solubility of $CsPbBr_3$ (mM)
DMSO	2.00	~500
DMF	0.80	<100

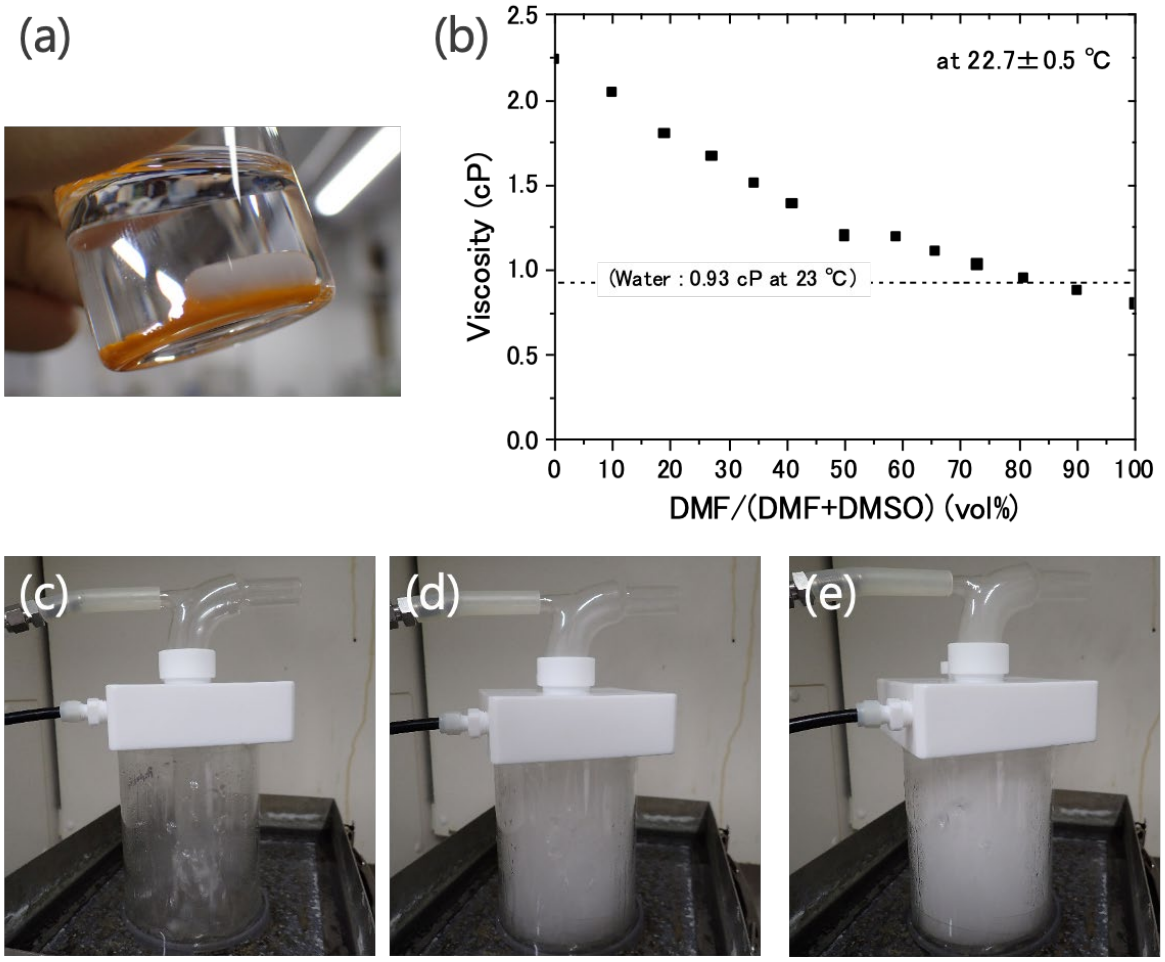

Figure 2-1| (a) A photograph of a solution prepared by adding 100 mM of $CsPbBr_3$ in DMF. (b) Viscosities of DMSO–DMF mixtures vs. the DMF/(DMSO+DMF) volume ratio. (c)–(e) Photographs of ultrasonic atomization of (c) DMSO (d) DMSO-DMF (1:3, *v/v*) (e) DMSO-DMF (1:1, *v/v*).

2.3.2 Effects of Substrate Temperature

Figure 2-2a–d shows photographs of $CsPbBr_3$ films formed on glass substrates at various substrate temperatures (130–190 °C) to examine the temperature dependence. Clear orange-colored films were obtained at 150–170 °C, while frosted films were obtained at 130 and 190 °C. The cross-sectional SEM images (Figure 2-2e–h) showed that the films formed at 150–170 °C were composed of closely packed columnar crystals with diameters of 1–2 μm, whereas those at lower and higher temperatures (130 and 190 °C) were composed of rough grains, corresponding to clear or frosted appearances (Figure 2-2a–d). When the substrate temperature was set at 150–170 °C, the supply of precursor solution and solvent evaporation seemed to be well-balanced, resulting in the formation of high-quality films. The XRD patterns of the films corresponded to that of orthorhombic $CsPbBr_3$ [10] (Figure 2-2i). It is known that $CsPbBr_3$ exists in an orthorhombic structure at room temperature, with phase transitions to tetragonal and cubic structures at 88 °C and 130 °C, respectively.[10] The films can be identified as an orthorhombic structure due to the specific peaks, such as (201) at $2\theta = 24.2°$. The bandgap of the film derived from the visible absorption spectrum (Figure 2-2j) was 2.33 eV, in agreement with the value reported for $CsPbBr_3$.[11–13] These results showed that $CsPbBr_3$ films were indeed obtained using the mist deposition method. Interestingly, the films formed at 150–170 °C were composed of highly (101)-oriented columnar crystals (Figure 2-2f, g, and i). Columnar growth should be preferable because it creates few grain boundaries that cross the charge collection route, thus 150 °C was selected as the substrate temperature in the following sections.

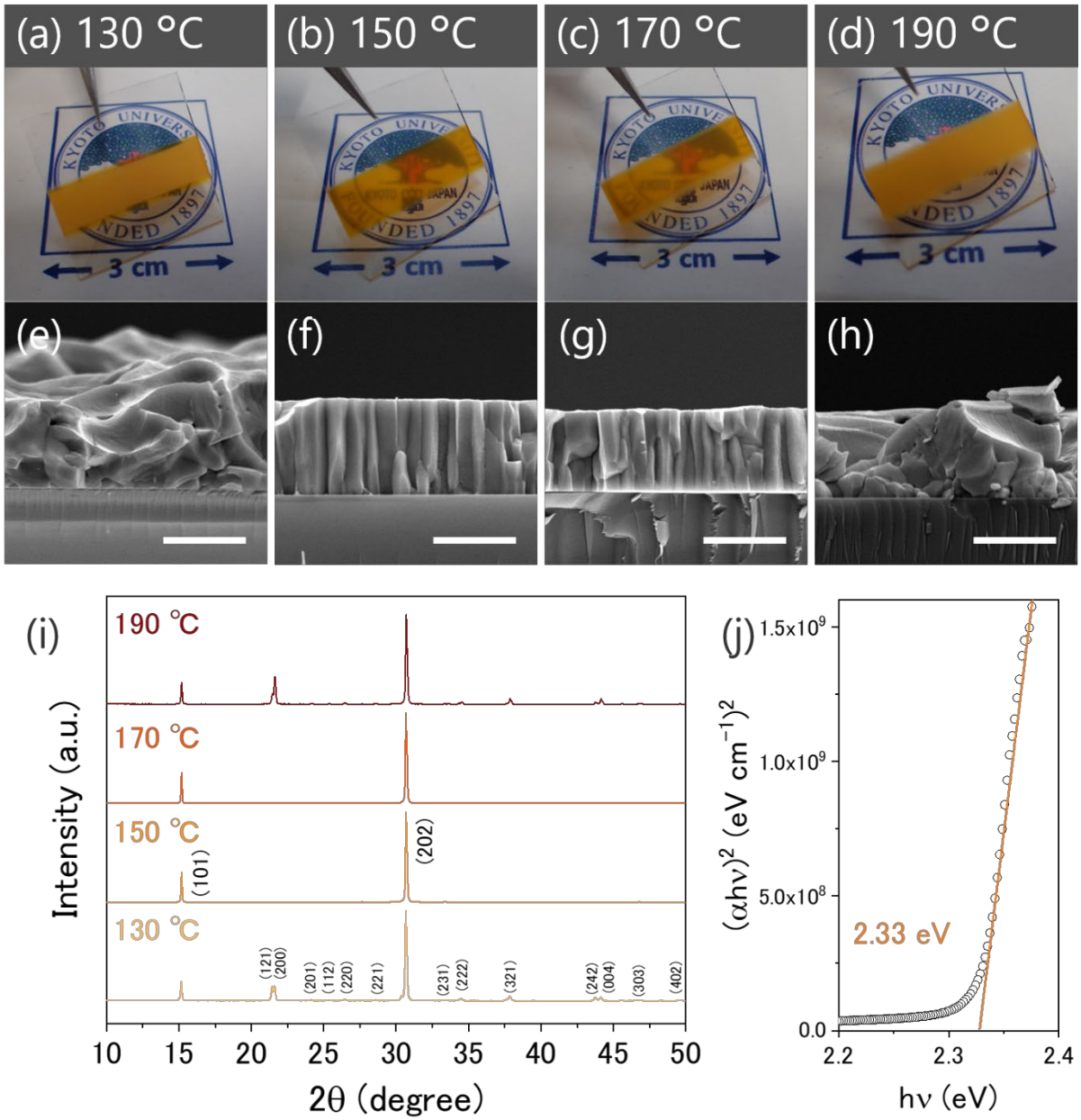

Figure 2-2| (a)–(d) Photographs and (e)–(h) cross-sectional SEM images of the $CsPbBr_3$ films formed at (a, e) 130, (b, f) 150, (c, g) 170, and (d, h) 190 °C. Scale bars are 5 μm. (i) XRD patterns of films formed at 130–190 °C, (j) Tauc plot for the film formed at 150 °C.

2.3.3 Increase of Film Thickness and Evaluation of Charge Transport Properties

The number of deposition cycles (*N*) was increased to fabricate thick $CsPbBr_3$ films. The film thickness increased in proportion to the number of deposition cycles (Figure 2-3a), showing that the film thickness was controlled effectively in this method. In addition, columnar crystals continued growing while maintaining their structure (Figure 2-3b–d).

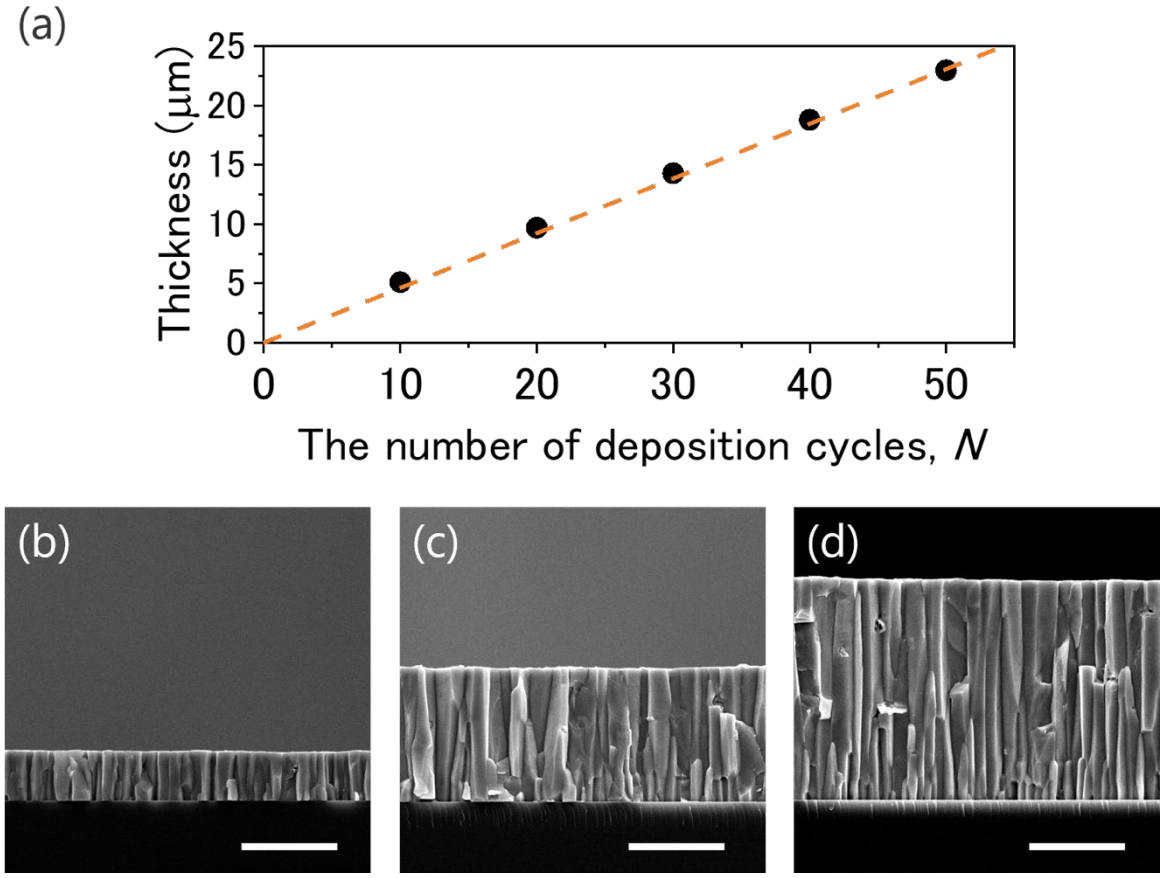

Figure 2-3| (a) Relation between the film thickness and the number of deposition cycles, *N*, (b)–(d) cross-sectional SEM images of films formed at deposition cycles of (b) 10, (c) 30, and (d) 50. Scale bars are 10 μm.

The carrier transport properties of the $CsPbBr_3$ film in the direction vertical to the substrates were determined through space-charge limited current (SCLC) measurements[14] with an ohmic device (Pt/$CsPbBr_3$/Carbon). In the current density-voltage ($J \approx V^n$) curve, ohmic ($n = 1$), trap-filling (TFL, $n > 3$), and Child ($n = 2$) regions were observed (Figure 2-4). The resistivity (R) was calculated from the ohmic region, and the trap density (n_{trap}) was calculated using the equation:

$$n_{\mathrm{trap}} = \frac{2V_{\mathrm{TFL}}\varepsilon\varepsilon_0}{eL^2} \qquad (1)$$

where V_{TFL} is the trap-filled limit voltage, L is the film thickness of 27.7 μm (measured from cross-sectional SEM image of this sample), ε_0 is the vacuum permittivity, e is the electron charge, and ε is the relative dielectric constant for $CsPbBr_3$ (~23.9).[12] The mobility (μ) was calculated from the Child region following Mott-Gurney's equation:

$$\mu = \frac{8J_D L^3}{9\varepsilon\varepsilon_0 V^2} \qquad (2)$$

where J_D is the current density. The results of the SCLC measurements are summarized in Table 2-2 with previous reports. The resistivity (R) is 1.4 GΩ cm, which is comparable to that for solution-grown $CsPbBr_3$ SCs[15,16] and expected to contribute to the suppression of noise current. The trap-filled limit voltage (V_{TFL}) is 0.37 V for this sample and the trap density (n_{trap}) calculated from Equation (1) is 1.3×10^{12} cm^{-3}, which is relatively higher than that for $CsPbBr_3$ SCs but much lower than that for polycrystalline films.[17,18] In addition, the mobility (μ) calculated from Equation (2) is 13 $cm^2\ V^{-1}\ s^{-1}$, which is comparable to that for $CsPbBr_3$ SCs[12,15] and higher than that for high-quality $CsPbBr_3$ thin films.[17] Generally, the mobility of polycrystalline films is lower than that for single crystals due to the grain boundaries. In the case of $CH_3NH_3PbI_2Cl$ polycrystalline films, the dramatical deterioration of the mobility with increasing grain boundaries has been reported.[19] However, the $CsPbBr_3$ films fabricated by the mist deposition method had high carrier mobility. We speculate that reason as follows. As shown in the inset of Figure 2-4, in the (101)-oriented $CsPbBr_3$ films, the $[PbBr_6]^{4-}$ octahedrons align in the direction of charge collection and the Br-Pb-Br continuous bonds form straight chains, leading to

effective carrier transport.[12] In addition, the columnar growth created few grain boundaries to disturb carrier transport. Both (101)-orientation and columnar growth seemed to contribute to the high carrier mobility.

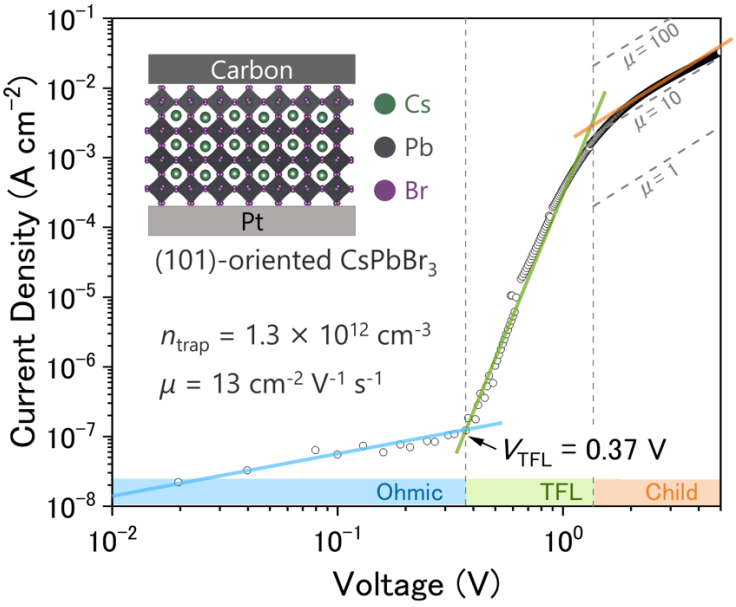

Figure 2-4| Dark current density-voltage characteristics of a $CsPbBr_3$ film.

Table 2-2| Carrier transport properties comparisons of $CsPbBr_3$ from previous reports.

Method	Structure	Size	R [GΩ cm]	n_{trap} [cm^{-3}] electron / hole	μ [$cm^2 V^{-1} s^{-1}$] electron / hole	Ref.
Bridgman	SC	φ 24 mm × 90 mm	–	1.08×10^9 / –	11.61 / –	12
Bridgman	SC	φ25 mm × 70 mm	–	– / 1.2×10^9	2290 / 2060	20
ITC*	SC	3 mm × 2 mm × 1 mm	0.1	1.1×10^{10} / 4.2×10^{10}	52 / 11	15
AVC**	SC	42 mm × 5 mm × 3 mm	2.1	–	– / 143	16
Spin-coating	thin film	–	–	1.40×10^{16}	–	18
Spin-coating	porous film	40 mm × 40 mm × <1 μm	–	3.07×10^{12}	9.27	17
Mist deposition	thick film	25 mm × 6 mm × 28 μm	1.4	1.3×10^{12}	13	This work

*ITC: Inverse temperature crystallization, **AVC: Anti-solvent vapor-assisted crystallization

2.4 Conclusions

In conclusion, the mist deposition method was successfully applied for the fabrication of $CsPbBr_3$ films. Highly (101)-oriented $CsPbBr_3$ films composed of columnar crystals were obtained in a temperature range of 150–170 °C. Furthermore, the film thickness was controlled and upscaled in the range of 5–28 μm by the number of deposition cycles. The $CsPbBr_3$ film had excellent carrier transport properties comparable to single crystals, such as the mobility of 13 $cm^2 V^{-1} s^{-1}$, the trap density of 1.3×10^{12} cm^{-3}. Especially, the trap density is much lower than that for polycrystalline films fabricated by conventional spin-coating method. These results demonstrated that the mist deposition method can produce high-quality $CsPbBr_3$ films. In Chapter 3 and Chapter 4, the device applications for solar cells and X-ray detectors using $CsPbBr_3$ films are investigated.

References for Chapter 2

1. Fujita, S. Mist deposition technology as a green route for thin film growth. Proceedings of AM-FPD 2014 - The 21st International Workshop on Active-Matrix Flatpanel Displays and Devices: TFT Technologies and FPD Materials 53–56 (2014) doi:10.1109/AM-FPD.2014.6867120.

2. Kim, B. H., Lee, J. Y., Choa, Y. H., Higuchi, M. & Mizutani, N. Preparation of TiO_2 thin film by liquid sprayed mist CVD method. Materials Science and Engineering B: Solid-State Materials for Advanced Technology **107**, 289–294 (2004).

3. Okuno, T., Oshima, T., Lee, S. D. & Fujita, S. Growth of SnO_2 crystalline thin films by mist chemical vapour deposition method. Physica Status Solidi (C) Current Topics in Solid State Physics **8**, 540–542 (2011).

4. Lee, J.-H., Yoshikawa, S. & Sagawa, T. Fabrication of efficient organic and hybrid solar cells by fine channel mist spray coating. Solar Energy Materials and Solar Cells **127**, 111–121 (2014).

5. Ikenoue, T., Nishinaka, H. & Fujita, S. Fabrication of conducting poly(3,4-ethylenedioxythiophene): poly(styrenesulfonate) thin films by ultrasonic spray-assisted mist deposition method. Thin Solid Films **520**, 1978–1981 (2012).

6. Ikenoue, T. & Fujita, S. Thin Film Formation of Transparent Conductive Oxides by Solution-Based Mist Deposition Method toward Hybrid Device Applications. MRS Proceedings **1400**, mrsf11-1400-s02-05 (2012).

7. Nishinaka, H. & Yoshimoto, M. Solution-based mist CVD technique for $CH_3NH_3Pb(Br_{1-x}Cl_x)_3$ inorganic–organic perovskites. Japanese Journal of Applied Physics **55**, 100308 (2016).

8. Ikenoue, T., Sakamoto, S. & Inui, Y. Fabrication and characterization of Cu_2O, ZnO and ITO thin films toward oxide thin film solar cell by mist chemical vapor deposition method. physica status solidi (c) **11**, 1237–1239 (2014).

9. Ikenoue, T., Kameyama, N. & Fujita, S. Fabrication of PEDOT:PSS/ZnMgO Schottky-type ultraviolet sensors on glass substrates with solution-based mist deposition technique and hard-mask patterning. physica status solidi (c) **8**, 613–615 (2011).

10. Stoumpos, C. C. et al. Crystal Growth of the Perovskite Semiconductor $CsPbBr_3$: A New Material for High-Energy Radiation Detection. Crystal Growth & Design **13**, 2722–2727 (2013).

11. Kulbak, M., Cahen, D. & Hodes, G. How Important Is the Organic Part of Lead Halide

Perovskite Photovoltaic Cells? Efficient $CsPbBr_3$ Cells. The Journal of Physical Chemistry Letters **6**, 2452–2456 (2015).

12. Zhang, P. et al. Anisotropic Optoelectronic Properties of Melt-Grown Bulk $CsPbBr_3$ Single Crystal. The Journal of Physical Chemistry Letters **9**, 5040–5046 (2018).

13. He, Y. et al. High spectral resolution of gamma-rays at room temperature by perovskite $CsPbBr_3$ single crystals. Nature Communications **9**, 1609 (2018).

14. Bube, R. H. Trap Density Determination by Space-Charge-Limited Currents. Journal of Applied Physics **33**, 1733–1737 (1962).

15. Saidaminov, M. I. et al. Inorganic Lead Halide Perovskite Single Crystals: Phase-Selective Low-Temperature Growth, Carrier Transport Properties, and Self-Powered Photodetection. Advanced Optical Materials **5**, 1600704 (2017).

16. Zhang, H. et al. Centimeter-Sized Inorganic Lead Halide Perovskite $CsPbBr_3$ Crystals Grown by an Improved Solution Method. Crystal Growth & Design **17**, 6426–6431 (2017).

17. Zeng, J. et al. Space-Confined Growth of $CsPbBr_3$ Film Achieving Photodetectors with High Performance in All Figures of Merit. Advanced Functional Materials **28**, 1804394 (2018).

18. Feng, J. et al. Crystallographically Aligned Perovskite Structures for High-Performance Polarization-Sensitive Photodetectors. Advanced Materials **29**, 1605993 (2017).

19. Nie, W. et al. High-efficiency solution-processed perovskite solar cells with millimeter-scale grains. Science **347**, 522–525 (2015).

20. Song, J. et al. Ultralarge All-Inorganic Perovskite Bulk Single Crystal for High-Performance Visible-Infrared Dual-Modal Photodetectors. Advanced Optical Materials **5**, 1700157 (2017).

Chapter 3
$CsPbBr_3$-Based Perovskite Solar Cells

3.1 Introduction

In Chapter 2, the uniform $CsPbBr_3$ films with the thickness range of 5–28 μm were successfully fabricated by the mist deposition method. If the uniformity is kept even for thin-film fabrication, the mist deposition method may solve the conventional problem in solar cell applications: full-coverage coating of $CsPbBr_3$ thin films (~500 nm) via a one-step solution method is difficult. The significance of the mist deposition method for $CsPbBr_3$ solar cells are described in detail as follows:

As described in Chapter 1, the all-inorganic perovskite is expected for solar cell applications thanks to its high stability.[1,2] Especially, carbon-based perovskite solar cells (PSCs), which eliminate the need for precious metal electrodes and hole transport layers, have demonstrated improved stability and reduced fabrication cost.[3–5] Following this trend, new type PSCs incorporating extremely durable carbon electrodes and $CsPbBr_3$ were proposed and demonstrated great stability.[6] Owing to its reduced fabrication cost and high stability, this state-of-the-art PSC is one of the most practical PSCs.

Since the first carbon-based $CsPbBr_3$ PSCs were reported in 2016,[6] their power conversion efficiencies (PCEs) have improved from 6.7% to more than 10% through various efforts such as interface engineering[7–12] and compositional engineering.[13–15] Despite these attempts at improving the PCE, there has been insufficient progress in developing solution processes for their industrialization. Although $CsPbBr_3$ thin films have been prepared by two-step spin-coating methods involving $PbBr_2$ preparation and its subsequent conversion to $CsPbBr_3$ with a CsBr solution, these methods require precise compositional control to suppress the formation of impurity phases such as Cs_4PbBr_6 and $CsPb_2Br_5$ during the second step.[7] In contrast, simple one-step methods that can directly form $CsPbBr_3$ from the precursor solution is preferable for

industrialization. In the one-step method, however, the $CsPbBr_3$ films often suffer from poor coverage because the density of the heterogeneous nuclei tends to be low owing to the poor solubility of CsBr in typical organic solvents, such as dimethyl sulfoxide (DMSO).[16–19]

To increase the density of heterogeneous nuclei, Y. Ren *et al.* proposed a fast nucleation-deposition method by introducing polyethylene glycol (PEG) in a one-step solution.[18] They revealed that the PEG increases the cluster number of CsBr-$PbBr_2$-DMSO-PEG colloids in the solution. These colloids serve as a nucleation site and induce fast nucleation-deposition. Consequently, the surface coverage of the $CsPbBr_3$ film was drastically improved. The obtained $CsPbBr_3$-based PSCs achieved a stabilized PCE of 7.2%, which is the highest efficiency recorded in the one-step method.[18] However, the PCE is still lower than those in the case of the two-step methods. Although the improved film coverage should improve the PCE, the residual additives within the $CsPbBr_3$ films may limit the photovoltaic performance.

Herein, the author proposes the mist deposition method as a one-step method to realize fast nucleation-deposition without any additives for the preparation of full-coverage $CsPbBr_3$ thin films. Figure 3-1 shows a schematic illustration of the proposed concept. In this method, the precursor solution is atomized into numerous mist particles by a 2.4 MHz ultrasonic vibration. This high frequency generates small droplets with a size of 3 μm (volume ~14 fL)[20] which is much smaller than that generated by air-brush (> size: 50 μm, volume: ~65 pL).[21] Therefore, as soon as the mist particles contact a preheated substrate, solvent evaporation and consequent fast nucleation-deposition should occur. Based on this hypothesis, at the initial stage of the deposition process, the numerous mist particles reaching the substrate one after another should repeat numerous fast nucleation-deposition, leading to a high density of heterogeneous nuclei. At the second stage, i.e. when the following mist particles adhere to the existing crystals, the re-dissolution and crystal grain growth should occur as reported in a previous study.[22] It is expected that the film coverage would improve gradually and full-coverage $CsPbBr_3$ films are finally obtained after repeated crystal grain growth and additional nucleation.

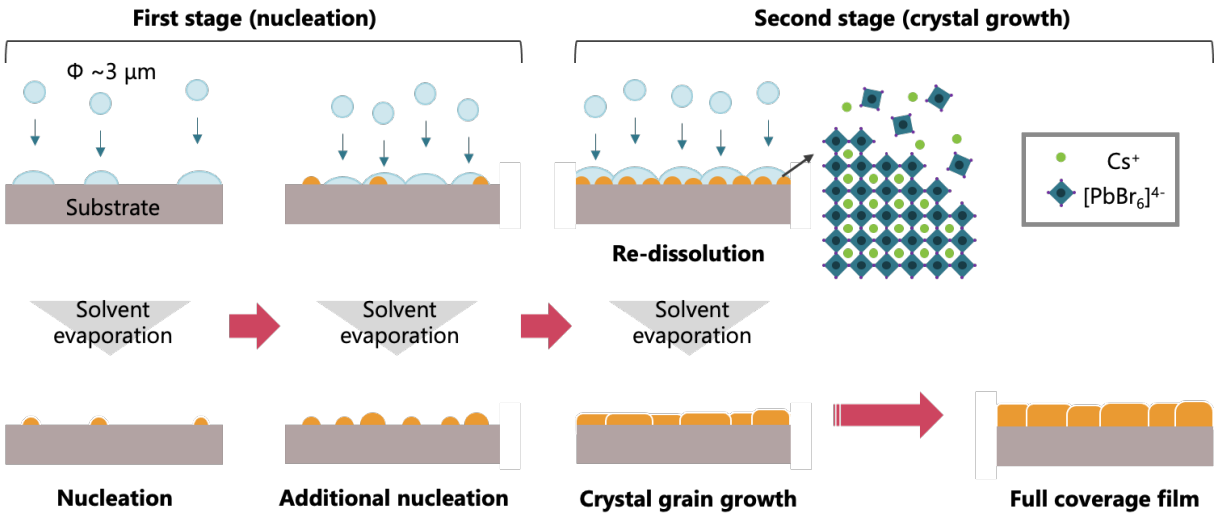

Figure 3-1| Schematic illustration of full coverage $CsPbBr_3$ film preparation by using mist deposition.

3.2 Experimentals

Materials

Cesium bromide (CsBr, 99%) and lead bromide ($PbBr_2$, 98%) were purchased from Tokyo Chemical Industry and Sigma-Aldrich, respectively. The $CsPbBr_3$ powder was synthesized from CsBr and $PbBr_2$ using the solution method described by Stoumpos et al.[23] Dimethyl sulfoxide (DMSO, 99.0%) and *N*, *N*-dimethylformamide (DMF, 99.5%) were purchased from Fujifilm Wako Chemicals. Titanium diisopropoxide bis(acetylacetonate) ($Ti(acac)_2OiPr_2$, 75 wt.% in isopropanol) was purchased from Sigma-Aldrich.

$CsPbBr_3$ Thin Film Deposition

Glass substrates (25 × 25 mm^2) were cleaned by sonication in acetone, methanol, and distilled water for 10 min. $CsPbBr_3$ thin films were prepared on the glass substrates using a mist deposition method. A precursor solution was prepared by dissolving $CsPbBr_3$ powder (0.06 M) in a mixed solvent of DMSO and DMF (1:4, *v*/*v*). The precursor solution was atomized by ultrasonic vibration at 2.4 MHz. As the commercial ultrasonic generator was designed to atomize water, DMF was used to decrease the viscosity of the solvent to 0.95 cP, which is similar to that of water. The generated mist was then transported by nitrogen gas to a nozzle with a rectangular aperture (30 × 1 mm^2), which supplied the mist to the preheated glass substrate (135 °C) as a curtain-like flow. The distance from the nozzle aperture to the substrate surface was 2 mm. The flow rates of the carrier gas and dilution gas were set at 0.375 and 4.625 L min^{-1}, respectively. $CsPbBr_3$ was uniformly deposited over a wide area by passing the substrate under the mist flow at a constant speed of 0.06 mm s^{-1}. After the coating procedure, the obtained $CsPbBr_3$ film was annealed at 350 °C for 30 min on a hotplate.

Fabrication of All-Inorganic Perovskite Solar Cells

Indium tin oxide (ITO)-coated glass (GEOMATEC, 25 × 25 mm^2) was cleaned by sonication in acetone, methanol, and distilled water for 10 min. Firstly, a TiO_2 layer was deposited on the ITO glass using a mist deposition method. A precursor solution for the TiO_2 coating was prepared by mixing methanol with the $Ti(acac)_2OiPr_2$ solution (99:1, *v*/*v*). For TiO_2 deposition, the substrate temperature was set at 400 °C, and the flow rates of the carrier gas and dilution gas were set at 2.0 and 3.0 L min^{-1}, respectively. Using a glass mask, TiO_2 was deposited onto a selected area of the substrate (20 × 25 mm^2), which left a section of the ITO glass exposed as an electrode. Secondly, the $CsPbBr_3$ layer was deposited on the TiO_2 layer using the same method as for deposition on the glass substrate. In this study, $CsPbBr_3$ was deposited onto a selected area of 25 × 15 mm^2 by using a step motor to move the substrate over a distance of 15 mm at a speed of 0.06 mm s^{-1}, unless otherwise noted. The $CsPbBr_3$ layer was coated with carbon ink (JELCON CH-8, Jujo Chemical) using screen printing (mask size: 3 × 3 mm^2) followed by annealing at 200 °C for 30 min. Because the actual electrode area varied, the active device areas were measured to be 0.08–0.10 cm^2.

Measurements and Characterization

The solvent viscosity was measured using a tuning fork vibro viscometer (SV-100, A & D Company). X-ray diffraction (XRD) patterns of the $CsPbBr_3$ films were obtained using a PW 3040/60 X'Pert PRO diffractometer (PANalytical) with Cu-Kα radiation. Optical absorption spectra were measured by UV-vis spectroscopy (UV-2450, Shimadzu). Scanning electron microscopy (SEM) images were taken with a JSM-6510LV instrument (JEOL). The current density–voltage (*J–V*) characteristics of the devices were measured with a source meter (Keithley 2450) at a scan rate of 0.1 V s^{-1} under 1 Sun (AM 1.5 G, 100 mW cm^{-2}) illumination with a solar simulator (HAL-320, Asahi Spectra).

3.3 Results and Discussion

3.3.1 $CsPbBr_3$ Thin Films on Glass Substrates

As shown in Figure 3-2a, a uniform $CsPbBr_3$ film was obtained on the glass substrate. The top-view scanning electron microscopy (SEM) image reveals that the $CsPbBr_3$ film fully covered the substrate surface without any voids (Figure 3-2b), unlike films prepared by the conventional one-step spin-coating method.[18] To investigate the optical properties and crystallinity, the absorbance spectrum and the X-ray diffraction (XRD) pattern were measured. Figure 3-2c shows the absorbance spectrum and the corresponding Tauc plot of the $CsPbBr_3$ film, which confirmed that the absorption edge and optical bandgap (E_g) were 527 nm and 2.35 eV, respectively, and were in agreement with previously reported values for $CsPbBr_3$.[6] As shown in Figure 3-2d, the XRD pattern was well matched to that of the orthorhombic $CsPbBr_3$ phase[23] with the preferred orientation along the (101) plane, which is consistent with the results in Chapter 2. Additionally, no changes were observed in the XRD pattern after storage for over 1 month under atmospheric conditions (0–25 °C, average RH 60%). The fact that peaks derived from an impurity phase, such as Cs_4PbBr_6 or $CsPb_2Br_5$, were not detected, shows that a high-purity $CsPbBr_3$ film was produced by the mist deposition method. In terms of chemical equilibrium theory, the Cs-rich impurity phase tends to precipitate from the solution in which Cs and Pb are dissolved in equal molar ratios.[19] However, in the case of the mist deposition method, $CsPbBr_3$, which has the same composition ratio as that of the solution, tends to precipitate because the solute is precipitated by the fast evaporation of mist particles. These results demonstrated that full-coverage $CsPbBr_3$ thin films can be obtained from a one-step solution without any additives by using the mist deposition method. Generally, voids in the photoconductive layer cause voltage loss owing to the formation of short-circuit.[24] Therefore, it is expected that the void-free $CsPbBr_3$ film could realize a high V_{OC}.

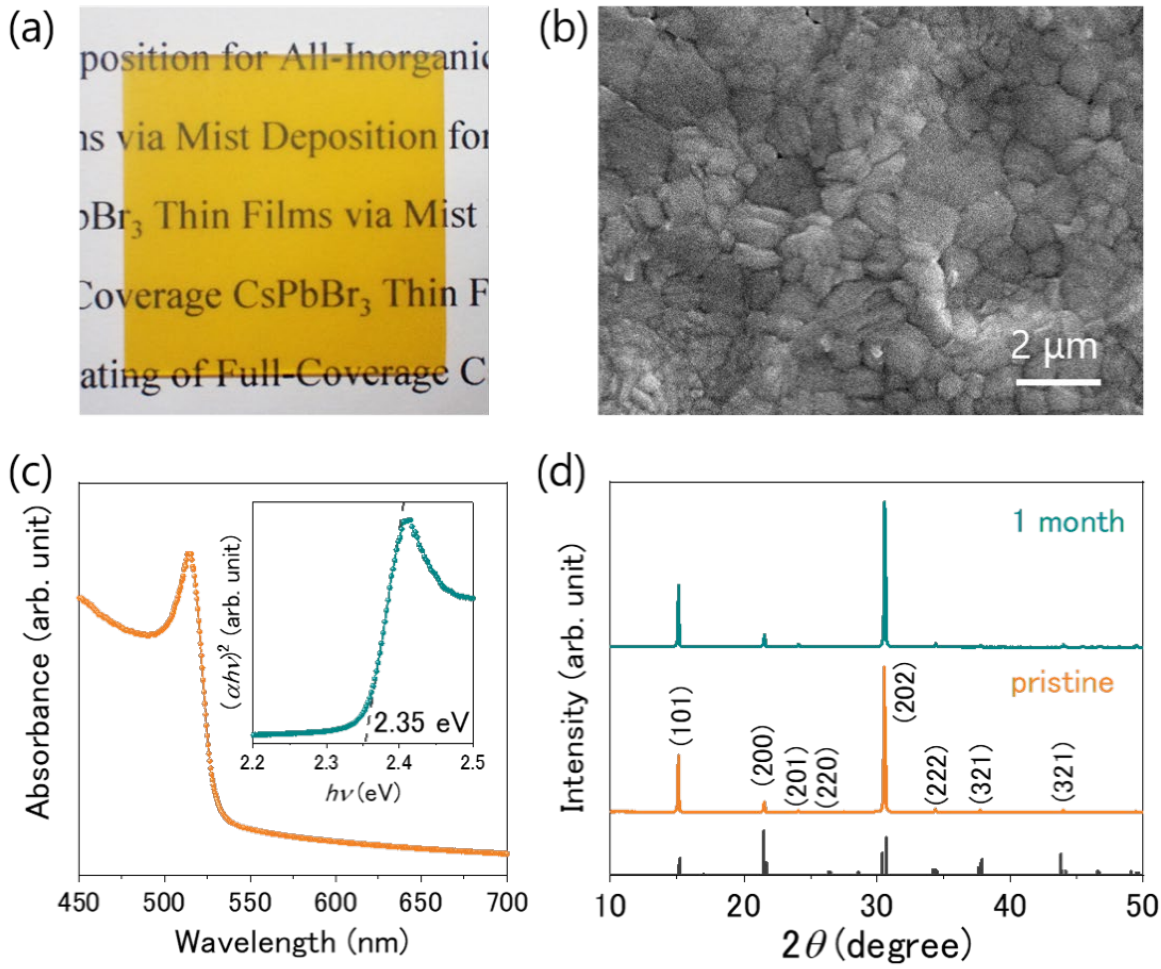

Figure 3-2| (a) Photograph (25 × 25 mm^2), (b) top-view SEM image, (c) absorbance spectrum (inset: Tauc plot) and (d) XRD patterns of the pristine $CsPbBr_3$ film and aged $CsPbBr_3$ film.

3.3.2 Photovoltaic Performances of All-Inorganic Perovskite Solar Cells

To evaluate the photovoltaic performances of the $CsPbBr_3$ thin films, $CsPbBr_3$ PSCs with the ITO/TiO_2/$CsPbBr_3$/carbon configuration were prepared. For photovoltaic application, not only the surface coverage ratio is important, but also the thickness of the photoconductive layer. Therefore, the thickness of the $CsPbBr_3$ film required to cover the substrate completely was investigated and the photovoltaic performances at various $CsPbBr_3$ thicknesses were evaluated. The $CsPbBr_3$ thickness was controlled by the stage speed (v) which is directly related to the number of mist particles arriving at the substrate. Regardless of the stage speed, all detected XRD peaks were identified by $CsPbBr_3$ and the TiO_2/ITO substrate (Figure 3-3).

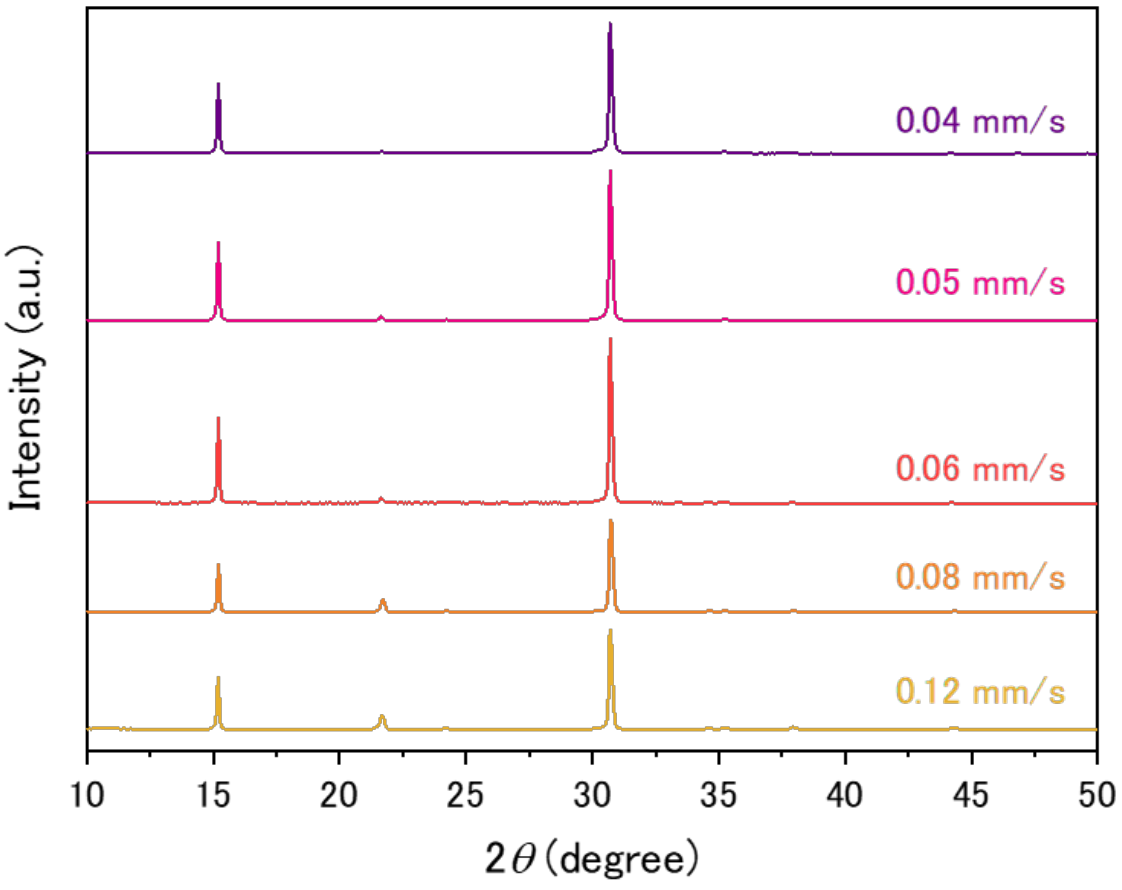

Figure 3-3| XRD patterns of $CsPbBr_3$ films prepared on TiO_2/ITO substrates by various stage speeds.

Figure 3-4 shows surface and cross-sectional SEM images of $CsPbBr_3$ PSCs. The film thickness and the grain size distribution (Figure 3-5) were measured from these SEM images. In the case of a too fast stage speed (v = 0.12 mm s^{-1} or above), the $CsPbBr_3$ layer only partially covered the substrate, which was attributed to an insufficient amount of mist particles. By comparison, full-coverage was achieved at a moderate stage speed (v = 0.04–0.08 mm s^{-1}) and the thickness was measured to be 340–920 nm. As shown in Figure 3-6, the thickness and the mean grain size of the $CsPbBr_3$ layers increased in proportion to supply time, defined as the reciprocal of the stage speed. Additionally, the mean grain size was always more than twice the thickness. For the 580 nm thick $CsPbBr_3$ layer, the average grain size was 1.4 μm. Consequently, the $CsPbBr_3$ layer had a monolayer-vertical structure, which consisted of single grains arranged in a vertical direction, as shown in Figure 3-4c. This monolayer-vertical structure was also observed in the other full-coverage $CsPbBr_3$ layers.

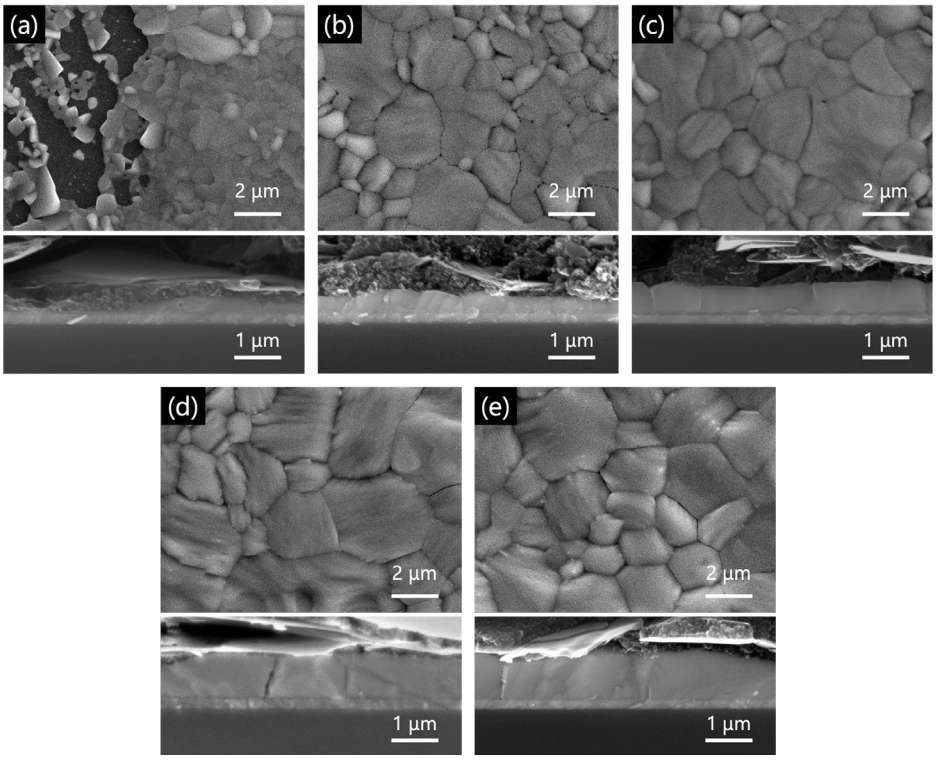

Figure 3-4| Top-view and cross-sectional SEM images of carbon-based $CsPbBr_3$ PSCs in which the $CsPbBr_3$ layer was fabricated at different stage speeds: (a) 0.12, (b) 0.08, (c) 0.06, (d) 0.05, and (e) 0.04 mm s^{-1}.

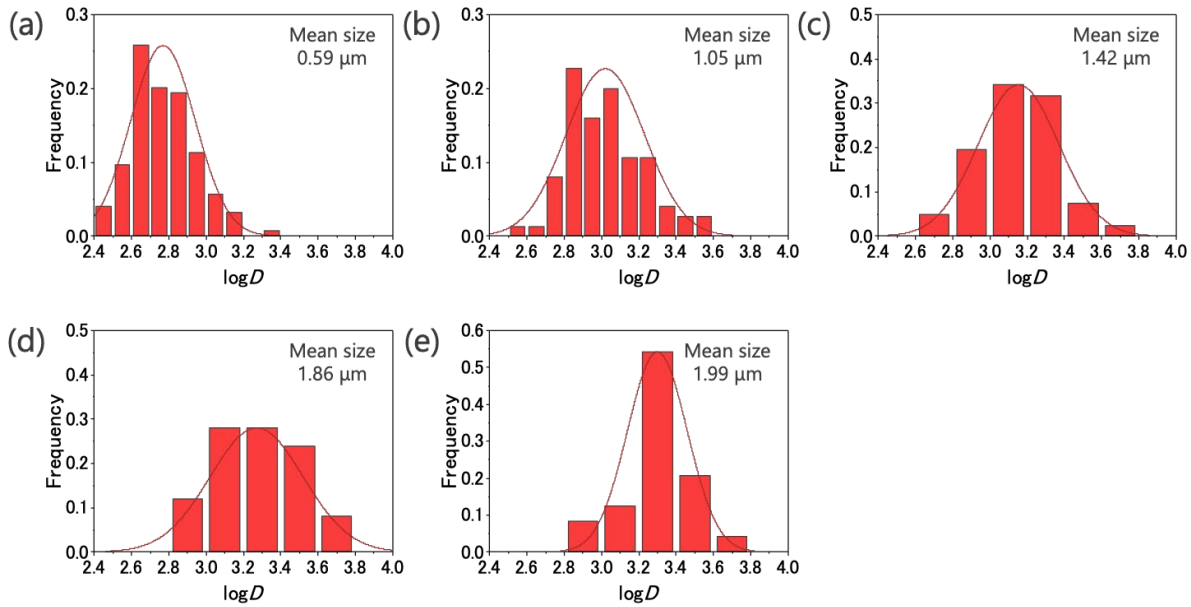

Figure 3-5| Grain size (D (nm)) distribution of $CsPbBr_3$ layers fabricated at different stage speeds: (a) 0.12, (b) 0.08, (c) 0.06, (d) 0.05, and (e) 0.04 mm s^{-1}.

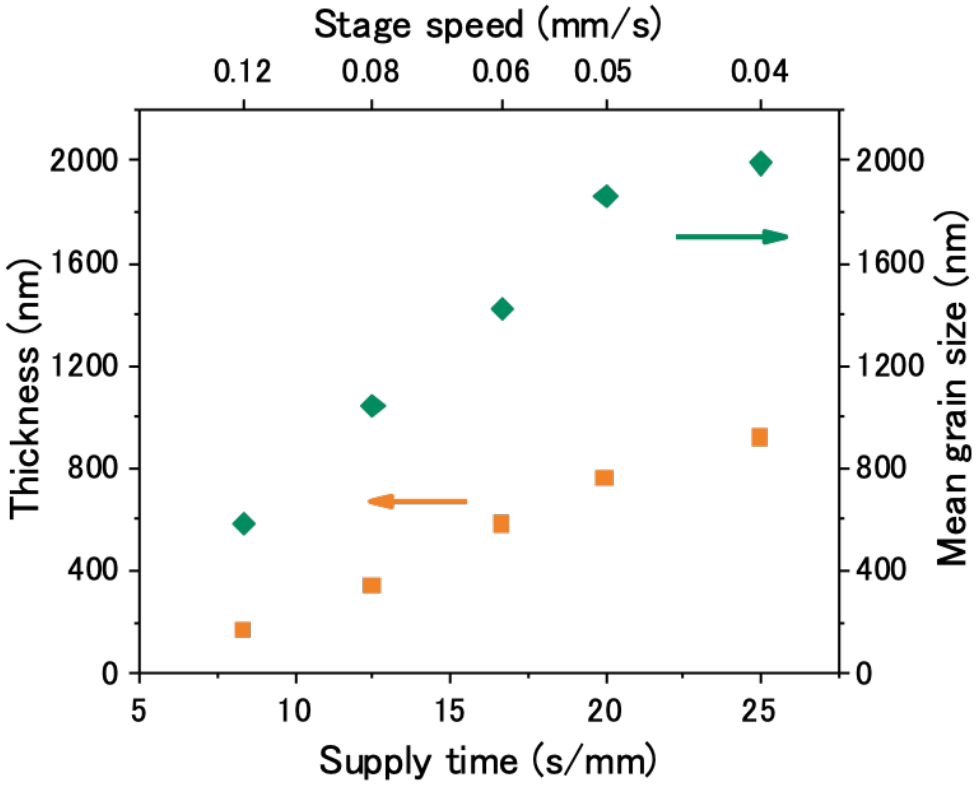

Figure 3-6| Correlation between supply time, film thickness, and mean grain size.

Figure 3-7 shows the photovoltaic performance, including the short-circuit current density (J_{SC}), V_{OC}, fill factor (FF), and PCE, of the $CsPbBr_3$ PSCs. It should be noted that full-coverage films were obtained when the thickness of the $CsPbBr_3$ layer was more than 340 nm (the area shown in yellow in Figure 3-7). In the case of the poor coverage $CsPbBr_3$ layer, the average PCE was limited to 4.5%. By comparison, that of the full-coverage $CsPbBr_3$ layer drastically improved to 7.0–7.8%, which was attributed to especially the improved FF from 0.63 to 0.73–0.75 owing to the elimination of short-circuit. For the full-coverage layers, a high V_{OC} of up to 1.51 V was obtained and the value is higher than those of the carbon-based PSCs in previous studies (Table 3-1). This fact suggests that the voltage loss was effectively eliminated by achieving full-coverage. Interestingly, the average PCEs at thicknesses of 580–920 nm distributed in a small range (7.6–7.8%). Considering that the increased photon absorption was negligible in this range (Figure 3-8), the similar PCEs implied that the obtained $CsPbBr_3$ layers with monolayer-vertical structures have long carrier diffusion lengths. In Chapter 2, thick $CsPbBr_3$ films prepared by the mist deposition method demonstrated a high carrier mobility (13 $cm^2\ V^{-1}\ s^{-1}$) and a low trap density ($1.3 \times 10^{12}\ cm^{-3}$), which are comparable to those for single crystals.[25] For $CsPbBr_3$ single crystals, the diffusion lengths for electrons and holes have been reported to be 10.9 and 9.5 μm, respectively,[26] and therefore this speculation seems reasonable. It should be noted that there was no significant degradation of ITO performance including conductivity and transmittance because the annealing time was short in this study.

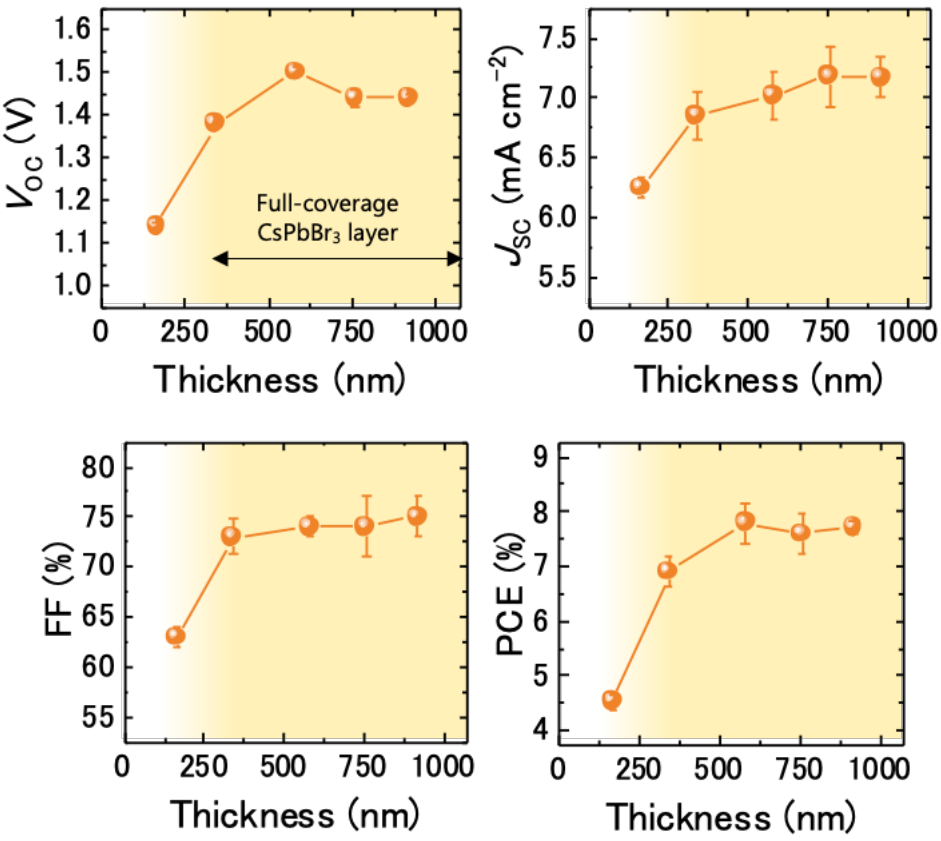

Figure 3-7| Photovoltaic performance, including J_{SC}, V_{OC}, FF, and PCE, of the $CsPbBr_3$ PSCs with $CsPbBr_3$ layers of various thicknesses.

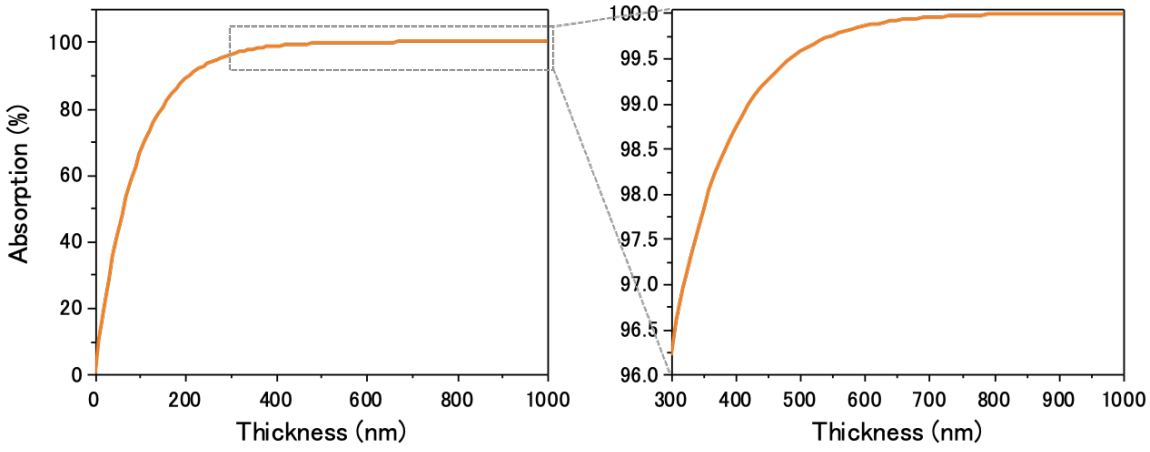

Figure 3-8| Calculated absorption of the $CsPbBr_3$ film at a wavelength of 500 nm vs. thickness. The absorption is almost same when the thickness is >300 nm.

3.3.3 Stability and Reproducibility of All-Inorganic Perovskite Solar Cells

Figure 3-9a shows the current density–voltage (*J–V*) curve of a typical 580 nm $CsPbBr_3$-based PSC, for which the corresponding photovoltaic parameters were a PCE of 8.3%, a J_{SC} of 7.3 mA cm^{-2}, a V_{OC} of 1.51 V, and a FF of 0.75. To evaluate the validity of the photovoltaic performance of our devices, the stabilized current density and PCE were measured at a bias voltage of 1.27 V. As shown in Figure 3-9b, the current density and PCE gradually increased and stabilized at 6.1 mA cm^{-2} and 7.7%, respectively. The stabilized PCE of 7.7% is the highest reported value for carbon-based $CsPbBr_3$ PSCs prepared via a one-step solution process. The full surface coverage and large grain size of the $CsPbBr_3$ layer seem to contribute to this excellent performance. In comparison to state-of-the-art $CsPbBr_3$ PSCs prepared via two-step solution processes (Table 3-1), the stabilized PCE of 7.7% is still low but comparable to control devices without any interface engineering. Considering that our devices suffered from hysteresis (Figure 3-10), which is related to the defects and trap states at the perovskite/adjacent layer interface,[27] it is expected that interface engineering can eliminate hysteresis and further improve the PCE.[7–12]

To evaluate the reproducibility of the mist deposition method for $CsPbBr_3$ PSCs, we fabricated 18 cells and measured their PCEs. As shown by the histogram in Figure 3-11, the PCEs were distributed over a small range with an average value of 7.7% and a standard deviation of 0.6%, suggesting high reproducibility.

The $CsPbBr_3$ PSC can maintain 84% of its initial PCE values under continuous light illumination over 10000 s (Figure 3-12a). Additionally, even after more than two months of storage in atmospheric conditions (0–25 °C, average RH 60%) without any encapsulation, there was no degradation of photovoltaic performance (Figure 3-12b).

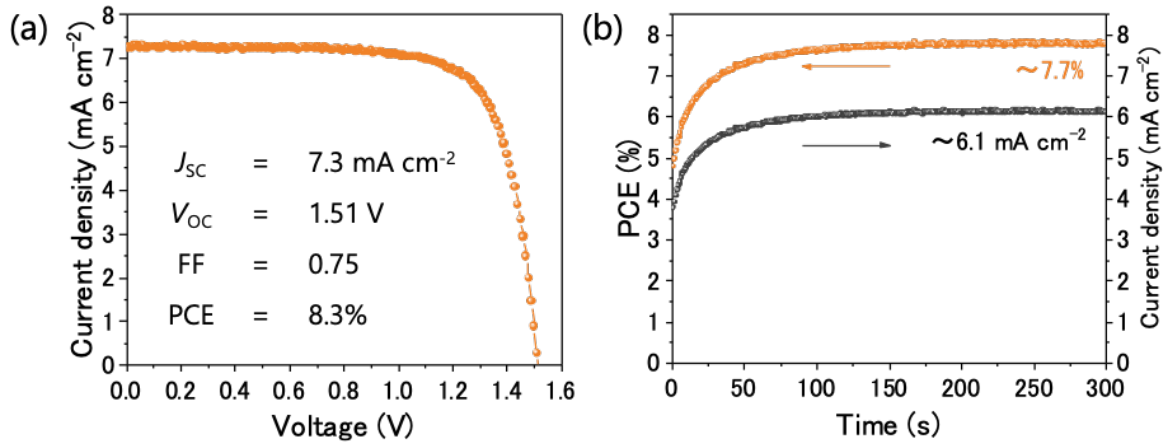

Figure 3-9| (a) *J*–*V* curve of a typical $CsPbBr_3$ PSC. (b) Stabilized PCE and current density at a bias voltage of 1.27 V.

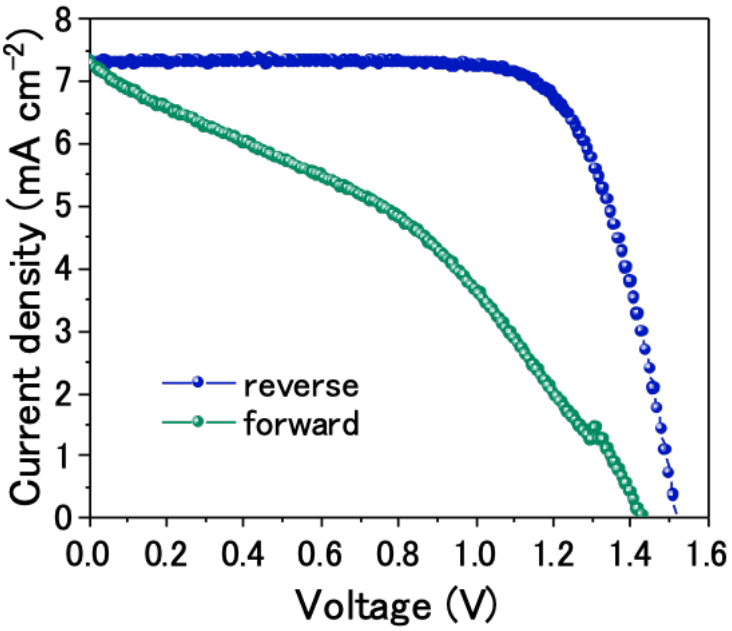

Figure 3-10| *J*–*V* curve of a carbon-based $CsPbBr_3$ PSC under reverse and forward scanning conditions.

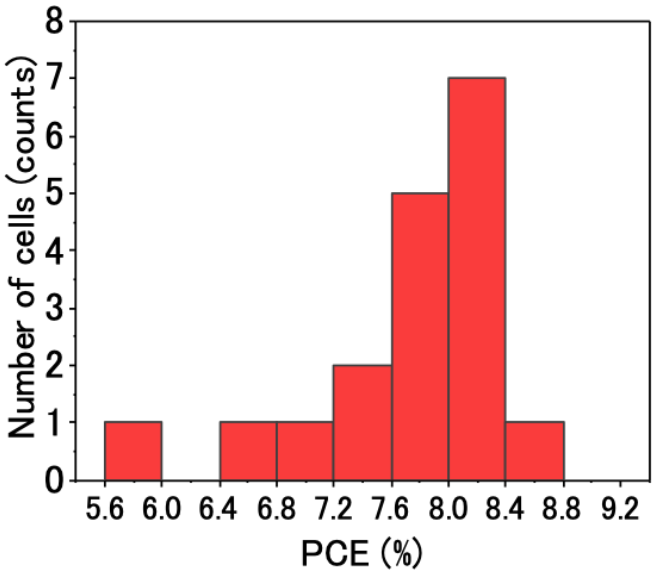

Figure 3-11| Histogram of the PCEs of 18 $CsPbBr_3$ PSCs.

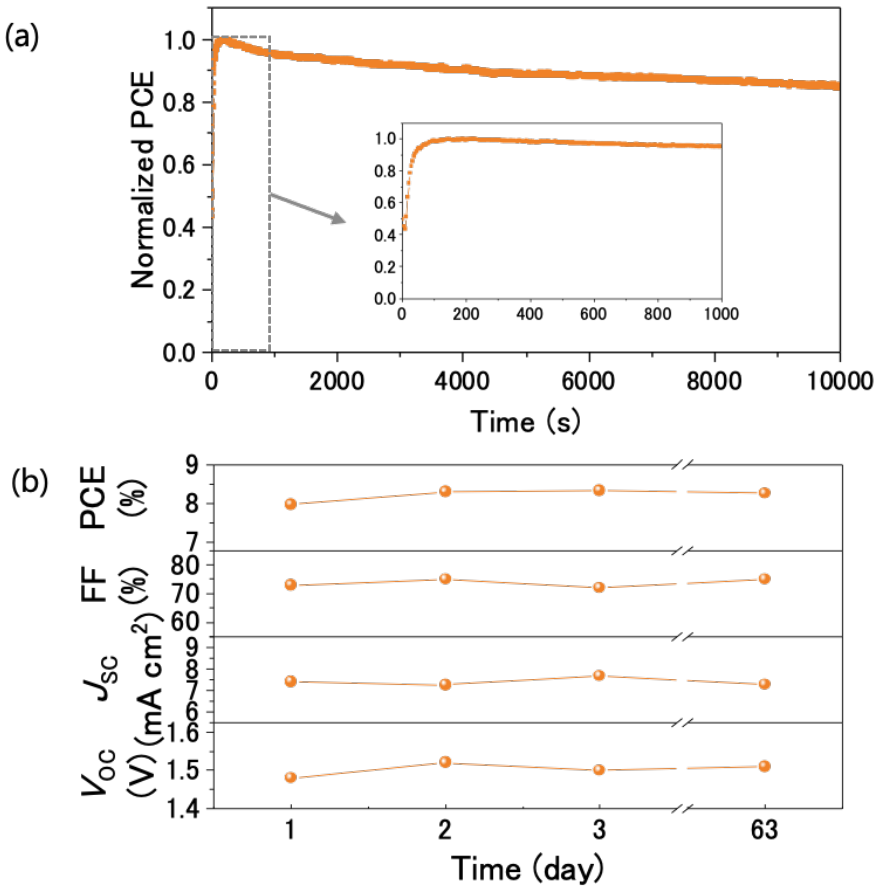

Figure 3-12| (a) Photostability and (b) storage stability of $CsPbBr_3$ PSCs without any encapsulation

Table 3-1| Photovoltaic performance of representative carbon-based $CsPbBr_3$ PSCs.

Device Structure	Method	PCE (%)	S-PCE [a] (%)	J_{SC} (mA cm^{-2})	V_{OC} (V)	FF	Ref
FTO/c-TiO_2/mp-TiO_2/$CsPbBr_3$/carbon	2-step	6.7	-	7.4	1.24	0.73	[6]
FTO/c-TiO_2/mp-TiO_2/$CsPbBr_3$/carbon	2-step	7.54	7.06 [b]	7.46	1.308	0.773	[7]
FTO/c-TiO_2/mp-TiO_2/GQDs/$CsPbBr_3$/carbon		9.72	9.62 [b]	8.12	1.458	0.821	
FTO/c-TiO_2/mp-TiO_2/$CsPbBr_3$/carbon	2-step	3.8	-	4.5	1.23	0.69	[8]
FTO/c-TiO_2/mp-TiO_2/$CsPbBr_3$/CuPc/carbon		6.21	-	6.62	1.26	0.744	
FTO/c-TiO_2/mp-TiO_2/$CsPbBr_3$/carbon	2-step	7.76	7.8 [c]	6.86	1.438	0.786	[28]
FTO/c-TiO_2/mp-TiO_2/GQDs/$CsPbBr_3$/ClSZ-QDs/carbon		9.43	9.3 [c]	7.35	1.522	0.843	
FTO/c-TiO_2/mp-TiO_2/$CsPbBr_3$/carbon	2-step	6.01	6.00 [b]	6.13	1.34	0.7316	[9]
FTO/c-TiO_2/mp-TiO_2/$CsPbBr_3$/$CuInS_2$/ZnS-QDs/carbon		8.42	8.40 [b]	7.47	1.45	0.773	
FTO/c-TiO_2/mp-TiO_2/$CsPbBr_3$/carbon	2-step	7.28	7.1 [c]	6.72	1.406	0.771	[13]
FTO/c-TiO_2/mp-TiO_2/$Cs_{0.91}Rb_{0.09}PbBr_3$/carbon		9.86	9.6 [c]	7.73	1.552	0.822	
FTO/c-TiO_2/mp-TiO_2/$CsPbBr_3$/NiO_x/carbon	2-step	7.29	-	6.84	1.4	0.761	[14]
FTO/c-TiO_2/mp-TiO_2/$CsPb_{0.97}Tb_{0.03}Br_3$/SnS:ZnS/NiO_x/carbon		10.26	10.18 [b]	8.21	1.57	0.796	
FTO/c-TiO_2/mp-TiO_2/$CsPbBr_3$/carbon	2-step	6.37	6.2 [c]	6.04	1.431	0.737	[15]
FTO/c-TiO_2/mp-TiO_2/$CsPb_{0.995}Zn_{0.005}Br_3$/carbon		9.18	9.2 [c]	7.3	1.56	0.8061	
FTO/Ni-TiO_2/$CsPbBr_3$/CuPc/carbon	2-step	6.94	6.16 [b]	7.36	1.292	0.730	[29]
FTO/Ni-TiO_2/$CsPbBr_3$/CuPc/carbon (CB treated)		8.55	7.95 [b]	7.92	1.362	0.793	
FTO/c-TiO_2/mp-TiO_2/$CsPbBr_3$/carbon	2-step	6.85	6.4 [c]	7.27	1.29	0.7304	[30]
FTO/c-TiO_2/mp-TiO_2/Sn-$CsPbBr_3$/carbon		8.63	8.6 [c]	7.66	1.37	0.8222	
FTO/c-TiO_2/mp-TiO_2/$CsPbBr_3$/carbon	2-step	7.39	7.21 [b]	6.75	1.41	0.776	[10]
FTO/c-TiO_2/mp-TiO_2/Sm^{3+}-$CsPbBr_3$/Cu(Cr,Ni)O_2/carbon		10.79	10.08 [b]	7.81	1.615	0.855	
FTO/SnO_2/$CsPbBr_3$/carbon	2-step	10.2	10.3 [c]	7.64	1.588	0.841	[31]
FTO/SnO_2/$CsPbBr_3$/N-CQDs/carbon		10.71	10.7 [c]	7.87	1.622	0.801	
FTO/c-TiO_2/mp-TiO_2/$CsPbBr_3$/carbon	2-step	6.15	5.6 [c]	5.15	1.51	0.77	[32]
FTO/c-TiO_2/mp-TiO_2/$CsPbBr_3$/[BMMIm]Cl/carbon		9.92	9.48 [b]	7.45	1.61	0.83	
FTO/c-TiO_2/mp-TiO_2/$CsPbBr_3$/carbon	2-step	7.38	7.4 [c]	7.03	1.426	0.736	[11]
FTO/c-TiO_2/mp-TiO_2/$CsPbBr_3$/C12-QDs/LPP-carbon		10.85	-	7.73	1.626	0.863	
FTO/SnO_2-TiO_xCl_{4-2x}/$CsPbBr_3$/carbon	2-step	9.27	9.3 [c]	7.45	1.59	0.783	[12]
FTO/SnO_2-TiO_xCl_{4-2x}/WS_2/$CsPbBr_3$/carbon		10.65	10.6 [c]	7.95	1.70	0.790	
FTO/c-SnO_2/$CsPbBr_3$/carbon	1-step	4.36	-	6.13	1.15	0.62	[18]
FTO/c-SnO_2/$CsPbBr_3$-PEG/carbon		7.8	7.2 [b]	7.56	1.41	0.73	
ITO/c-TiO_2/$CsPbBr_3$/carbon	**1-step**	**8.3**	**7.7**	**7.3**	**1.51**	**0.75**	**This work**

[a] S-PCE; stabilized power conversion efficiency, [b] Value read from the text, [c] Value read from a graph

3.4 Conclusions

In summary, the author demonstrated the fabrication of a one-step solution-processed $CsPbBr_3$ PSCs using a mist deposition method. $CsPbBr_3$ films with full surface coverage and a large grain size were obtained at thicknesses of more than 340 nm, whereas thinner $CsPbBr_3$ films suffered from poor coverage. The 580 nm $CsPbBr_3$-based device achieved an excellent photovoltaic performance, including a PCE of 8.3%, a J_{SC} of 7.3 mA cm^{-2}, a V_{OC} of 1.51 V, and a FF of 0.75. Moreover, the stabilized PCE of 7.7% is the highest value for a $CsPbBr_3$-based PSC fabricated via a one-step solution process and is comparable to those for PSCs fabricated via two-step solution processes. Notably, the PCE of the $CsPbBr_3$ PSC decreased by only 0.1% on increasing the thickness of the $CsPbBr_3$ layer from 580 to 920 nm, suggesting that the $CsPbBr_3$ layers had a long carrier diffusion length.

References for Chapter 3

1. Kulbak, M., Cahen, D. & Hodes, G. How Important Is the Organic Part of Lead Halide Perovskite Photovoltaic Cells? Efficient $CsPbBr_3$ Cells. *The Journal of Physical Chemistry Letters* **6**, 2452–2456 (2015).

2. Kulbak, M. *et al.* Cesium Enhances Long-Term Stability of Lead Bromide Perovskite-Based Solar Cells. *The Journal of Physical Chemistry Letters* **7**, 167–172 (2016).

3. Ku, Z., Rong, Y., Xu, M., Liu, T. & Han, H. Full Printable Processed Mesoscopic $CH_3NH_3PbI_3/TiO_2$ Heterojunction Solar Cells with Carbon Counter Electrode. *Scientific Reports* **3**, 3132 (2013).

4. Mei, A. *et al.* A hole-conductor-free, fully printable mesoscopic perovskite solar cell with high stability. *Science* **345**, 295–298 (2014).

5. Hu, Y. *et al.* Stable Large-Area (10 × 10 cm^2) Printable Mesoscopic Perovskite Module Exceeding 10% Efficiency. *Solar RRL* **1**, 2–7 (2017).

6. Liang, J. *et al.* All-Inorganic Perovskite Solar Cells. *Journal of the American Chemical Society* **138**, 15829–15832 (2016).

7. Duan, J., Zhao, Y., He, B. & Tang, Q. High-Purity Inorganic Perovskite Films for Solar Cells with 9.72 % Efficiency. *Angewandte Chemie International Edition* **57**, 3787–3791 (2018).

8. Liu, Z. *et al.* Efficient Carbon-Based $CsPbBr_3$ Inorganic Perovskite Solar Cells by Using Cu-Phthalocyanine as Hole Transport Material. *Nano-Micro Letters* **10**, 34 (2018).

9. Ding, J., Duan, J., Guo, C. & Tang, Q. Toward charge extraction in all-inorganic perovskite solar cells by interfacial engineering. *Journal of Materials Chemistry A* **6**, 21999–22004 (2018).

10. Duan, J., Zhao, Y., Wang, Y., Yang, X. & Tang, Q. Hole-Boosted $Cu(Cr,M)O_2$ Nanocrystals for All-Inorganic $CsPbBr_3$ Perovskite Solar Cells. *Angewandte Chemie International Edition* **58**, 16147–16151 (2019).

11. Duan, J., Wang, Y., Yang, X. & Tang, Q. Alkyl-Chain-Regulated Charge Transfer in Fluorescent Inorganic $CsPbBr_3$ Perovskite Solar Cells. *Angewandte Chemie International Edition* **59**, 4391–4395 (2020).

12. Zhou, Q., Duan, J., Yang, X., Duan, Y. & Tang, Q. Interfacial Strain Release from the $WS_2/CsPbBr_3$ van der Waals Heterostructure for 1.7 V Voltage All-Inorganic Perovskite Solar Cells. *Angewandte Chemie* **132**, 22181–22185 (2020).

13. Li, Y. *et al.* Lattice Modulation of Alkali Metal Cations Doped $Cs_{1-x}R_xPbBr_3$ Halides for Inorganic Perovskite Solar Cells. *Solar RRL* **2**, 1800164 (2018).

14. Yuan, H. *et al.* All-inorganic $CsPbBr_3$ perovskite solar cell with 10.26% efficiency by spectra engineering. *Journal of Materials Chemistry A* **6**, 24324–24329 (2018).

15. Tang, M. *et al.* Toward efficient and air-stable carbon-based all-inorganic perovskite solar cells through substituting $CsPbBr_3$ films with transition metal ions. *Chemical Engineering Journal* **375**, 121930 (2019).

16. Wang, Z. *et al.* Efficient and Stable Pure Green All-Inorganic Perovskite $CsPbBr_3$ Light-Emitting Diodes with a Solution-Processed NiOx Interlayer. *The Journal of Physical Chemistry C* **121**, 28132–28138 (2017).

17. Song, L. *et al.* Efficient Inorganic Perovskite Light-Emitting Diodes with Polyethylene Glycol Passivated Ultrathin $CsPbBr_3$ Films. *Journal of Physical Chemistry Letters* **8**, 4148–4154 (2017).

18. Ren, Y. *et al.* Exploration of polymer-assisted crystallization kinetics in $CsPbBr_3$ all-inorganic solar cell. *Chemical Engineering Journal* **392**, 123805 (2020).

19. Dirin, D. N., Cherniukh, I., Yakunin, S., Shynkarenko, Y. & Kovalenko, M. V. Solution-Grown $CsPbBr_3$ Perovskite Single Crystals for Photon Detection. *Chemistry of Materials* **28**, 8470–8474 (2016).

20. Park, M. *et al.* Highly Reproducible Large-Area Perovskite Solar Cell Fabrication via Continuous Megasonic Spray Coating of $CH_3NH_3PbI_3$. *Small* **15**, 1804005 (2019).

21. Chen, H. *et al.* Comprehensive studies of air-brush spray deposition used in fabricating high-efficiency $CH_3NH_3PbI_3$ perovskite solar cells: Combining theories with practices. *Journal of Power Sources* **402**, 82–90 (2018).

22. Heo, J. H., Lee, M. H., Jang, M. H. & Im, S. H. Highly efficient $CH_3NH_3PbI_{3-x}Cl_x$ mixed halide perovskite solar cells prepared by re-dissolution and crystal grain growth via spray coating. *Journal of Materials Chemistry A* **4**, 17636–17642 (2016).

23. Stoumpos, C. C. *et al.* Crystal Growth of the Perovskite Semiconductor $CsPbBr_3$: A New Material for High-Energy Radiation Detection. *Crystal Growth & Design* **13**, 2722–2727 (2013).

24. Fu, K. *et al.* Influence of void-free perovskite capping layer on the charge recombination process in high performance $CH_3NH_3PbI_3$ perovskite solar cells. *Nanoscale* **8**, 4181–4193 (2016).

25. Haruta, Y., Ikenoue, T., Miyake, M. & Hirato, T. Fabrication of (101)-oriented $CsPbBr_3$

thick films with high carrier mobility using a mist deposition method. *Applied Physics Express* **12**, 085505 (2019).

26. Song, J. *et al.* Ultralarge All-Inorganic Perovskite Bulk Single Crystal for High-Performance Visible-Infrared Dual-Modal Photodetectors. *Advanced Optical Materials* **5**, 1700157 (2017).

27. Chen, B., Yang, M., Priya, S. & Zhu, K. Origin of J – V Hysteresis in Perovskite Solar Cells. *The Journal of Physical Chemistry Letters* **7**, 905–917 (2016).

28. Duan, J., Hu, T., Zhao, Y., He, B. & Tang, Q. Carbon-Electrode-Tailored All-Inorganic Perovskite Solar Cells To Harvest Solar and Water-Vapor Energy. *Angewandte Chemie International Edition* **57**, 5746–5749 (2018).

29. Liu, X. *et al.* Novel antisolvent-washing strategy for highly efficient carbon-based planar $CsPbBr_3$ perovskite solar cells. *Journal of Power Sources* **439**, 227092 (2019).

30. Guo, H. *et al.* Doping with $SnBr_2$ in $CsPbBr_3$ to enhance the efficiency of all-inorganic perovskite solar cells. *Journal of Materials Chemistry C* **7**, 11234–11243 (2019).

31. Zhao, Y., Duan, J., Wang, Y., Yang, X. & Tang, Q. Precise stress control of inorganic perovskite films for carbon-based solar cells with an ultrahigh voltage of 1.622 V. *Nano Energy* **67**, 104286 (2020).

32. Zhang, W. *et al.* Interface Engineering of Imidazolium Ionic Liquids toward Efficient and Stable $CsPbBr_3$ Perovskite Solar Cells. *ACS Applied Materials & Interfaces* **12**, 4540–4548 (2020).

Chapter 4
$CsPbBr_3$-Based X-Ray Detectors

4.1 Introduction

As shown in Chapter 1, metal halide perovskite materials demonstrated excellent X-ray detection performance. The parameters of several X-ray detectors based on perovskite materials, as proposed in the existing studies, are summarized in Table 4-1. For example, Wei et al. reported on Si-integrated $CH_3NH_3PbBr_3$ single crystal X-ray detectors having a sensitivity of 21,000 μC Gy_{air}^{-1} cm^{-2}, which is more than a thousand times higher than that of amorphous selenium (a-Se) detectors.[1] Kim et al. successfully obtained a hand phantom X-ray image by using $CH_3NH_3PbI_3$ thick-film-based flat panel detectors with a sensitivity of 11,000 μC Gy_{air}^{-1} cm^{-2}.[2] However, such detectors suffer from poor thermal stability, which is caused by the volatility of the organic cations.[3] In contrast, all-inorganic perovskite materials, especially cesium lead tribromide ($CsPbBr_3$), demonstrate excellent thermal stability, and thus, these materials are often used to fabricate stable perovskite-based devices including X-ray detectors.[4,5] Gou et al. reported upon an Au/$CsPbBr_3$ (18 μm)/ITO structure self-powered X-ray detector, which could exhibit a sensitivity of 470 μC Gy_{air}^{-1} cm^{-2} at zero bias. The researchers fabricated the $CsPbBr_3$ thick films by using the multiple-times dissolution–recrystallization method.[6] Pan et al. developed a hot-pressed $CsPbBr_3$ quasi-monocrystalline thick film (240 μm), which could achieve a record sensitivity of 55,684 μC Gy_{air}^{-1} cm^{-2}, surpassing that of all the existing X-ray detectors.[7]

Because of the excellent performance demonstrated by $CsPbBr_3$ X-ray detectors, these devices can be considered to be applied for highly sensitive X-ray imaging, which can enable medical diagnosis at a low dose rate, thereby reducing the risk of cancer by radiation. However, the existing fabrication methods for the $CsPbBr_3$ X-ray detectors are not suitable for large-area production. For X-ray imaging devices, a large detection area equivalent to the imaging area is

essential because, in contrast to visible light, it is difficult to condense an X-ray by using a lens. Therefore, a scalable method is required for the fabrication of thick $CsPbBr_3$ films.

In Chapter 2, the authors demonstrated the fabrication of (101)-oriented $CsPbBr_3$ films with a thickness of up to 28 μm by using a mist deposition method, which is suitable for large-area production. Although considerably thicker films (with a thickness of over 100 μm) are preferable for highly sensitive X-ray detection, it is difficult to prepare such thick films owing to the occurrence of film exfoliation during the cooling process after the deposition. In this chapter, the author demonstrated thick films fabrication for X-ray detection applications.

Table 4-1| Comparison of the relevant device parameters of X-ray detectors based on perovskite materials.

Material	Thickness (μm)	X-ray (kV)	Electric Field ($V\ mm^{-1}$)	Sensitivity ($\mu C\ Gy_{air}^{-1}\ cm^{-2}$)	Ref.
$CH_3NH_3PbI_3$ film	0.6	N/A	0	25	8
$CH_3NH_3PbBr_3$ single crystal	2,000	N/A	0.05	80	9
$CH_3NH_3PbBr_3$ single crystal	2,000	8	47	21,000	1
$CH_3NH_3PbI_3$ thick film	830	100	60	11,000	2
$(CsFAMA)PbI_3$ film	0.45	35	890	98	10
$CsPbBr_3$ thick film	18	35	110	1,700	6
$CsPbBr_3$ thick film	240	30	5.0	55,684	7
$CsPbBr_3$ thick film	110	70	45.5	11,840	This work

4.2 Experimentals

Materials

Cesium bromide (CsBr, 99%) and lead bromide ($PbBr_2$, 98%) were purchased from Tokyo Chemical Industry and Sigma-Aldrich, respectively. Dimethyl sulfoxide (DMSO, 99.0%) and *N*, *N*-dimethylformamide (DMF, 99.5%) were purchased from Fujifilm Wako Chemicals. The $CsPbBr_3$ powder was synthesized from CsBr and $PbBr_2$ by using the solution method described by C. C. Stoumpos.[4]

Preparation of $CsPbBr_3$ Thick Films

Pt-coated ITO substrates (hereafter termed as Pt substrates, sized 26 × 20 mm^2) were cleaned using acetone, isopropanol, and distilled water in an ultrasonic bath for 10 min. Subsequently, the substrates were dried using an air blower. To avoid film exfoliation, the Pt substrates were coated with a polymer by using the spin-coating method. $CsPbBr_3$ thick films were prepared on the Pt substrates with and without the polymer layer. A precursor solution was prepared by dissolving 50 mM $CsPbBr_3$ powder in a solvent mixture of DMSO and DMF (volume ratio 6:4). Next, $CsPbBr_3$ was deposited on the substrates by using the mist deposition method. The carrier and dilution gas flow rates were set as 0.375 and 4.625 L min^{-1}, respectively. The substrate temperature was set as 150 °C, which is considered to be optimized for the fabrication of highly (101)-oriented $CsPbBr_3$ films, as reported in chapter 2. In this chapter, $CsPbBr_3$ was deposited onto a reduced area of 26 × 10 mm^2 by moving the substrate by 10 mm at a speed of 0.80 mm s^{-1}. The deposition cycle was determined to assign a thickness of approximately 100 μm. After the $CsPbBr_3$ deposition, the substrate temperature was slowly decreased to room temperature at a cooling rate of less than 2 °C min^{-1}.

Characterization and Device Fabrication

The surface and cross-sections of the films were observed using the scanning electron microscopy technique (SEM; JSM-6510LV, JEOL). Furthermore, the X-ray diffraction (XRD) spectra of the $CsPbBr_3$ films were recorded using a PW 3040/60 X'Pert PRO with Cu-Kα radiation.

An X-ray detector with the configuration of tungsten (W)/$CsPbBr_3$/polymer/Pt was fabricated. A $CsPbBr_3$ thick film was deposited on a polymer-coated Pt substrate. Subsequently, a W electrode was deposited on the $CsPbBr_3$ film by using ion sputtering coating. The device area of 0.25 cm^2 was determined using a metal mask.

Figure 4-1 shows the schematic of the X-ray detection measurements. The photoresponse characteristics of the X-ray detector were measured using a W target X-ray source. The tube voltage and tube current used in the measurement were 70 kV and 2.0 mA, respectively. The dose rate of the X-ray was 10 $\mu Gy_{air}\ s^{-1}$, as measured using an ionized-chamber-type survey meter. The measurements were performed in a dark room to exclude the effect of other photons, such as those of visible light.

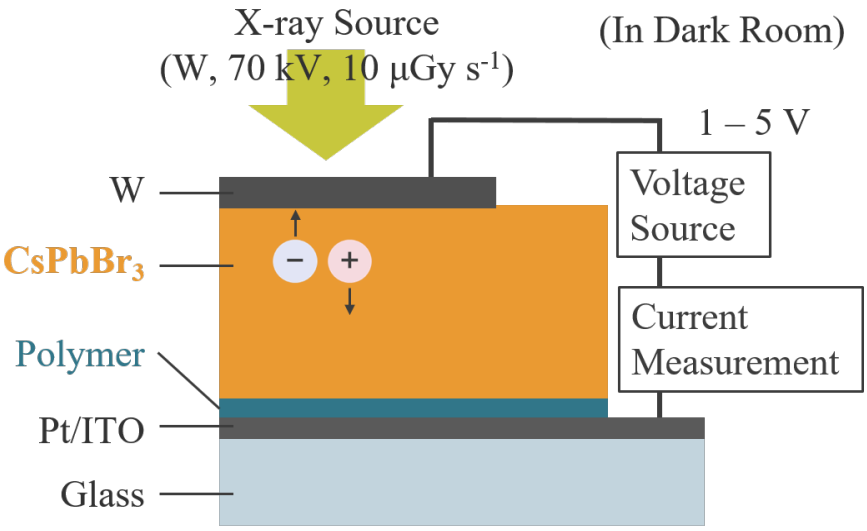

Figure 4-1| Schematic of X-ray detection measurements.

4.3 Results and Discussion

4.3.1 Thick Film Fabrication with Polymer Layer

In chapter 2, the authors successfully formed a 28-μm-thick $CsPbBr_3$ film on a Pt substrate by using the mist deposition method. Since thicker films (with a thickness of more than 100 μm) are preferable for highly sensitive X-ray detection, the deposition cycle was increased to increase the thickness of the $CsPbBr_3$ thick film.

Figure 4-2a shows the images of the obtained film on the Pt substrate. Many light orange speckles appeared on the film surface during the cooling process after the $CsPbBr_3$ deposition. The cross-sectional SEM image of the film (Figure 4-2b, c) revealed that the speckles corresponded to the film exfoliation. It appears that large stress accumulated at the interface between the $CsPbBr_3$ film and Pt substrate owing to the difference in the thermal expansion coefficients. The high thermal expansion coefficient of $CsPbBr_3$ $(1.2 \times 10^{-4}\ K^{-1})^4$ makes it difficult to form a thick film on the Pt substrate without exfoliation. Therefore, a part of the Pt substrate was coated with a polymer as a buffer layer. Figure 4-2d shows the photograph of a $CsPbBr_3$ thick film prepared on the polymer-coated substrate. Unlike the $CsPbBr_3$ film directly prepared on the Pt substrate, a uniform orange film was obtained on the polymer layer, and it did not include any speckles. The SEM images (Figure 4-2) confirmed that as a result of inserting the polymer layer, a uniform 110-μm-thick $CsPbBr_3$ film was successfully obtained without exfoliation. As can be seen in Figure 4-2f, columnar crystals grew even on the polymer layer. Additionally, the XRD patterns indicated that the $CsPbBr_3$ thick film was highly (101)-oriented. The columnar growth and the high (101)-orientation, which correspond to the results in chapter 2, suggest that the $CsPbBr_3$ film has high carrier mobility, which can facilitate the realization of highly sensitive X-ray detection.

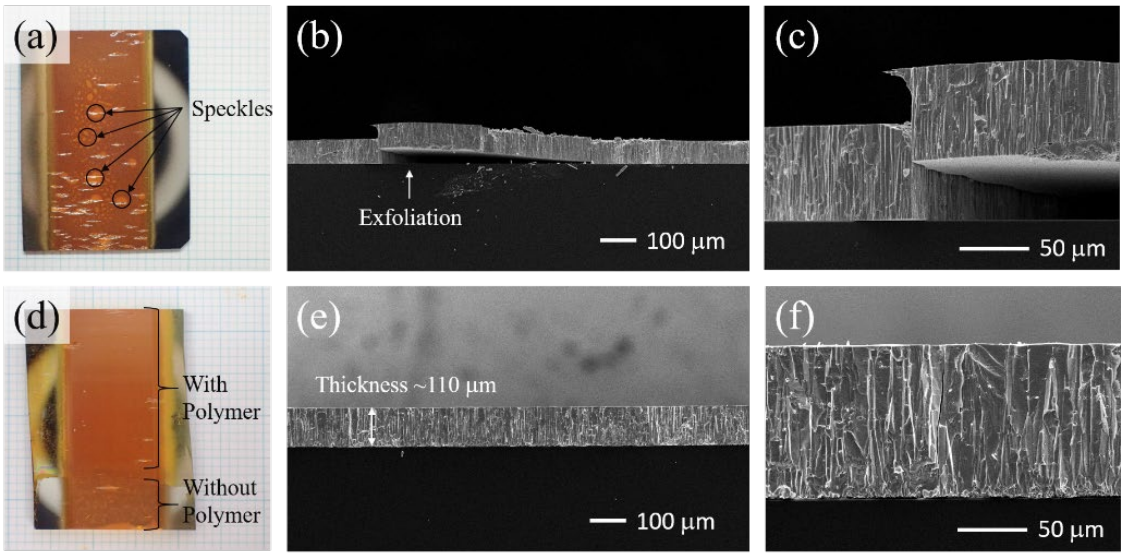

Figure 4-2| (a, d) Photographs and (b, c, e, f) cross-sectional SEM images of $CsPbBr_3$ thick films prepared on (a–c) a bare Pt substrate and (d–f) a polymer-coated Pt substrate.

4.3.2 Fabrication of X-Ray Detectors

An X-ray detector was fabricated by forming a tungsten electrode onto the 110-μm-thick $CsPbBr_3$ film. Figure 4-3a shows the photoresponses to the X-ray with a dose rate of 10 μGy_{air} s^{-1} under bias voltages of 1–5 V. Under all the bias voltages, the measured current was pumped up by the X-ray irradiation, indicating that the X-ray detector could detect the X-ray. The sensitivity (S) of the X-ray detector was calculated using equation: $S = (J_P - J_D)/G$, where J_P, J_D, and G denote the measured photocurrent density, dark current density, and dose rate of 10 μGy_{air} s^{-1}. As shown in Figure 4-3b, the sensitivity increased with an increase in the bias voltage and reached 11,840 μC Gy_{air}^{-1} cm^{-2} under a bias voltage of 5 V (45.5 V mm^{-1}). The sensitivity of the proposed device (11,840 μC Gy_{air}^{-1} cm^{-2}) is considerably higher than that of most other perovskite devices, as presented in Table 4-1. Moreover, this sensitivity is approximately 600 times higher than that of the currently available commercial a-Se X-ray detectors, which operate at a considerably higher field of 10,000 V mm^{-1} (20 μC Gy_{air}^{-1} cm^{-2}).[11]

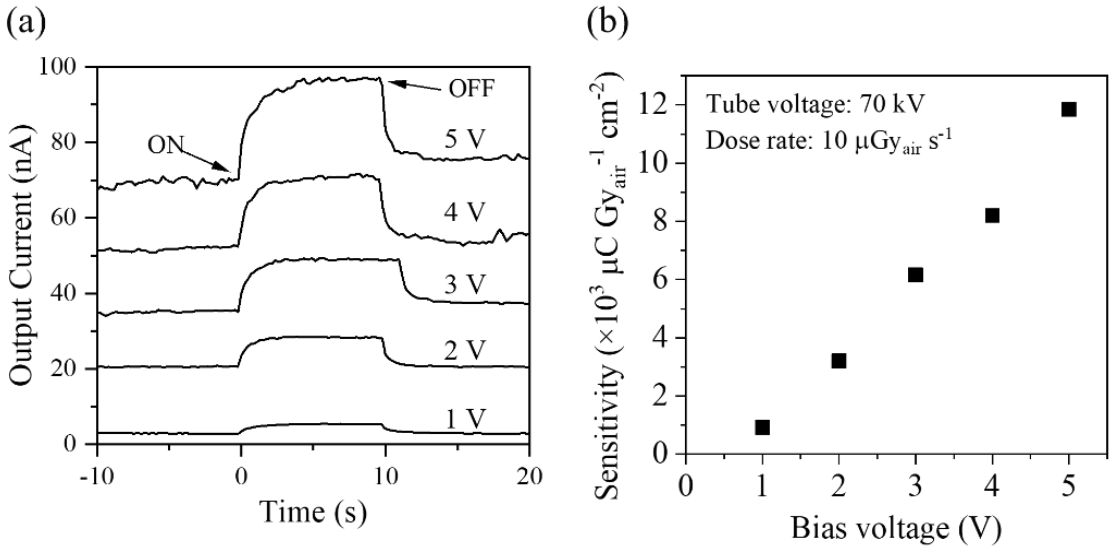

Figure 4-3| (a) X-ray responses and (b) sensitivities of the W/$CsPbBr_3$/polymer/Pt detector under bias voltages ranging from 1–5 V.

4.4 Conclusion

In this chapter, to demonstrate the X-ray detection application capability, $CsPbBr_3$ thick films were fabricated by using the mist deposition method. A polymer was used as a buffer layer to prevent the film exfoliation of a $CsPbBr_3$ film. Additionally, an X-ray detector based on a 110-μm-thick $CsPbBr_3$ film was successfully fabricated by using a scalable solution deposition method (mist deposition method). The detector demonstrated a sensitivity of 11,840 μC Gy_{air}^{-1} cm^{-2}, which is approximately 600 times higher than that of the currently available commercial a-Se X-ray detectors. This investigation provides a scalable method to fabricate high-sensitivity X-ray detectors based on the $CsPbBr_3$ thick film.

References for Chapter 4

1. Wei, W. *et al.* Monolithic integration of hybrid perovskite single crystals with heterogenous substrate for highly sensitive X-ray imaging. *Nature Photonics* **11**, 315–321 (2017).

2. Kim, Y. C. *et al.* Printable organometallic perovskite enables large-area, low-dose X-ray imaging. *Nature* **550**, 87–91 (2017).

3. Fu, R. *et al.* Stability Challenges for Perovskite Solar Cells. *ChemNanoMat* **5**, 253–265 (2019).

4. Stoumpos, C. C. *et al.* Crystal Growth of the Perovskite Semiconductor $CsPbBr_3$: A New Material for High-Energy Radiation Detection. *Crystal Growth & Design* **13**, 2722–2727 (2013).

5. He, Y. *et al.* High spectral resolution of gamma-rays at room temperature by perovskite $CsPbBr_3$ single crystals. *Nature Communications* **9**, 1609 (2018).

6. Gou, Z. *et al.* Self-Powered X-Ray Detector Based on All-Inorganic Perovskite Thick Film with High Sensitivity Under Low Dose Rate. *physica status solidi (RRL) – Rapid Research Letters* **13**, 1900094 (2019).

7. Pan, W. *et al.* Hot-Pressed $CsPbBr_3$ Quasi-Monocrystalline Film for Sensitive Direct X-ray Detection. *Advanced Materials* **31**, 1904405 (2019).

8. Yakunin, S. *et al.* Detection of X-ray photons by solution-processed lead halide perovskites. *Nature Photonics* **9**, 444–449 (2015).

9. Wei, H. *et al.* Sensitive X-ray detectors made of methylammonium lead tribromide perovskite single crystals. *Nature Photonics* **10**, 333–339 (2016).

10. Basiricò, L. *et al.* Detection of X-Rays by Solution-Processed Cesium-Containing Mixed Triple Cation Perovskite Thin Films. *Advanced Functional Materials* **29**, 1902346 (2019).

11. Kasap, S. O. X-ray sensitivity of photoconductors: application to stabilized a-Se. *Journal of Physics D: Applied Physics* **33**, 2853–2865 (2000).

Chapter 5
Lead-Free Perovskites for X-Ray Detectors

5.1 Introduction

From Chapter 2 to Chapter 4, the $CsPbBr_3$ films with good capability for solar cell and X-ray detector applications were fabricated by using the mist deposition method. The unique structure of the $CsPbBr_3$ films, which is consisted of columnar grains, is assumed to be one of the origins of the high performance. In this chapter, the author generalizes the mist deposition method to the fabrication of columnar grains of the other promising material that is $Cs_2AgBiBr_6$. In addition, the columnar grain growth mechanism is investigated to establish the general knowledge on the fabrication in the mist deposition method. The significance of fabrication of $Cs_2AgBiBr_6$ columnar grains is described in detail as follows:

While lead halide perovskites, including $CsPbBr_3$, have attracted much attention, lead toxicity has remained an inevitable issue. As a solution to the toxicity problem, Tang's group first reported lead-free double perovskite ($Cs_2AgBiBr_6$) single-crystal X-ray detectors in 2017.[1] Two years later, they improved the quality of $Cs_2AgBiBr_6$ single crystals through a controlled cooling process for synthesis, achieving a high X-ray sensitivity of 1,974 μC Gy_{air}^{-1} cm^{-2},[2] more than 98 times that of state-of-the-art a-Se X-ray detectors (20 μC Gy_{air}^{-1} cm^{-2}).[3] Clearly, non-toxic $Cs_2AgBiBr_6$ shows great potential for X-ray detection applications.[1,2,4–11] However, polycrystalline $Cs_2AgBiBr_6$ thick films, which can be easily scaled up for imaging devices, have achieved a sensitivity of only up to 250 μC Gy_{air}^{-1} cm^{-2} because of their high trap densities at grain boundaries.[7,8] Considering that it is difficult to prepare large single crystals and integrate them with readout circuits for imaging, a fabrication process for high-quality polycrystalline $Cs_2AgBiBr_6$ thick films is required to realize highly sensitive X-ray imaging devices. Although an exceptionally high sensitivity of 18,000 μC Gy_{air}^{-1} cm^{-2} has been reported using $Cs_2AgBiBr_6$ thin films, this result was obtained under conditions that facilitate high

sensitivity, i.e., extremely low dose rate (145.2 nGy_{air} s^{-1}) and high bias voltage (~1,667 V mm^{-1}).[9]

The formation of a columnar grain structure in the photoconductive layer is a promising solution to improve the sensitivity because a polycrystalline film composed of columnar grains has few grain boundaries across the direction of electron–hole pair collection. In fact, polycrystalline HgI_2 films with a columnar grain structure for X-ray detectors have shown excellent electrical properties, close to those of single crystals.[12,13] In the case of perovskite films, the advantages of columnar grains have been reported for developing highly efficient perovskite solar cells.[14–17] Cao *et al.* found that $MAPbI_3$ films with columnar grains exhibit a low trap density of 1.96×10^{16} cm^{-3}. The $MAPbI_3$-based solar cell achieved a high power conversion efficiency (PCE) of 15.14%, whereas the one without columnar grains exhibited a relatively high trap density of 6.37×10^{16} cm^{-3} and a low PCE of 11.30%.[14] Eggers *et al.* reported the fabrication of 1.5-μm-thick multi-cation perovskite films with columnar grains via inkjet printing and demonstrated the highest PCE of over 21% in inkjet-printed perovskite solar cells.[15] Similarly, perovskite films with columnar grains are expected to achieve high X-ray sensitivity. However, the thickness of the previously reported perovskite films with columnar grains is less than 2 μm, which is optimized for the absorption of visible light, not X-rays. Unfortunately, the fabrication of $Cs_2AgBiBr_6$ thick films with columnar grains has not been realized.

Herein, the author proposes the mist deposition method for the columnar grain growth of $Cs_2AgBiBr_6$ films. In Chapter 4, the author demonstrated that a 110-μm-thick $CsPbBr_3$ thick film can exhibit a high sensitivity of 11,840 μC Gy_{air}^{-1} cm^{-2}, which is comparable to that achieved by a single crystal.[18,19] In this chapter, the author demonstrates the columnar grain growth of a $Cs_2AgBiBr_6$ film using the mist deposition method. Additionally, to clarify the mechanism of columnar grain growth, the effects of fabrication conditions, including the precursor solution concentration and substrate temperature, on the film growth are investigated.

5.2 Experimentals

Materials and Precursor Solutions

Cesium bromide (CsBr, 99.999%), silver bromide (AgBr, 99%), and bismuth bromide ($BiBr_3$, 98%) were purchased from Sigma-Aldrich. Dimethyl sulfoxide (DMSO, 99.0%) and N, N-dimethylformamide (DMF, 99.5%) were purchased from Fujifilm Wako Chemicals. The precursor solution was prepared by dissolving CsBr, AgBr, and $BiBr_3$ (in a molar ratio of 2:1:1) in a mixed solvent of DMSO and DMF (1:1, v/v). For the saturation test, $Cs_2AgBiBr_6$ powder was synthesized using the previously reported method.[20]

Preparation of Perovskite Films

$Cs_2AgBiBr_6$ films were prepared using a mist deposition method (Figure 1a) as reported previously.[18] Glass substrates (25 × 25 mm^2) were cleaned by sonication in distilled water, acetone, and 2-propanol for 10 min, respectively. The precursor solution was atomized by ultrasonic vibration at 2.4 MHz. The generated mist was then transported by nitrogen gas to a nozzle with a rectangular aperture (30 × 1 mm^2), which supplied the mist repeatedly to a preheated substrate in the form of a curtain-like flow. The flow rates of the carrier and dilution gases were set to 0.40 and 4.60 L min^{-1}, respectively. The forward and backward movement speeds were set to 0.16 mm s^{-1} and 15.00 mm s^{-1}, respectively. The deposition cycle, which is defined as a set of forward and backward movements of the substrate, was repeated to control the film thickness. To investigate the early growth stage, conductive indium tin oxide (ITO) substrates (25 × 25 mm^2) were used for ease of observation using scanning electron microscopy (SEM). To observe the precipitation formed from a mist droplet, we focused on the edge on the substrate, which is only reached by few mist droplets, and found an isolated circular precipitation.

Device Fabrication

An X-ray detector with the configuration of W/$Cs_2AgBiBr_6$/Pt (W; tungsten, Pt; platinum) was fabricated as follows. $Cs_2AgBiBr_6$ thick films were deposited on the Pt-coated ITO substrates (hereinafter termed as Pt substrates, size: 26 × 20 mm^2). To obtain sufficient thickness for X-ray absorption, the deposition cycle was repeated 200 times. Subsequently, W electrodes were deposited on $Cs_2AgBiBr_6$ using ion sputtering coating. A device area of 0.25 cm^2 was determined using a metal mask.

Characterization and Measurements

The X-ray diffraction (XRD) spectra of the $Cs_2AgBiBr_6$ films were recorded using an X-ray diffractometer (X'Pert PRO-MPD, PANalytical) with Cu-Kα radiation. The surface and cross-sections of the films were observed using the scanning electron microscopy (SEM; JSM-6510LV, JEOL) and field emission scanning electron microscopy (FE-SEM; JSM-IT300HR, JEOL). The grain size was defined as the diameter of circles corresponding to the area of the grain determined from the surface SEM image. Elemental investigations were carried out using the energy-dispersive X-ray (EDX) analysis system attached to the SEM instrument.

The crystal orientation of (hkl) plane was quantified using the orientation factor $F_{(hkl)}$ defined by the following equation:

$$F_{(hkl)} = \left[I_{(hkl)} / I_{(220)} \right]_{\text{sample}} / \left[I_{(hkl)} / I_{(220)} \right]_{\text{reference}}$$

where $I_{(hkl)}$ is the intensity of the XRD peak derived from the (hkl) plane.

The photoresponse characteristics of the X-ray detector were measured using a W target X-ray source. The tube voltage and tube current used in the measurement were 70 kV and 2.0 mA, respectively. The dose rate of the X-ray was 10 $\mu Gy_{air}\ s^{-1}$, as measured using an ionized-chamber-type survey meter. The measurements were performed in a dark room to exclude the effect of other photons, such as those of visible light.

5.3 Results and Discussion

5.3.1 Investigation of $Cs_2AgBiBr_6$ Saturation Concentration

To investigate the saturation concentration of $Cs_2AgBiBr_6$ for the solvent mixture of DMSO and DMF (1:1, *v*/*v*), 1.16 mmol $Cs_2AgBiBr_6$ powders were added to the solvent (Figure 5-1a, b). As shown in Figure 5-1c and Figure 5-1d, white precipitates remained even after 3 hours of stirring. The white precipitates seemed to be CsBr. After adding a total solvent amount of 6 mL, complete dissolution was confirmed (Figure 5-1e). Based on the above results, the saturation concentration was identified to be 193–232 mM. These experiments were performed at 20±5 °C.

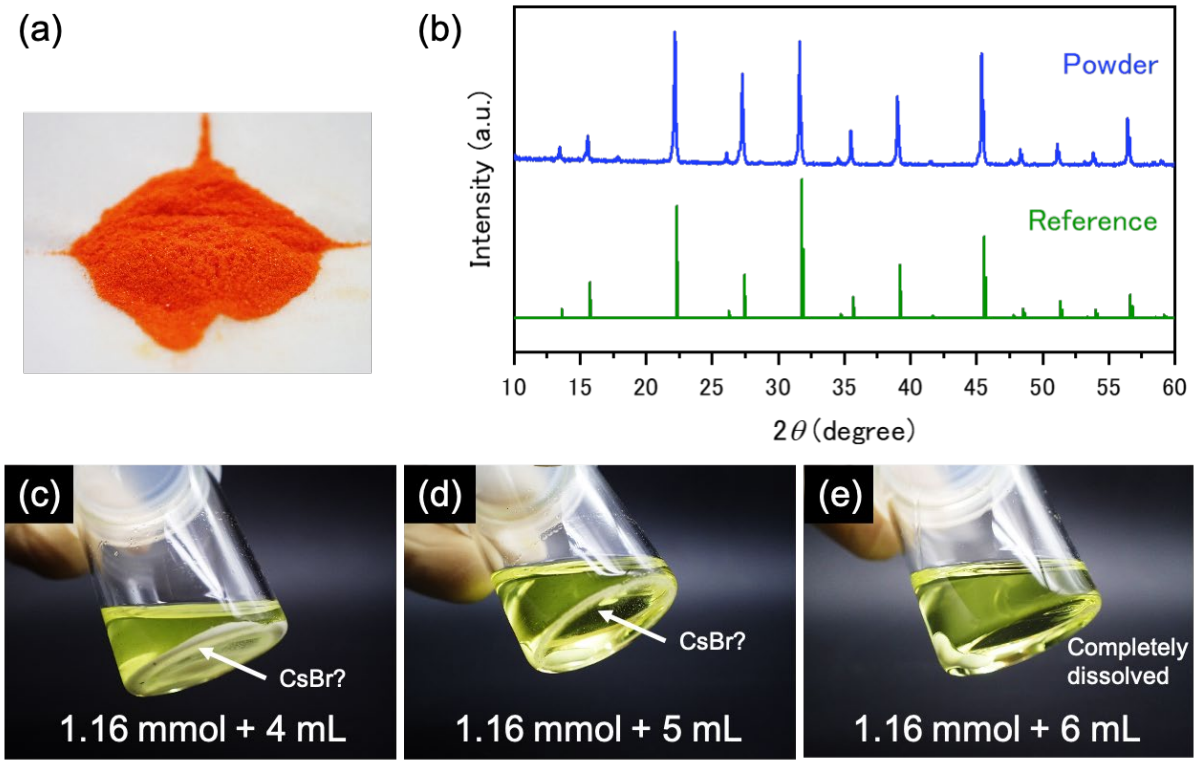

Figure 5-1| (a) A photograph and (b) XRD pattern of the prepared $Cs_2AgBiBr_6$ powders. (c–e) Saturation test by adding (c) 4 mL, (d) 5 mL, and (e) 6 mL DMSO-DMF solvent to 1.16 mmol $Cs_2AgBiBr_6$ powders.

5.3.2 Preparation of $Cs_2AgBiBr_6$ Films

In the mist deposition method, the precursor solution concentration is typically set lower than 20% of the saturation concentration to avoid the precipitation of the solutes before arriving at the substrate.[18,19,21] Subsequently, the author first identified the saturation concentration of $Cs_2AgBiBr_6$ for the solvent mixture of DMSO and DMF to be approximately 200 mM (Figure 5-1). Considering the saturation concentration, the author performed mist deposition using the 25 mM solution and characterized the resulted film by XRD and EDX to establish the applicability of the mist deposition for fabricating $Cs_2AgBiBr_6$ films. The substrate temperature was set to 150 °C, which is optimized for $CsPbBr_3$ film fabrication in Chapter 2.

As shown in Figure 5-2a, an orange-colored film was uniformly obtained on the substrate. The XRD pattern of the film corresponded to that of cubic $Cs_2AgBiBr_6$[22] (Figure 5-2b). Additionally, an EDX analysis revealed that the atomic contents of Cs, Ag, Bi, and Br in the film were 19.2%, 10.1%, 9.8%, and 60.9%, respectively, which almost corresponded to the $Cs_2AgBiBr_6$ stoichiometry (Figure 5-2c). The XRD and EDX demonstrated the applicability of the mist deposition method for the formation of $Cs_2AgBiBr_6$ films. As shown in the surface and cross-sectional SEM images (Figure 5-3), the $Cs_2AgBiBr_6$ film is homogeneous, composed of compact grains, and fully covers the substrate. The measurement of the film thickness at 100 points randomly selected from the entire area (25 × 25 mm^2) revealed that the average thickness and standard deviation were 1.93 μm and 0.14 μm, respectively (Figure 5-4). The standard deviation is much lower than that (0.37 μm) of previously reported 1.7-μm-thick $MAPbI_3$ films prepared using an air-brush,[23] confirming the excellent uniformity of the coating realized using the mist deposition method.

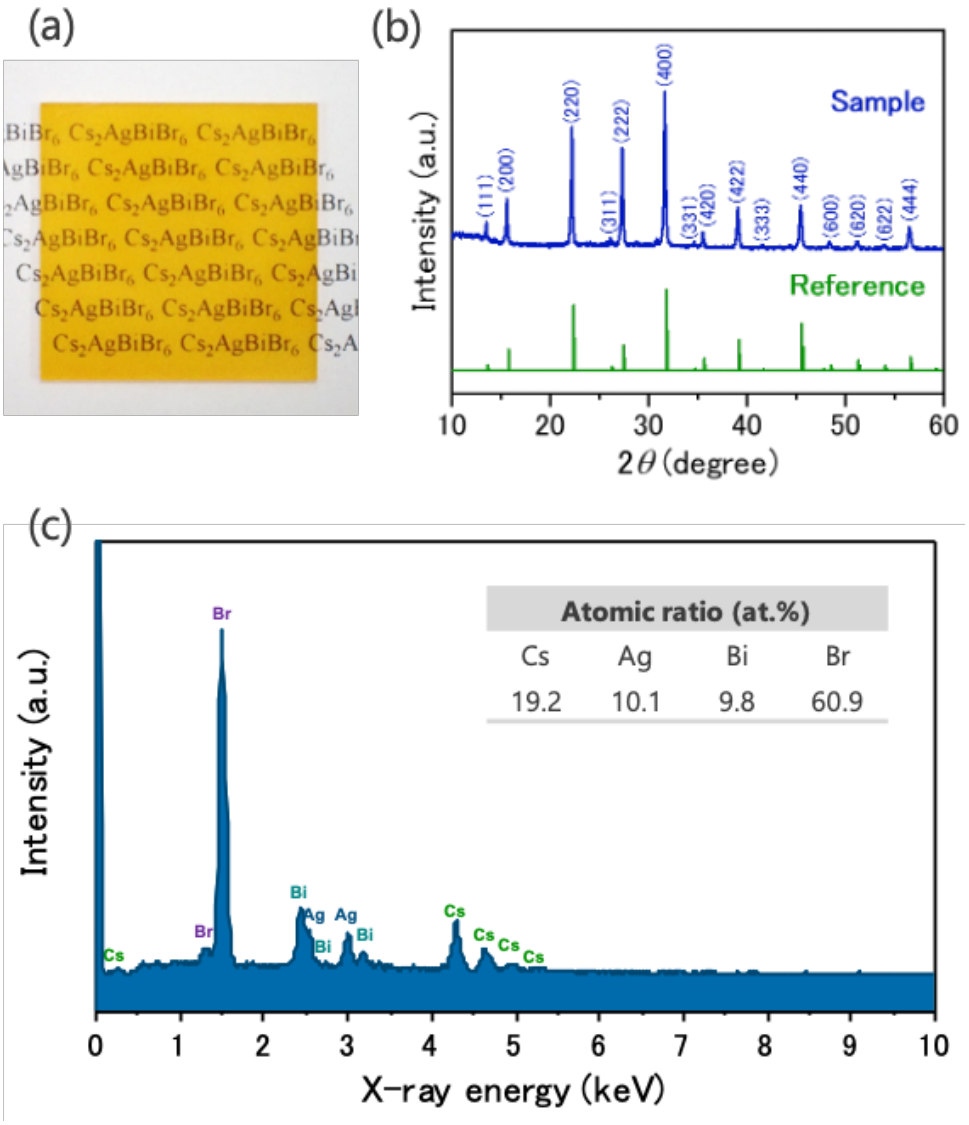

Figure 5-2| (a) An image, (b) XRD pattern, (c) EDX spectrum and the corresponding atomic ratio of the obtained film.

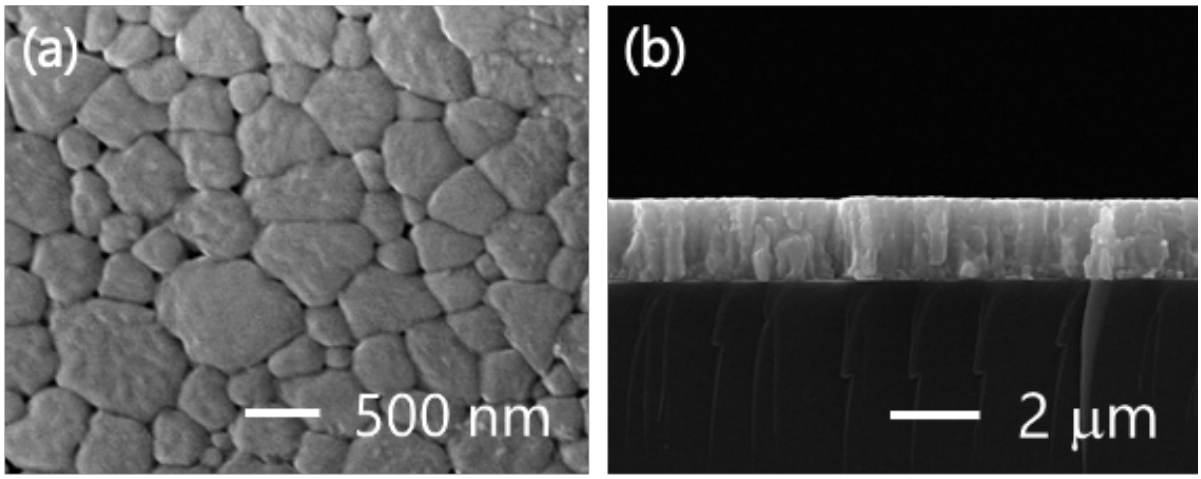

Figure 5-3| (a) Surface and (b) cross-sectional SEM images of the obtained $Cs_2AgBiBr_6$ film.

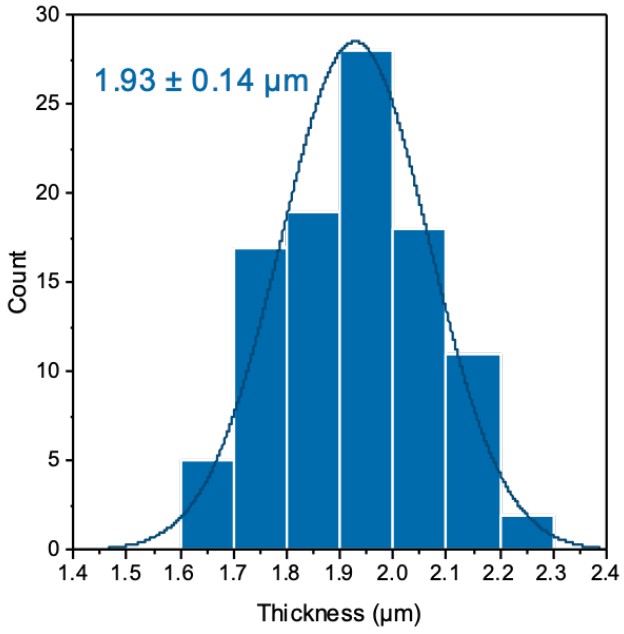

Figure 5-4| Histogram of thicknesses measured at randomly selected points in the 1.9-µm-thick $Cs_2AgBiBr_6$ film.

5.3.3 Effects of Precursor Solution Concentration on $Cs_2AgBiBr_6$ Growth

To investigate the effect of the precursor solution concentration on the film growth, $Cs_2AgBiBr_6$ films were prepared using 25 mM and 75 mM solutions. The number of deposition cycles was varied in the range of 6–40 to control the film thickness. In the case of the 25 mM solution, the crystal grains grew in a direction perpendicular to the substrate and became columnar grains (Figure 5-5a–c), demonstrating the fabrication of columnar grains via the mist deposition method. Interestingly, although the film was prepared by repeating the deposition cycle up to 40 times, a vertical columnar structure was formed, not a layer-by-layer structure. On the other hand, in the case of the 75 mM solution, the pre-deposited grains did not grow, and the small crystal grains piled up one after another (Figure 5-5d–f). These results indicate that the concentration of the precursor solution plays an important role in the columnar grain growth.

Figure 5-5g, h shows the XRD patterns of the $Cs_2AgBiBr_6$ films. From all the samples, noticeable peaks derived from the (200), (220), (222), (400), (422), and (440) planes of cubic $Cs_2AgBiBr_6$ could be detected. Interestingly, focusing on the (220) and (400) planes, in the case of the 25 mM solution, the peak intensity of the (400) plane, denoted by $I_{(400)}$, increased with the thickness, whereas $I_{(220)}$ remained unchanged (Figure 2i), suggesting the preferential growth along the [100] direction. Such a preferential growth was also confirmed in chapter 2, which reveals that $CsPbBr_3$ films with columnar grains show a high (101)-orientation, suggesting a correlation between columnar growth and preferential orientation. On the other hand, in the case of the 75 mM solution, the peak intensities from the crystal planes did not correlate with the thickness. In other words, no sign of preferential orientation was observed.

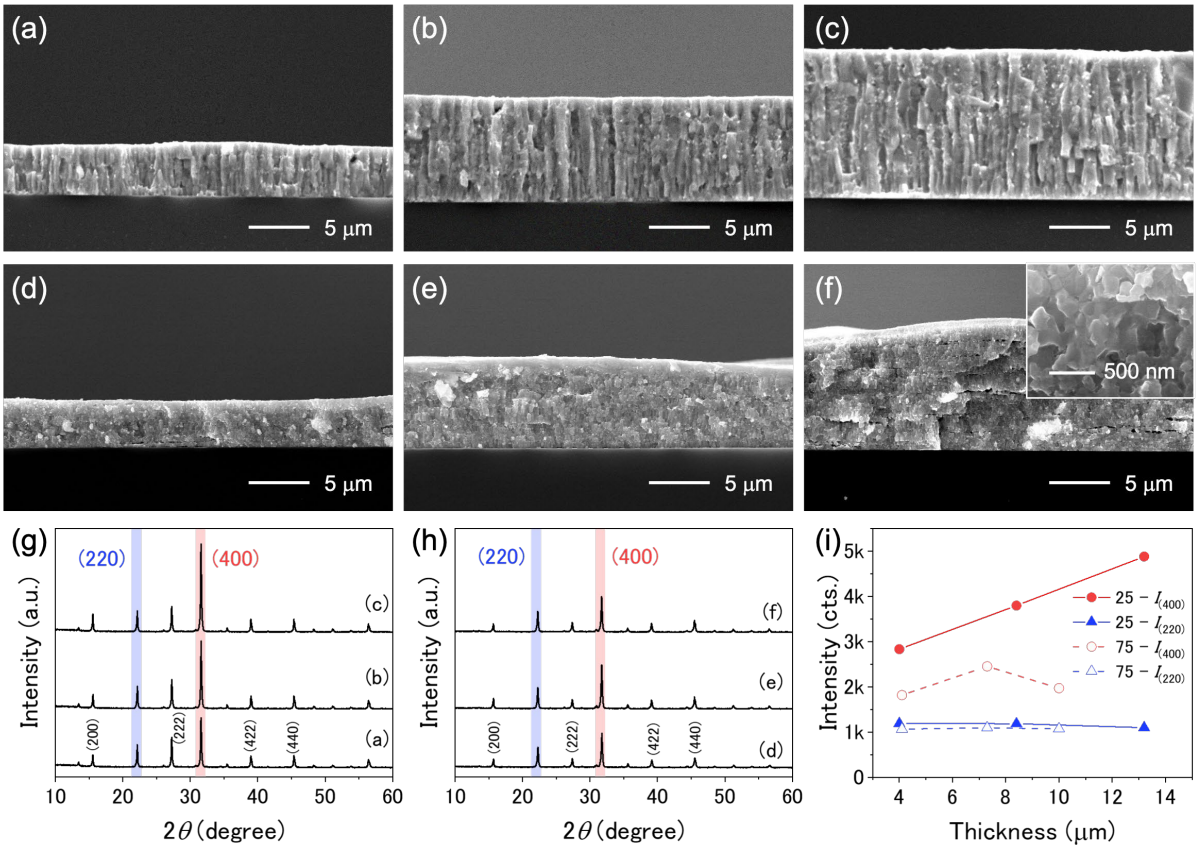

Figure 5-5| (a–f) Cross-sectional SEM images of the $Cs_2AgBiBr_6$ films prepared from (a–c) 25 mM and (d–f) 75 mM solutions. The number of deposition cycles was 13, 27, 40, 6, 12, and 18 for these samples, respectively. (g, h) Corresponding XRD patterns of the $Cs_2AgBiBr_6$ films shown in Figure 2a–f. (i) Correlation between thickness and peak intensity.

To reveal the growth mechanism in the mist deposition process, the author focused on the early growth stage and investigated the morphology of the film formed after one and five deposition cycles. In the case of the 25 mM solution, the $Cs_2AgBiBr_6$ film with a flat surface was formed after the first deposition (Figure 5-6a), and the average grain size increased from 216 nm to 443 nm as the number of deposition cycles increased (Figure 5-6b). On the other hand, in the case of the 75 mM solution, precipitates with the shape of overlapping circles were formed after the first deposition (Figure 5-6c), and an average grain size of 62 nm remained almost unchanged even after five deposition cycles (Figure 5-6d). In the mist deposition process, droplets of the precursor solution, namely the mist solution, are continuously supplied to the substrate. The droplets reach the substrate, and crystals are deposited as the solvent evaporates. Owing to the continuous supply of fresh droplets, the crystals are wetted by the droplets arriving later. Since 25 mM is much lower than the saturation concentration (200 mM), the author supposes that the mist solution re-dissolved the pre-deposited crystals and merged them into larger crystal grains after solvent evaporation. This type of grain growth process has been reported for spray-coated $MAPbI_{3-x}Cl_x$ films[24] and $MAPbI_3$ films.[25] In contrast, when the 75 mM solution was used, no grain growth occurred, and overlapping circle precipitates were formed. As the diameter of the circle is largely the same as that of the mist droplets (Figure 5-7), each circular precipitate seems to have been directly formed from a mist droplet, indicating that the mist solution hardly re-dissolved the pre-deposited crystals. Given that grain growth occurred only when the low concentration (25 mM) solution was used, the author believes that the capability of the mist solution to re-dissolve the pre-deposited crystals, which is defined as the re-dissolution capability, is a key factor that promotes grain growth, leading to columnar grain growth in the mist deposition process.

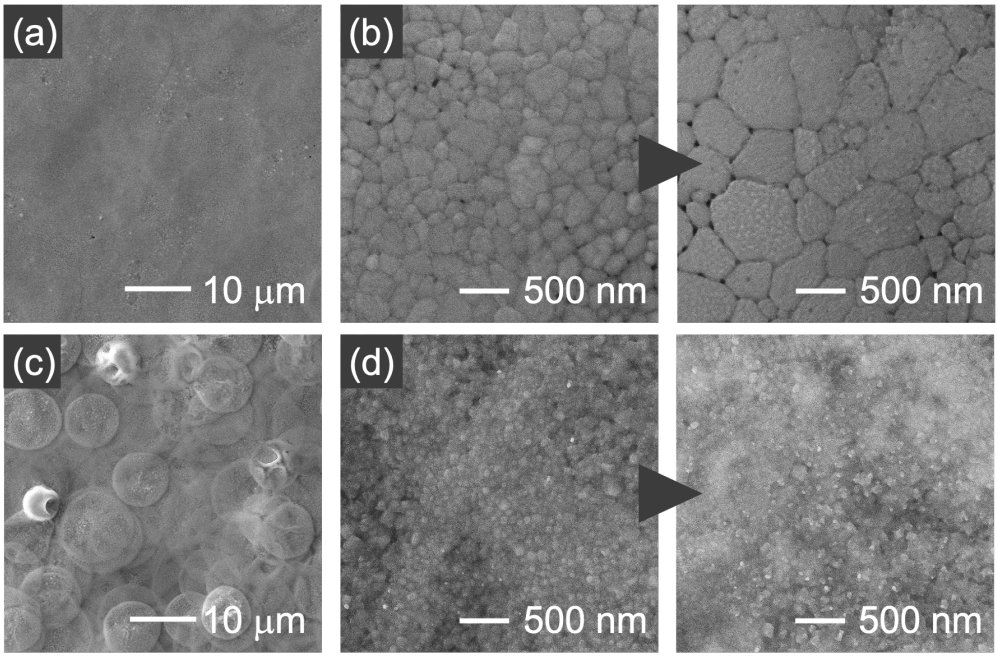

Figure 5-6| Surface SEM images of the $Cs_2AgBiBr_6$ films prepared from (a, b) 25 mM and (c, d) 75 mM solutions. The left and right images in **Figure 5-6**b, d show the surfaces after one and five deposition cycles, respectively.

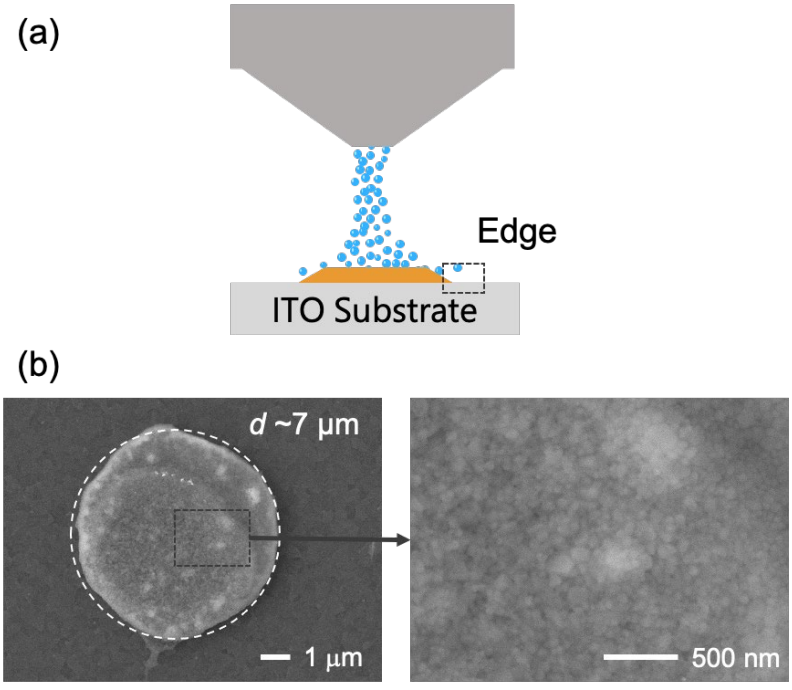

Figure 5-7| (a) Schematic of the mist droplets reaching the substrate. (b) SEM images of the precipitation formed from a mist droplet.

5.3.4 Effects of Substrate Temperature on $Cs_2AgBiBr_6$ Growth

The author investigated the effects of substrate temperature by preparing $Cs_2AgBiBr_6$ films in the temperature range of 110–210 °C using the 25 mM solution. The deposition cycle was repeated 20 times to form a film thick enough for easy observation of the cross-section structure. When the substrate temperature was low (110 °C), a $Cs_2AgBiBr_6$ film composed of columnar grains was formed; however, the film surface contained dents, and the grains tilted toward the dents (Figure 5-8a). This poor morphology was attributed to the extremely slow solvent evaporation.[18] On the other hand, when the substrate temperature was in the range of 130–190 °C, relatively uniform $Cs_2AgBiBr_6$ films with vertical columnar grains could be obtained as shown in Figure 5-8b, which present a representative SEM image of the film prepared at 150 °C and those of the others, respectively. When the substrate temperature was too high (210 °C), an extremely thin $Cs_2AgBiBr_6$ film was formed with many spherical particles on the film surface (Figure 5-8c). These spherical particles are probably $Cs_2AgBiBr_6$ powders precipitated by the complete evaporation of the solvent before the mist droplets reached the substrate. The thin $Cs_2AgBiBr_6$ film contained small grains, approximately 200 nm in diameter as shown in the inset of Figure 5-8c. Interestingly, the grain size measured from the surface SEM images decreased from over 2 μm to approximately 0.2 μm with increasing substrate temperature (Figure 5-8d). A high substrate temperature leads to fast solvent evaporation, and thus, the re-dissolution capability of the mist solution becomes low due to a lack of re-dissolution time. Therefore, it is considered that the low re-dissolution capability impeded the grain growth process, thereby decreasing the grain size. Notably, the XRD patterns of the films corresponded to that of cubic $Cs_2AgBiBr_6$ (Figure 5-9). Moreover, all the $Cs_2AgBiBr_6$ films with columnar grains showed preferential crystal orientation. Although the preferential growth direction of $Cs_2AgBiBr_6$ varies from [100] to [111] depending on the substrate temperature (Figure 5-10), the rational reason is under consideration.

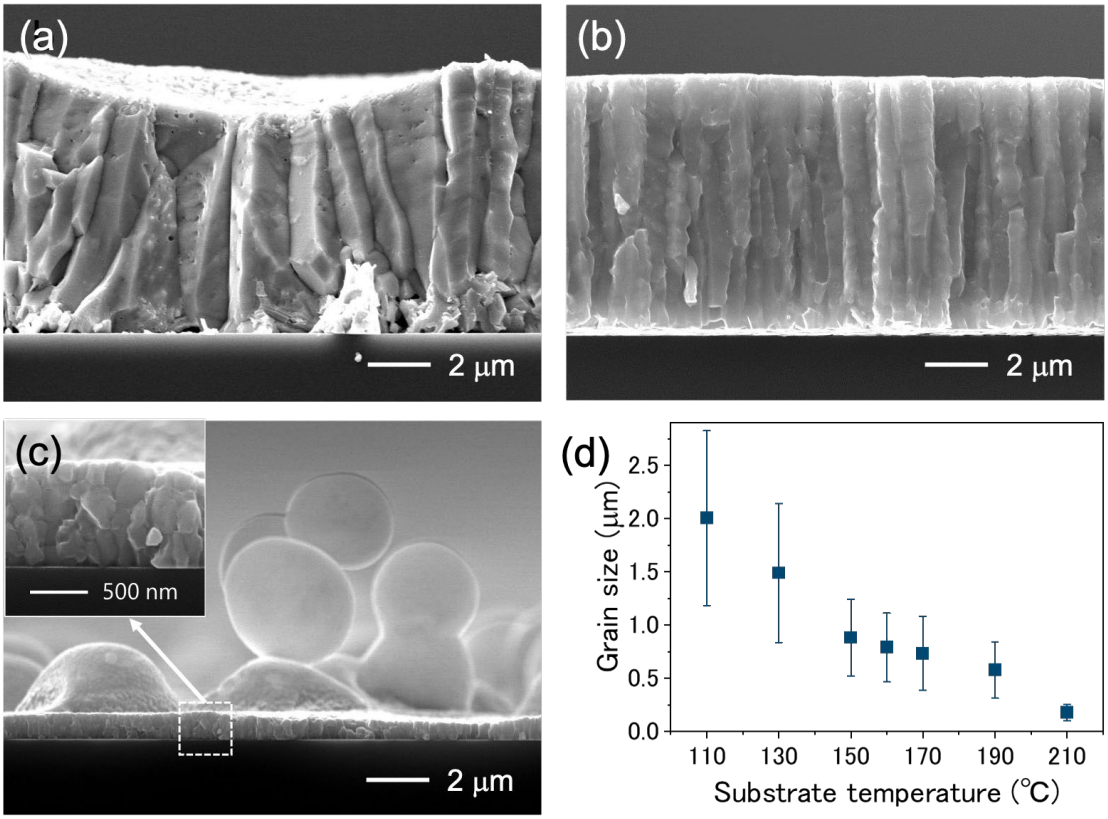

Figure 5-8| (a–c) Cross-sectional SEM images of $Cs_2AgBiBr_6$ films prepared at substrate temperatures of (a) 110, (b) 150, and (c) 210 °C. (d) Correlation between average grain size and substrate temperature.

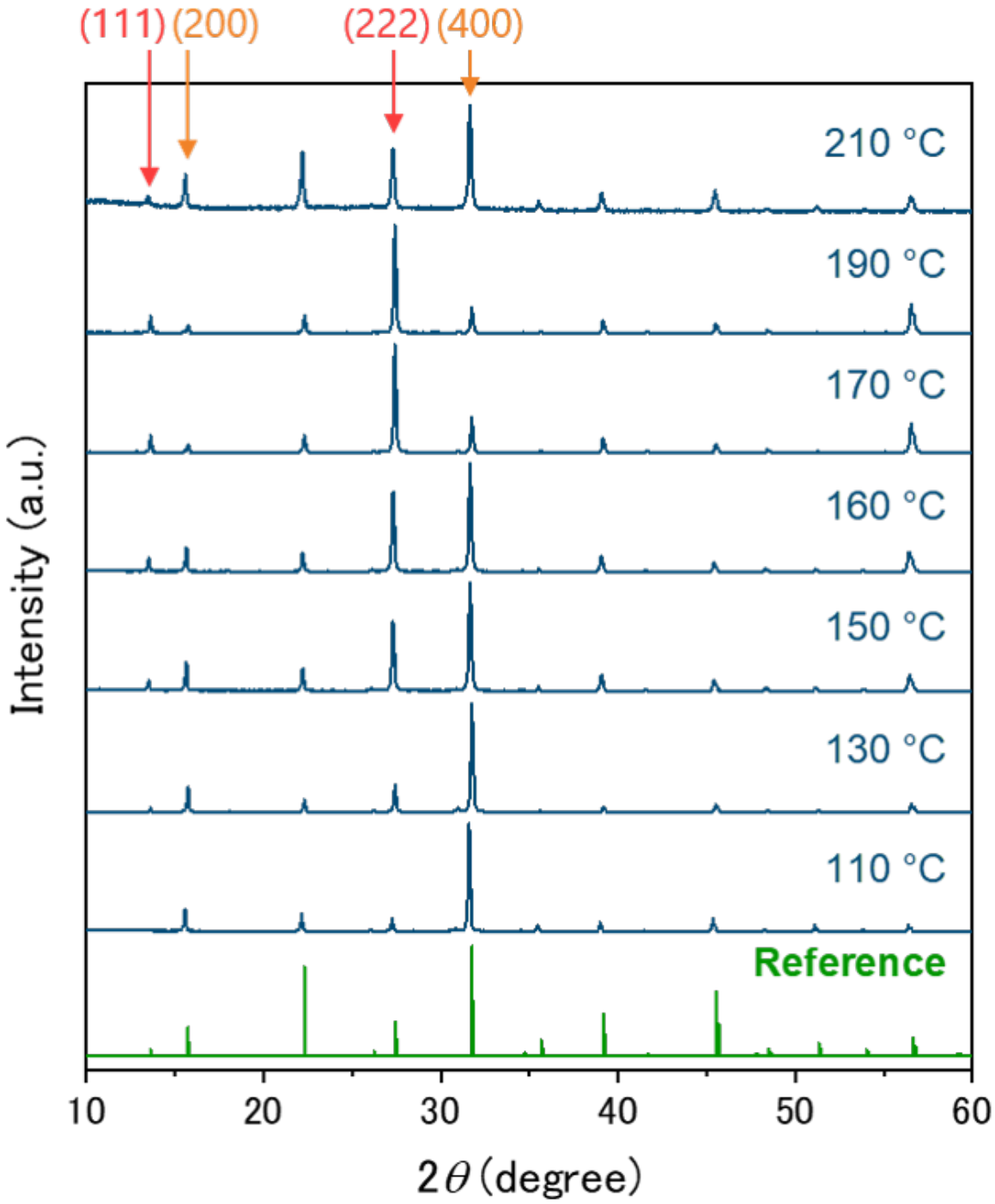

Figure 5-9| XRD patterns of the $Cs_2AgBiBr_6$ films prepared at 110–210 °C.

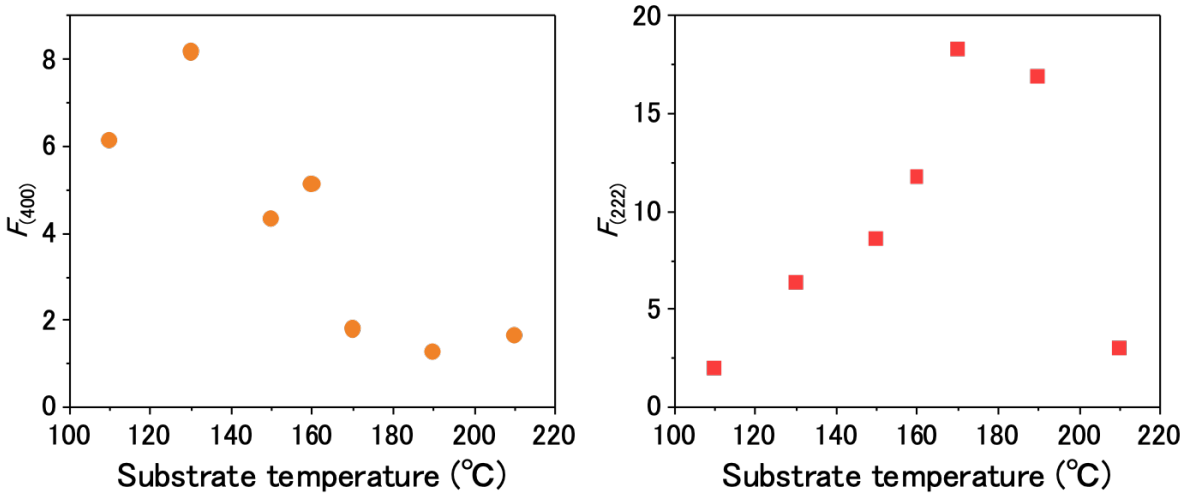

Figure 5-10| Correlation between (100)-orientation/(111)-orientation and substrate temperature.

5.3.5 Mechanism of Columnar Grain Growth in the Mist Deposition

Based on a series of experiments, the mechanism of columnar grain growth in the mist deposition process can be summarized as shown in Figure 5-11. In this process, the mist solution continuously supplied to the substrate and forms a wetted region on the pre-deposited crystal surface (Figure 5-11a). Herein, the author proposes that the capability of the mist solution to re-dissolve the pre-deposited crystals (re-dissolution capability) affects the growth mode in the wetted region (Figure 5-11b). When the re-dissolution capability is high, a sufficiently wetted region is formed to promote grain growth, as illustrated on the top in Figure 5-11b. In contrast, when the re-dissolution capability is low, the wetted region is not sufficiently formed, and thus, grain growth hardly occurs, and the frequency of the nucleation increases as shown on the bottom in Figure 5-11b. As a result, various structures depending on the re-dissolution capability are obtained as shown in Figure 5-11c. Notably, the re-dissolution capability can be changed by deposition conditions, such as the precursor solution concentration and substrate temperature. When the re-dissolution capability is too low, numerous small grains pile up one after another because of the frequent nucleation. This structure was observed in the $Cs_2AgBiBr_6$ films prepared at too high substrate temperatures or high precursor solution concentrations

(Figure 5-5d–f, and Figure 5-8c). When the re-dissolution capability is above a certain level, owing to the growth-dominant condition, columnar grains are formed as a result of the continuous grain growth on the film surface, as demonstrated in Figure 5-5a–c and Figure 5-8b. The grain size, which is the width of the columnar grains, increases with the re-dissolution capability owing to the facilitated grain growth (Figure 5-8d). When the re-dissolution capability is too high, some dents are formed on the film surface probably because of the extremely slow solvent evaporation (Figure 5-8a). Similarly, many dents were formed on the film fabricated from the precursor solution with a low concentration (2.5 mM; Figure 5-12), further supporting the adverse effects of a too high re-dissolution capability. Overall, it is concluded that the re-dissolution capability of the mist solution is a key factor for columnar grain growth in the mist deposition process. Additionally, in terms of the re-dissolution capability, the author realized the columnar grain growth of $MAPbBr_3$ (Figure 5-13) in addition to that of $Cs_2AgBiBr_6$ and previously reported $CsPbBr_3$, demonstrating the generality of the mist deposition method for columnar grain growth.

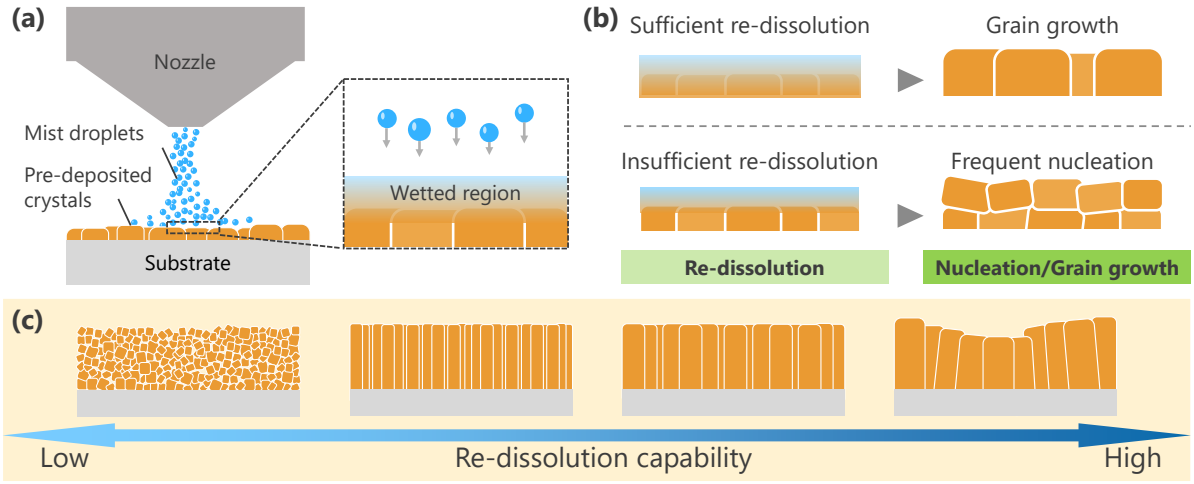

Figure 5-11| Schematics of (a) Formation of a wetted region by the arriving mist solution, (b) Difference in growth modes in the wetted region, and (c) Film structures depending on the re-dissolution capability of the arriving mist solution.

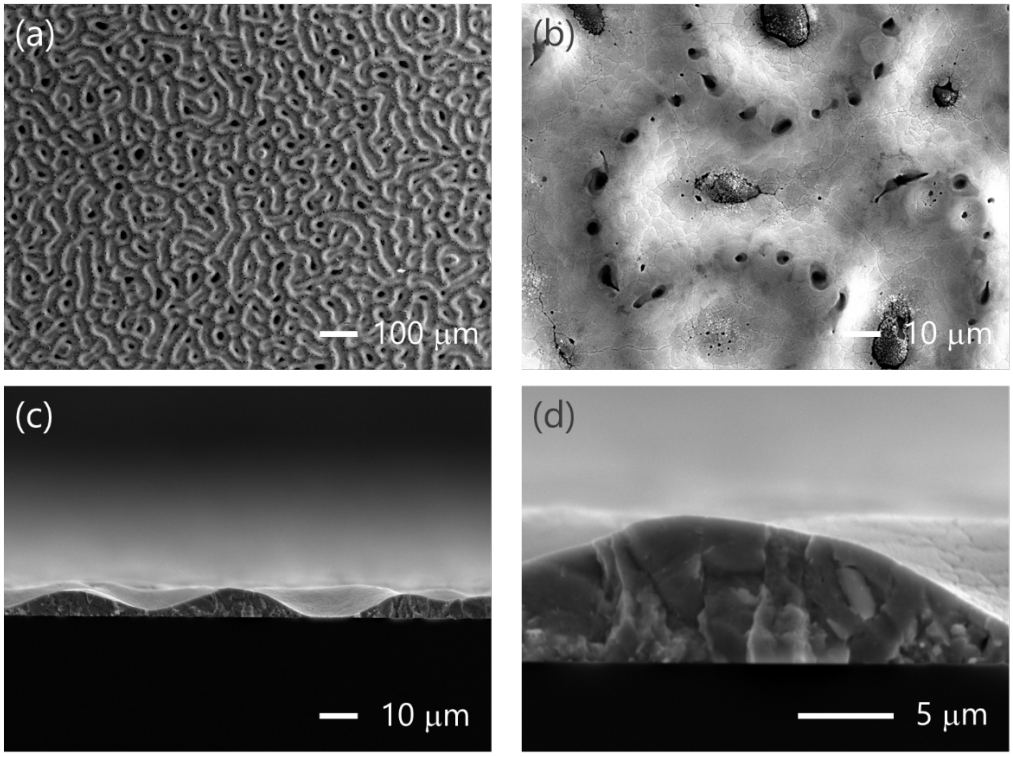

Figure 5-12| (a, b) surface and (c, d) cross-sectional SEM images of the $Cs_2AgBiBr_6$ film prepared from the 2.5 mM solution.

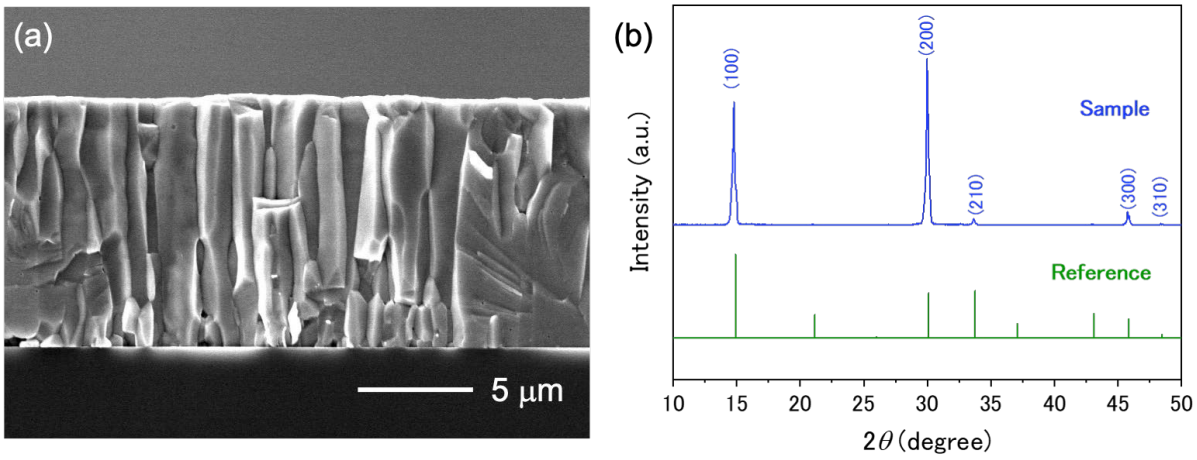

Figure 5-13| (a) Cross-sectional SEM image and (b) XRD pattern of the $MAPbBr_3$ film and the reference pattern of cubic $MAPbBr_3$.[26]

5.3.6 X-Ray Detection Performance of $Cs_2AgBiBr_6$ Films with Columnar Grains

To demonstrate the potential of $Cs_2AgBiBr_6$ films with columnar grains for X-ray detectors, a W/$Cs_2AgBiBr_6$/Pt detector is prepared by fabricating a 92-μm-thick $Cs_2AgBiBr_6$ film on a Pt substrate, followed by W coating (Figure 5-14a). The 92-μm-thick $Cs_2AgBiBr_6$ film was also composed of columnar grains, and the thickness was uniform over the entire area (Figure 5-14b). Under dark conditions, the X-ray detector showed an ohmic response (Figure 5-14c), and the resistivity of the $Cs_2AgBiBr_6$ thick film was calculated to be 1.0×10^{10} Ω cm, which is comparable to that of $Cs_2AgBiBr_6$ single crystals.[2] Figure 5-14d shows the photoresponses to X-rays with a dose rate of 10 $\mu Gy_{air}\ s^{-1}$ under bias voltages of 5 and 10 V (56 and 109 V mm^{-1}). The measured current increased under X-ray irradiation, indicating the detection of X-rays. The sensitivity was 208 μC $Gy_{air}^{-1}\ cm^{-2}$ at 5 V and increased to 487 μC $Gy_{air}^{-1}\ cm^{-2}$ at 10 V, which is the highest among detectors based on $Cs_2AgBiBr_6$ polycrystalline thick films (Table 5-1), demonstrating the significant potential of columnar grains for X-ray detection.

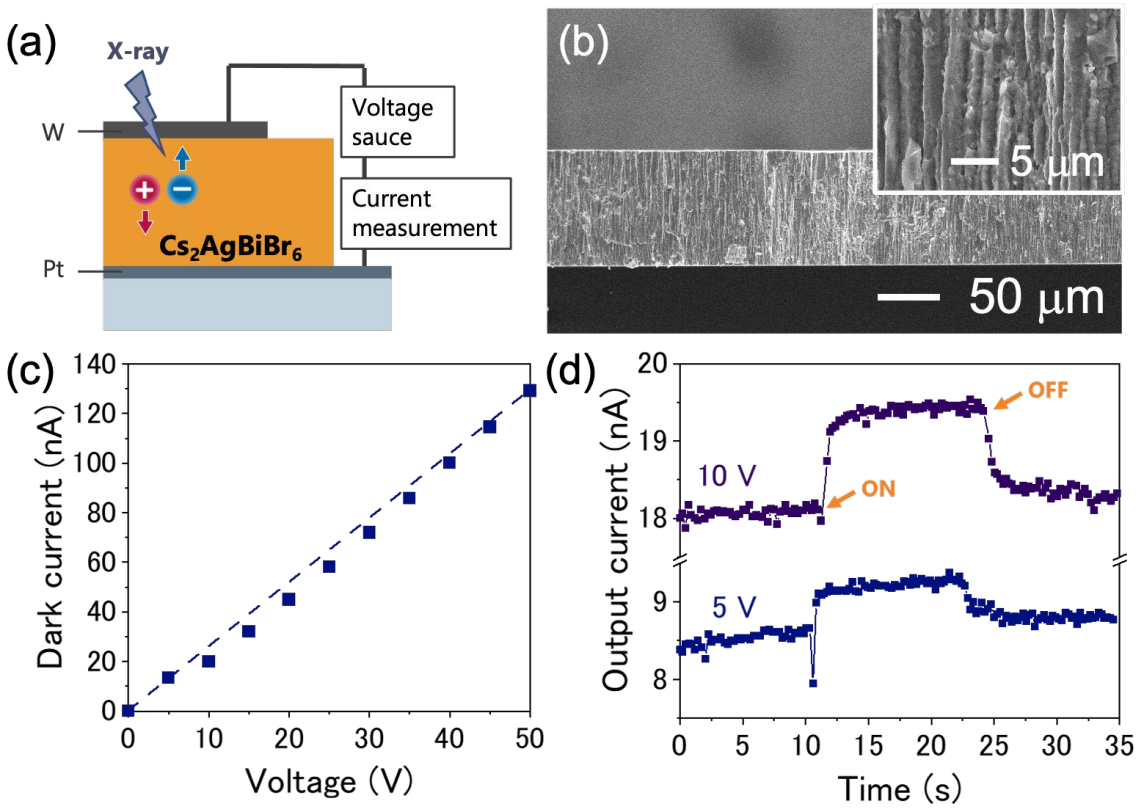

Figure 5-14| (a) Schematic of X-ray detection measurements. (b) Cross-sectional SEM image of a $Cs_2AgBiBr_6$ thick film fabricated on a Pt substrate. (c) Dark current and (d) X-ray responses of the X-ray detector.

Table 5-1| Sensitivities of previously reported X-ray detectors based on $Cs_2AgBiBr_6$.

Materials	Bias ($V\ mm^{-1}$)	Sensitivity ($\mu C\ Gy_{air}^{-1}\ cm^{-2}$)	Ref.
Single crystal	25	105	[1]
Single crystal	50	1,974	[2]
Single crystal	50	316	[4]
Single crystal	6	316	[5]
Single crystal	22.7	288.8	[6]
Polymer composited film	4,000	40	[7]
Wafer with BiOBr	500	250	[8]
Wafer	100	32	[8]
Thin film	~1,667	18,000	[9]
Thick film with columnar grains	109	487	This work

5.4 Conclusions

The mist deposition method was developed for fabricating $Cs_2AgBiBr_6$ films with columnar grain structures. Through the investigation of the effects of precursor solution concentration and substrate temperature, $Cs_2AgBiBr_6$ films with columnar grains could be fabricated. Based on a series of experiments, the author can summarize the mechanism of the columnar grain growth as follows: In the mist deposition process, the continuously supplying precursor mist re-dissolves the pre-deposited crystals and forms a wetted region on the film surface. When the re-dissolution capability is above a certain level, grain growth is promoted in the wetted region, leading to the formation of columnar grains. Thus, the author concludes that the re-dissolution capability of the precursor solution is a key factor in the formation of columnar grain structures. The re-dissolution capability can be tuned using the deposition conditions, such as the precursor solution concentration and substrate temperature. Finally, the author fabricated a 92-μm-thick $Cs_2AgBiBr_6$ film with columnar grains. An X-ray detector based on this film showed a high sensitivity of 487 μC Gy_{air}^{-1} cm^{-2}, which is the highest among detectors based on $Cs_2AgBiBr_6$ polycrystalline thick films, demonstrating the significant potential of columnar grains for X-ray detection.

References for Chapter 5

1. Pan, W. *et al.* $Cs_2AgBiBr_6$ single-crystal X-ray detectors with a low detection limit. *Nature Photonics* **11**, 726–732 (2017).

2. Yin, L. *et al.* Controlled Cooling for Synthesis of $Cs_2AgBiBr_6$ Single Crystals and Its Application for X-Ray Detection. *Advanced Optical Materials* **7**, 1900491 (2019).

3. Kasap, S. O. X-ray sensitivity of photoconductors: application to stabilized a-Se. *Journal of Physics D: Applied Physics* **33**, 2853–2865 (2000).

4. Steele, J. A. *et al.* Photophysical Pathways in Highly Sensitive $Cs_2AgBiBr_6$ Double-Perovskite Single-Crystal X-Ray Detectors. *Advanced Materials* **30**, 1804450 (2018).

5. Zhang, H. *et al.* X-Ray Detector Based on All-Inorganic Lead-Free $Cs_2AgBiBr_6$ Perovskite Single Crystal. *IEEE Transactions on Electron Devices* **66**, 2224–2229 (2019).

6. Yuan, W. *et al.* In Situ Regulating the Order–Disorder Phase Transition in $Cs_2AgBiBr_6$ Single Crystal toward the Application in an X-Ray Detector. *Advanced Functional Materials* **29**, 1900234 (2019).

7. Li, H. *et al.* Lead-free halide double perovskite-polymer composites for flexible X-ray imaging. *Journal of Materials Chemistry C* **6**, 11961–11967 (2018).

8. Yang, B. *et al.* Heteroepitaxial passivation of $Cs_2AgBiBr_6$ wafers with suppressed ionic migration for X-ray imaging. *Nature Communications* **10**, 1989 (2019).

9. Zhang, H. *et al.* Encapsulated X-Ray Detector Enabled by All-Inorganic Lead-Free Perovskite Film With High Sensitivity and Low Detection Limit. *IEEE Transactions on Electron Devices* **67**, 3191–3198 (2020).

10. Zhang, Z. *et al.* Towards radiation detection using $Cs_2AgBiBr_6$ double perovskite single crystals. *Materials Letters* **269**, 127667 (2020).

11. Zhang, W. *et al.* Growth and photodetection properties of $Cs_2AgBiBr_6$ crystals with large flat (111) plane grown from the solution by adding toluene. *Journal of Crystal Growth* **552**, 125922 (2020).

12. Zuck, A., Schieber, M., Khakhan, O. & Burshtein, Z. Near single-crystal electrical properties of polycrystalline HgI_2 produced by physical vapor deposition. in *2002 IEEE Nuclear Science Symposium Conference Record* vol. 1 505–509 (IEEE, 2002).

13. Shih, C. T., Huang, T. J., Luo, Y. Z., Lan, S. M. & Chiu, K. C. Oriented polycrystalline α-HgI_2 thick films grown by physical vapor deposition. *Journal of Crystal Growth* **280**, 442–447 (2005).

14. Cao, X. *et al.* Fabrication of Perovskite Films with Large Columnar Grains via Solvent-Mediated Ostwald Ripening for Efficient Inverted Perovskite Solar Cells. *ACS Applied Energy Materials* **1**, 868–875 (2018).

15. Eggers, H. *et al.* Inkjet-Printed Micrometer-Thick Perovskite Solar Cells with Large Columnar Grains. *Advanced Energy Materials* **10**, 1903184 (2020).

16. Chern, Y.-C. *et al.* Grain structure control and greatly enhanced carrier transport by $CH_3NH_3PbCl_3$ interlayer in two-step solution processed planar perovskite solar cells. *Organic Electronics* **38**, 362–369 (2016).

17. Zhao, Y. *et al.* Perovskite seeding growth of formamidinium-lead-iodide-based perovskites for efficient and stable solar cells. *Nature Communications* **9**, 1607 (2018).

18. Haruta, Y., Ikenoue, T., Miyake, M. & Hirato, T. Fabrication of (101)-oriented $CsPbBr_3$ thick films with high carrier mobility using a mist deposition method. *Applied Physics Express* **12**, 085505 (2019).

19. Haruta, Y., Ikenoue, T., Miyake, M. & Hirato, T. Fabrication of $CsPbBr_3$ Thick Films by Using a Mist Deposition Method for Highly Sensitive X-ray Detection. *MRS Advances* **5**, 395–401 (2020).

20. Gao, W. *et al.* High-Quality $Cs_2AgBiBr_6$ Double Perovskite Film for Lead-Free Inverted Planar Heterojunction Solar Cells with 2.2 % Efficiency. *ChemPhysChem* **19**, 1696–1700 (2018).

21. Haruta, Y., Ikenoue, T., Miyake, M. & Hirato, T. One-Step Coating of Full-Coverage $CsPbBr_3$ Thin Films via Mist Deposition for All-Inorganic Perovskite Solar Cells. *ACS Applied Energy Materials* **3**, 11523–11528 (2020).

22. Slavney, A. H., Hu, T., Lindenberg, A. M. & Karunadasa, H. I. A Bismuth-Halide Double Perovskite with Long Carrier Recombination Lifetime for Photovoltaic Applications. *Journal of the American Chemical Society* **138**, 2138–2141 (2016).

23. Rocks, C., Svrcek, V., Maguire, P. & Mariotti, D. Understanding surface chemistry during $MAPbI_3$ spray deposition and its effect on photovoltaic performance. *Journal of Materials Chemistry C* **5**, 902–916 (2017).

24. Heo, J. H., Lee, M. H., Jang, M. H. & Im, S. H. Highly efficient $CH_3NH_3PbI_{3-x}Cl_x$ mixed halide perovskite solar cells prepared by re-dissolution and crystal grain growth via spray coating. *Journal of Materials Chemistry A* **4**, 17636–17642 (2016).

25. Liang, Z. *et al.* A large grain size perovskite thin film with a dense structure for planar heterojunction solar cells via spray deposition under ambient conditions. *RSC Advances* **5**, 60562–60569 (2015).

26. Jaffe, A. *et al.* High-pressure single-crystal structures of 3D lead-halide hybrid perovskites and pressure effects on their electronic and optical properties. *ACS Central Science* **2**, 201–209 (2016).

Chapter 6
Conclusions and Future Perspectives

6.1 Conclusions

To solve the world's energy problem, it is crucial to produce next-generation functional materials via low-energy processes. Recently, all-inorganic perovskites have much attention as a promising functional material that can be produced low-energy processes. However, the undeveloped scalable deposition method is a big issue for their practical applications. In this thesis, the author established the fundamental fabrication method for all-inorganic perovskite films by using a low-energy and scalable deposition process, that is mist deposition method. The results obtained through this thesis are summarized as follows:

Chapter 2. Mist deposition method for $CsPbBr_3$ films

The effects of the fabrication conditions for $CsPbBr_3$ films were investigated. The author clarified that substrate temperature effects on the morphology and crystal orientation of $CsPbBr_3$ films. In the range of the substrate temperature of 150–170 °C, dense $CsPbBr_3$ films consisting of highly (101)-oriented columnar grains were obtained. The author successfully obtained the columnar films with the thickness range of 5–28 μm. The obtained $CsPbBr_3$ film showed a low trap density of 1.3×10^{12} cm^{-3} and a high carrier mobility of 13 $cm^2 V^{-1} s^{-1}$.

Chapter 3. $CsPbBr_3$-based perovskite solar cells

Based on the knowledge obtained in Chapter 2, the author fabricated $CsPbBr_3$ thin films for the solar cell application. Poor coverage of $CsPbBr_3$ films has been an issue causing poor cell performance. The author demonstrated that full-coverage $CsPbBr_3$ thin films can be obtained by using the mist deposition method even the thickness is 340 nm. The author fabricated all-inorganic perovskite solar cells with the simple device configuration of

ITO/TiO_2/$CsPbBr_3$/carbon. The solar cells showed a high open-circuit voltage of 1.51 V and a power conversion efficiency of 8.3%, indicating the high potential of the mist deposition method for solar cell applications.

Chapter 4. $CsPbBr_3$-based X-ray detectors

For X-ray detection applications, $CsPbBr_3$ thick films were fabricated via the mist deposition method. The author demonstrated that the columnar grain can be grown with the height of over 100 μm, which means the fabrication of 100 μm thick $CsPbBr_3$ films. However, the thick film exfoliated from the substrate due to the thermal stress. The exfoliation was solved by using a polymer buffer layer, and the X-ray detector with the device configuration of Pt/polymer/$CsPbBr_3$/W was fabricated. The detector showed a sensitivity of 11,840 μC Gy_{air}^{-1} cm^{-2}, which is approximately 600 times higher than that of the currently available commercial a-Se X-ray detectors.

Chapter 5. Lead-free perovskites for X-ray detectors

To generalize the fabrication of perovskite films via the mist deposition method, the author focused on the lead-free inorganic perovskite ($Cs_2AgBiBr_6$). As same as the case of $CsPbBr_3$ fabrication, the author succussed the fabrication of $Cs_2AgBiBr_6$ thick films with closely packed columnar grains. The X-ray detector using the 92 μm-thick $Cs_2AgBiBr_6$ film showed a sensitivity of 487 μC Gy_{air}^{-1} cm^{-2}, which is comparable to that of X-ray detectors using $Cs_2AgBiBr_6$ single crystals. In addition, the mechanism of columnar grain growth was clarified through the precise observation of grains during crystal growth.

6.2 Future Perspectives

Demonstration of the large-area deposition

In this thesis, the fabrication of all-inorganic perovskite films via mist deposition method and their device applications for solar cells and X-ray detectors were demonstrated. However, the deposition area was just 3 cm in width that is determined by the width of the mist ejection nozzle used in this study. The practical level of a large area has not been demonstrated yet. Based on the knowledge obtained in this study, it is expected that the large-area deposition using the mist deposition method with a wide nozzle will be demonstrated in the future.

Successive formation of functional materials for efficient device fabrication

The mist deposition method has already been used for deposition of metal oxide and organic semiconductor thin films. In this study, the author has enabled the deposition of perovskite films by the mist deposition method, which enables an efficient device fabrication process by successive deposition of functional materials for devices. In Chapter 3, we demonstrate the fabrication of all-inorganic perovskite solar cells by using successive formation of TiO_2 and $CsPbBr_3$ via the mist deposition method.

Generalization of the mist deposition method for novel materials

In Chapter 4 and 5, the author successfully fabricated highly sensitive X-ray detectors using all-inorganic perovskite films. However, the unstable dark current should be solved for the application. According to recent studies, the migration of halide ions under a high bias is identified as the origin of the unstable dark current. To suppress the ion migration, novel materials are proposed one after another. In this study, the author provided the growth mechanism and demonstrated the generality of the mist deposition method, which makes it easier to fabricate novel materials via the mist deposition method for practical applications.

Rights

Chapter 2, 3, 4, and 5 in this thesis are written based on the peer-reviewed journal papers that the author (Yuki Haruta) wrote, which are shown on the next page.

List of Publications

Peer-Reviewed Journal Papers

1. **Yuki Haruta**, Shinji Wada, Takumi Ikenoue, Masao Miyake, Tetsuji Hirato

   "Columnar Grain Growth of Lead-Free Double Perovskite using Mist Deposition Method for Sensitive X-ray Detectors"

   Crystal Growth and Design **21**, 4030-4037 (2021).

2. **Yuki Haruta**, Takumi Ikenoue, Masao Miyake, Tetsuji Hirato

   "One-Step Coating of Full-Coverage $CsPbBr_3$ Thin Films via Mist Deposition for All-Inorganic Perovskite Solar Cells"

   ACS Applied Energy Materials **3**, 11523-11528 (2020).

3. **Yuki Haruta**, Takumi Ikenoue, Masao Miyake, Tetsuji Hirato

   "Fabrication of $CsPbBr_3$ Thick Films by Using a Mist Deposition Method for Highly Sensitive X-ray Detection"

   MRS Advances **5**, 395-401 (2020).

4. **Yuki Haruta**, Takumi Ikenoue, Masao Miyake, Tetsuji Hirato

   "Fabrication of (101)-oriented $CsPbBr_3$ thick films with high carrier mobility using a mist deposition method"

   Applied physics express **12**, 085505 (2019).

International Conference

1. **Yuki Haruta**, Takumi Ikenoue, Masao Miyake, Tetsuji Hirato

   "Fabrication of Cesium Lead Bromide Thick Films with Closely-Packed Columnar Crystals and High Carrier Mobility by Using a Mist Deposition Method" *2019 Materials Research Symposium Fall Meeting*, Boston, Massachusetts, EN09.06.09, December 3, 2019 (Poster).

2. **Yuki Haruta**, Takumi Ikenoue, Masao Miyake, Tetsuji Hirato

   "Successive Formation of Metal Oxide and Cesium Lead Halide Perovskites Thin Films Using a Mist Deposition Method for All-Inorganic Perovskite Solar Cells" *The 9th Asis-Pacific Workshop on Widegap Semiconductors*, OIST, Okinawa, Japan, ThP-OD-19, November 14, 2019 (Poster).

Conference in Japan

1. Mioko Kawakami, **Yuki Haruta**, Shinji Wada, Takumi Ikenoue, Masao Miyake, Tetsuji Hirato

   "X-ray detection using $(CH_3NH_3)_3Bi_2I_9$ thick film prepared via mist deposition method"

   The 82nd Japan Society of Applied Physics Fall Meeting 2021, Online, 21a-P07-6, September 21, 2021 (Poster).

2. Shinji Wada, **Yuki Haruta**, Takumi Ikenoue, Masao Miyake, Tetsuji Hirato

   "X-ray detection using $Cs_2AgBiBr_6$ thick film prepared via mist deposition method"

   The 68th Japan Society of Applied Physics Spring Meeting 2021, Online, 16p-Z28-14, March 16, 2021 (Oral).

3. Shinji Wada, **Yuki Haruta**, Takumi Ikenoue, Masao Miyake, Tetsuji Hirato

   "Fabrication of $Cs_2AgBiBr_6$ thick film via mist deposition method"

   The 81st Japan Society of Applied Physics Fall Meeting 2020, Online, 10p-Z14-4, September 10, 2020 (Oral).

4. **Yuki Haruta**, Takumi Ikenoue, Masao Miyake, Tetsuji Hirato

   "All-inorganic perovskite thick film formed by using mist deposition method and its X-ray detection properties"

   38th Electronic Materials Symposium, Nara, Japan, Fr2-8, October 11, 2019 (Poster).

5. **Yuki Haruta**, Takumi Ikenoue, Masao Miyake, Tetsuji Hirato

   "$CsPbBr_3$ thick films fabricated by using mist deposition method and its radiation detection properties"

   The 80th Japan Society of Applied Physics Fall Meeting 2019, Hokkaido, 21p-C213-3, September 21, 2019 (Oral).

6. **Yuki Haruta**, Takumi Ikenoue, Masao Miyake, Tetsuji Hirato

   "Fabrication of $CsPbBr_3$ thick films by mist deposition method"

   The 66th Japan Society of Applied Physics Spring Meeting 2019, Tokyo, 11p-S622-6, March 11, 2019 (Oral).

7. **Yuki Haruta**, Takumi Ikenoue, Masao Miyake, Tetsuji Hirato

   "Growth of dense $CsPbBr_3$ thin films by mist deposition method for all-inorganic perovskite solar cells"

   37th Electronic Materials Symposium, Shiga, Japan, Th1-17, October 11, 2018 (Poster).

8. **Yuki Haruta**, Takumi Ikenoue, Masao Miyake, Tetsuji Hirato

   “Fabrication of All-Inorganic Perovskite Solar Cells by Mist Deposition Method”

   The 79th Japan Society of Applied Physics Fall Meeting 2018, Nagoya, 21a-432-4, September 21, 2018 (Oral).

9. **Yuki Haruta**, Masaru Ui, Takumi Ikenoue, Masao Miyake, Tetsuji Hirato

   “Effect of substrate and growth temperature on fabrication of $CH_3NH_3PbI_3$ thin films by the mist deposition Method”

   36th Electronic Materials Symposium, Shiga, Japan, Th4-11, November 9, 2017 (Poster).

Patent

1. Keiji Abe, Toshiyuki Izawa, Kenji Makino, Seiichiro Mizuno, Takumi Ikenoue, **Yuki Haruta**, Masao Miyake, Tetsuji Hirato

   “Radiation detector and method for manufacturing radiation detector”

   PCT/JP2019/006625, US202102553A1

Acknowledgment

The author would like to express his deepest gratitude to Professor Tetsuji Hirato at Kyoto University for his supervision. The continuous support, guidance, and encouragement he gave me throughout my study have been a true blessing. The author is grateful to Professor Toshiya Doi and Professor Hitoshi Fujimoto for reviewing this thesis and giving a lot of invaluable instructions. The author is sincerely grateful to Associate Professor Masao Miyake for his detailed instructions and fruitful discussions. The author is grateful to Assistant Professor Takumi Ikenoue for his continuous discussion and help on various aspects of this study. The author believes that this thesis has reached its present form owing to their immeasurable amount of help and guidance.

The author greatly thanks Mr. Suguru Shiomi, Mr. Masaru Ui, Mr. Shota Higashino, Mr. Yuya Matamura, Mr. Shinji Wada, Ms. Mioko Kawakami, and all the people in the Materials Processing group in Energy Science Department for their kind help and the fruitful discussion throughout this study. Especially, Ms. Sachiko Yamamoto and Ms. Toshiko Morita provided countless arrangements to make a comfortable environment for this study.

The author greatly thanks Mr. Keiij Abe, Mr. Seiichiro Mizuno, Mr. Kenji Makino, and Mr. Toshiyuki Izawa in Hamamatsu Photonics K. K. for their kindly support. The author is grateful to Professor Toshiya Doi for his lending SEM equipment. The author is grateful to Assistant Professor Makhsud I. Saidaminov and his group's members for giving me an excellent opportunity to research in his group at the University of Victoria. The author sincerely appreciates the financial aid from the Japan Society for the Promotion of Science and the Japan Student Services Organization.

The author would like to thank all his family and friends for their heartful encouragement. The author believes that their continuous assistance was indispensable for accomplishing this study. The author is particularly grateful to his family, Masaki Haruta, Erika Haruta, Shoichi Haruta, and Kiyoka Haruta for their kind support and encouragement.